HAL
open science

Synthèse et transport électronique dans des nanotubes de carbone ultra-propres

Ngoc Viet Nguyen

To cite this version:

Ngoc Viet Nguyen. Synthèse et transport électronique dans des nanotubes de carbone ultra-propres. Physique [physics]. Université de Grenoble, 2012. Français. NNT : 2012GRENY045 . tel-00859807

HAL Id: tel-00859807

https://theses.hal.science/tel-00859807v1

Submitted on 9 Sep 2013

HAL is a multi-disciplinary open access archive for the deposit and dissemination of scientific research documents, whether they are published or not. The documents may come from teaching and research institutions in France or abroad, or from public or private research centers.

L'archive ouverte pluridisciplinaire **HAL**, est destinée au dépôt et à la diffusion de documents scientifiques de niveau recherche, publiés ou non, émanant des établissements d'enseignement et de recherche français ou étrangers, des laboratoires publics ou privés.

UNIVERSITÉ DE GRENOBLE

THÈSE

Pour obtenir le grade de

DOCTEUR DE L'UNIVERSITÉ DE GRENOBLE

Spécialité : **Physique des Materiaux**

Arrêté ministériel : 7 août 2006

Présentée par

Ngoc Viet NGUYEN

Thèse dirigée par **Dr. Wolfgang WERNSDORFER**

préparée au sein du **Institut Néel**
dans **l'École Doctorale de Physique**

Synthèse et transport électronique dans des nanotubes de carbone ultra-propres

Thèse soutenue publiquement le **25 Octobre 2012**
devant le jury composé de :

Dr. Vincent DERYCKE Rapporteur
CEA Saclay, Paris.
Prof. Philippe LAFARGE Rapporteur
Université Paris Diderot, Paris.
Dr. Vincent JOURDAIN Membre
Laboratoire Charles Coulomb, Montpellier.
Prof. Laurent SAMINADAYAR Président
Institut Néel, CNRS, Grenoble.
Dr. Jean-Pierre CLEUZIOU Membre
Institut Néel, CNRS, Grenoble.
Dr. Wolfgang WERNSDORFER Membre
Institut Néel, CNRS, Grenoble.

Université Joseph Fourier / Université Pierre Mendès France /
Université Stendhal / Université de Savoie / Grenoble INP

Université de Grenoble

Synthèse et Transport électronique dans des nanotubes de carbone ultra-propres

by

Ngoc Viet NGUYEN

A thesis submitted to obtain the
degree of Doctor of Philosophy

at the

Institut Néel

NANO department

Octobre 2012

Abstract

This thesis describes experiments on the synthesis of single wall carbon nanotubes (SWNTs), fabrication of ultraclean CNT devices, and study of electronic properties of CNTs with transport measurements. The first part of this work describes the optimization of the synthesis parameters (by chemical vapor deposition - CVD) such as carbon precursors, gas flows, temperature, catalyst for the growth of high quality SWNTs. In all these parameters, the catalyst composition plays a very important role on the high selective growth of SWNTs with a narrow diameter distribution. The second part deals with the nanofabrication of ultraclean CNT devices and the low temperature (40 mK) transport measurements of these CNT quantum dots. The level spectra of the electrons in the first shell are investigated using inelastic cotunneling spectroscopy in an axial magnetic field, which show a strong negative spin-orbit coupling of electron. We find that the sequence of electron shell filling in our case ($\Delta_{SO} < 0$) is different from which would be obtained in the pure SU(4) Kondo regime ($\Delta_{SO} = 0$). Indeed, a pure orbital Kondo effect is observed in N=2e at a finite magnetic field. In the last part of this thesis, we describe the experimental implementation of the thermal evaporation of single molecule magnets (SMMs) for the future fabrication of ultraclean CNT-SMM hybrid devices.

Keywords: carbon nanotubes, CVD, ultraclean CNT devices, transport measurement, spin-orbit coupling, single molecule magnets.

Résumé

Cette thèse décrit des expériences sur la synthèse de nanotubes de carbone (CNT) mono-paroi, leur intégration dans des dispositifs ultra-propres, ainsi que l'étude de leurs propriétés électroniques par des mesures de transport à très basse température. La première partie de ce travail décrit l'optimisation des paramètres de synthèse par déposition chimique en phase vapeur (CVD) tels que les précurseurs de carbone, les flux de gaz, la température, ou le catalyseur pour la croissance de CNT de très bonne qualité. Parmis tous ces paramètres, la composition du catalyseur joue un rôle decisif pour permettre une croissance sélective en mono-paroi ansi qu'une distribution de faible diamètre. Dans la deuxième partie nous développons la nanofabrication de boites quantiques ultra-propres à base de CNT ainsi que les mesures de transport de ces échantillons à basse température (40 mK). Le spectre de la première couche électronique du nanotube est mesuré par spectroscopie de *cotunneling* inélastique sous champ magnétique, montrant alors un fort couplage spin-orbite négatif, dans ce système. Nous montrons que la séquence de remplissage d'électrons dans notre cas ($\Delta_{SO} < 0$) est différente de celle que l'on obtiendrait en régime Kondo SU (4) ($\Delta_{SO} = 0$). En effet, un effet Kondo purement orbital est observé pour N = 2e à champ magnétique fini. Dans la dernière partie de cette thèse, nous décrivons la mise en œuvre expérimentale d'un évaporateur thermique à aimants à molécule unique (SMMs) pour la fabrication future de dispositifs hybrides CNT-SMM ultra-propres.

Mots-clés: nanotubes de carbone, CVD, ultra-propre dispositifs CNT, mesure de transport, couplage spin-orbite, aimants à une seule molécule.

Acknowledgements

This thesis would not have been possible without the help and company of many people in the Néel Institut/CNRS Grenoble through my three years of study here.

First of all, I want to thank Dr. Vincent Derycke and Prof. Philippe Lafarge for accepting to be the referees of my thesis, as well as Prof. Laurent Saminadayar and Dr. Vincent Jourdain for accepting to join the jury of this thesis. Many thanks for their time devoted to the careful reading of the manuscript. I benefited a lot from their comments and suggestions on my thesis.

I wish to express my sincere appreciation to my advisor, Dr. Wolfgang Wernsdorfer, for his scientific guidance and supports during the course of this research work. Your assistance and suggestions were crucial in the realization of this work. Your passion for work, enthusiasm to young researchers, insight into physics, and scientific integrity has left me a deep impression and taught me how a good scientist should be. I am lucky to have been your student.

The person with whom I have worked most is Dr. Jean-Pierre Cleuziou. Actually he has introduced me most of the technical skills from CNT synthesis, characterizations, nanofabrications and measurements. I have learnt a lot from his exceptional skills and practical approach to things. His insight into physics and nanomaterials has been a constant source of inspiration, and his clear explanations have led me to the nanotubes world and greatly enhanced my understanding to the mesoscopic physics. I owe a large debt of gratitude to Jean-Pierre for his always being supporting, understanding and suggestions.

I was very fortunate to get helps from a lot of people in the Lab. First, I would like to thank the successive directors of the Institute, Alain Fontaine and Alain Schuhl, for their reception. I need also to thank particularly Joel Cibert and Hervé Courtois, the successive directors of the NANO department, for excellent working conditions and a friendly atmosphere that I benefited much within the department. I would like to thank Véronique Fauvel and Sabine Gadal for their kind helps concerning many administrative questions.

This thesis represents a large experimental effort, and I am extremely grateful to the staffs of CNRS and CEA. Special thanks to Richard Haettel, Eric Eyraud, Didier Dufeu and Julien Jarreau for their great helps and technical supports on the CVD setup, cryogenics, evaporators. Thanks to Nedjma Bendiab, Valérie Reita and Antoine Reserbat-Plantey for the

introduction and discussions on the Raman spectroscopy of CNTs. Thanks to Maria Bacia, Stéphanie Kodjikian and Sébastien Pairis for accepting me a right of intensive use of TEM and SEM. Thanks to Laetitia Marty for the AFM instruction and the Nanochimie working condition. Thanks to all the people in the NANOFAB and PTA for the best and opening working environment for the nanofabrication, specially to Thierry Fournier, Thierry Crozes, Bruno Fernandez, Thibault Haccart and Helge Haas.

I would like to thank all the supports and valuable discussions during this work coming from Franck Balestro, Edgar Bonet-Orozco, Christophe Thirion, Vincent Bouchiat, Laurent Cagnon, Serge Florens. Thanks to the PhD students: Matias Urdampilleta, Romain Vincent, Marc Ganzhorn, Stefan Thiele, Zheng Han, Zahid Ishaque for helps in my work and living in Grenoble. Thanks to the two post-docs of the group, Oksana Gaier and Jarno Jarvinen, for their time of reading my thesis and suggestions.

I am grateful to the European Research Council (ERC) for the fellowship which assures me the financial support of this thesis.

And finally, I want to thank my family and my Vietnamese friends for their always following and sparing advices when I needed most. Special thanks to my wife and my little daughter, who had to bear my being away for such a long time, for their patient love and encouragement.

Contents

1. General introduction 1

2. Structures and synthesis methods of carbon nanotubes 5

2.1. SP^2 Hybridized Based Carbon Allotropes 6

2.2. Carbon Nanotube Crystal Structure 7

2.2.1. Single-Walled and Multi-Walled Carbon Nanotubes 7

2.2.2. From Graphene to Carbon Nanotubes 8

2.2.3. Electronic band structure of carbon nanotubes 9

2.3. Carbon nanotubes synthesis methods 12

2.3.1. The physical synthesis methods 13

2.3.2. Catalytic Decomposition 14

2.4. Catalytic Vapor Deposition Synthesis of SWNTs 15

2.4.1. Hydrocarbon decomposition 15

2.4.2. Growth mechanism 16

2.4.3. The catalyst 18

2.5. Conclusion 20

3. Synthesis and characterization of single wall carbon nanotubes 24

3.1. Motivation 24

3.2. Description of experiments 25

3.2.1. CVD setup 25

3.2.2. Catalyst composition and preparation 27

3.2.3. Local deposition of the catalyst on a surface 29

3.2.4. Characterization methods 30

3.3. Optimization the CVD synthesis conditions 31

3.3.1. Methane CVD 33

3.3.2. Ethylene CVD 38

3.3.3. Ethanol CVD 40

3.4. Optimization of the catalyst composition 43

3.4.1. Fe-Mo catalyst 44

3.4.2. Fe-Ru catalyst 54

3.5. Conclusion 60

4. Nanofabrication and Measurement Setup 65

4.1. Motivation 65

4.2. Fabrication of ultraclean suspended CNT devices 67

4.2.1. Fabrication of the electrodes 67

4.2.2. In situ CVD growth of the suspended CNTs 70

4.2.3. Fabrication of devices with local gate 72

4.3. Device characterizations at room temperature 73

4.3.1. Measurement setup 73

4.3.2. Room temperature conductance measurements 76

4.4. Dilution refrigerator 78

4.5. Conclusion and perspectives 81

5. Electronic properties of carbon nanotubes quantum dots 83

5.1. Introduction 83

5.2. Quantum dots 83

5.3. Coulomb blockade 85

5.4. CNT four-fold energy level structure 90

5.5. Spin-orbit coupling in CNTs 93

5.6. Kondo effects 98

5.7. Conclusion 105

6. Ultraclean carbon nanotube quantum dot with a strong negative spin-orbit coupling in the Kondo regime 109

6.1. Introduction 109

6.2. Kondo effect of ultraclean CNT quantum dot with SOI splitting 111

6.2.1. Conductance at zero magnetic field 111

6.2.2. Evolution of Kondo ridges as a function of applied magnetic field 114

6.3. Conclusion 121

7. Evaporation of $TbPc_2$ Single Molecule Magnets 123

7.1. Motivation 123

7.2. Introduction to $TbPc_2$ single molecule magnets and grafting methods 123

7.2.1. $TbPc_2$ Single molecule magnets 123

7.2.2. SMMs deposition methods 124
7.3. Experimental details 125
7.3.1. Evaporation setup 125
7.3.2. Evaporation parameters 126
7.4. Results and discussions 127
7.4.1. Evaporating temperature 127
7.4.2. The integrity of the SMMs after thermal evaporation 128
7.4.3. Effect of evaporation time on thickness and size of molecule clusters 131
7.4.4. Evaporation of $TbPc_2$ onto suspended CNTs 133
7.5. Conclusion 134

8. Conclusions and perspectives 137
8.1. Summary of the results 137
8.2. Outlook 138

Annex 1. Binary phase diagrams of C-Mo and C-Ru I
Annex 2. Spin-orbit coupling in Kondo regime of ultra-clean CNT III

Chapter 1. General introduction

Carbon nanotubes (CNTs) are one-atom thick cylinders formed of carbon atoms. Since their discovery, the CNTs have attracted tremendous interest in scientific community owing to their unique structural and electronic properties [1]. For example, carbon nanotubes can be metallic or semiconducting depending on the orientation of the atomic lattice with respect to the axial direction, despite the fact that there is no difference in the local chemical bonding between the carbon atoms. An interesting characteristic of these nanotubes, shared with graphene, is the four-fold degeneracy of the energy level spectrum resulting from spin and orbital degeneracy.

When a short segment of a CNT is connected to metal electrodes, at low temperatures it behaves as a quantum dot (QD). The QDs are known as artificial atoms, with features close to those of real atoms. Moreover, QDs have the advantage that the attractive potential of the nucleus in real atom is replaced by a confinement potential which can be controlled and tuned in the experiment. It is also possible to confine and control the number of electrons in the QD due to the Coulomb blockade effect. These properties make CNT QDs ideal objects for studies at molecular level.

Our group "Nanospintronics and Molecular Transport" in the Néel Institute/CNRS Grenoble aims to fabricate, characterize and study molecular devices (molecular spin-valves and spin-filters, molecular spin-transistors, carbon nanotube junctions, nano-SQUIDs, molecular double-dot devices etc.) in order to read and manipulate spin states of a single molecule and to perform basic quantum operations [2]. In most of these devices, by utilizing the quantum transport measurement technique, carbon nanotubes are used as probes due to their high sensitivity to small changes in the electrostatic environment. At the time I joined the group, the nanotubes used for such a device fabrication were supplied by the collaborators in bulk form. These CNTs were dispersed into solution, deposited onto an isolating surface, located by microscopy (SEM or AFM), and patterned with metallic contacts by electron beam lithography and metal evaporation. The CNT junctions were thus inevitably contaminated chemically and structurally which most probably had an effect on their transport properties [3].

The disadvantages of using these CNTs initially motivated this project. We decided to implement a CVD setup in the group in order to directly grow separated high quality SWNTs, which can be used as directly after the growth. Moreover, using this technique it should be possible to fabricate “ultraclean” CNT devices, which have shown very interesting properties [4] that had never been observed in the CNT devices pinned on the substrate surface.

The main objectives in this thesis include: the synthesis of high quality SWNTs, fabrication of ultraclean CNT devices, and study of the electrical transport. Since the CVD technique leads to a growth of different kinds of carbon products including SWNTs, MWNTs, etc. having wide variety of length, density and diameter, we had to optimize the CVD parameters in order to have a proper control over the growth. We tried to find out a process for very highly selective growth of high quality SWNTs with a narrow diameter distribution. Once these optimal conditions are applied for the *in situ* growth of suspended CNT devices, we have a relatively high certainty about what kind of CNT is connected. The electrical transport in such an ultraclean CNT device is expected to reveal undiscovered phenomena of the quantum physics. The key issues in this work are the fabrication of CNT nanojunctions and the low temperature measurements on the devices. Concerning the fabrication, we developed a procedure using a state of the art all electron beam lithography process, which enables high accuracy fabrication of devices with small and elaborate structures. The electrical transport measurements are performed in our groups dilution refrigerators with multiaxis superconducting magnets.

This thesis is organized as follows.

In Chapter 2, we give a review about the structure and electronic properties of carbon nanotubes. Then, we introduce the main strategies of synthesis of CNTs and particularly emphasize on the Catalytic Chemical Vapor Deposition (CVD) technique used in this work.

Chapter 3 presents our work on the synthesis of SWNTs. By varying different growth parameters such as carbon precursors, gas flows, temperatures, catalysts, and characterizing very well the CNTs grown at each condition, we found the optimal parameters for obtaining high quality SWNTs. In our CVD synthesis, the catalyst composition plays a very important role on the growth of CNTs influencing to tubes lengths, number density, diameters and number of walls. Two different catalyst systems have been studied, Fe-Mo and Fe-Ru, which

both led to high selective growth of SWNTs with narrow diameter distribution. The optimal conditions for the synthesis were applied for device fabrication as described in the next chapter.

Chapter 4 is devoted to the description of the nanofabrication of our ultraclean CNT devices. All the patterns of the chip (source and drain electrodes, local gate, catalyst islands) are first fabricated, which is followed by the *in situ* growth of CNTs by the CVD technique at the last step. The resulting CNT junctions lie freely suspended on top of the source and drain electrodes without any contact with the substrate of the device, and thus are ultraclean from defects and disorders. We also briefly describe the techniques used to characterize these devices at room and low temperatures.

In Chapter 5, we recall the main characteristics of CNT quantum dots and review the recent low-temperature transport measurements. Depending on the contact between a CNT and source-drain electrodes, the electrical transport through the quantum dot can be either in Coulomb blockade or Kondo regime. CNT QDs are special due to their four-fold degenerate energy level spectrum that also leads to high symmetry SU(4) Kondo effect. Moreover, recent studies have shown that the spin-orbit coupling of electrons in CNT is quite significant, which can break these symmetries and change the sequence of electron filling of the CNT QD.

In Chapter 6, we present the electrical transport measurements of our ultraclean CNT devices. The electronic level spectrum of the first few electrons are investigated using inelastic cotunneling spectroscopy, which exhibits the spin-orbit coupling and the Kondo effect. When both phenomena are comparable in strength, the spin-orbit interaction lifts the four-fold Kondo symmetry and quenches the zero bias Kondo resonance at half filling. In these measurements, we found that the spin-orbit coupling of the electron is quite strong and especially has a negative value. A pure orbital level degeneracy in the two electron regime is also observed [5].

In Chapter 7, we describe the development of a technique to fabricate hybrid devices of suspended CNTs attached by single molecule magnets (SMMs). Since the grafting of SMMs onto CNTs can be done either by chemical solution drop casting method like our recent publication [6], or by physical thermal evaporation, we chose the later to keep our

CNT as clean as possible. Here, we describe the building of the evaporation setup and optimization of the process parameters. Due to the small size and small amount of the evaporated SMMs (clusters of one or few molecules), we first tried the evaporation on a very flat surface of sapphire and graphene for characterizations, before applying to CNT. Some primary results are presented, but this work is still in progress and needs more elaborate studies.

Finally, Chapter 8 summarizes and concludes this thesis.

References

[1] M. S. Dresselhaus, G. Dresselhaus, and P. Avouris, Eds., *Carbon Nanotubes: Synthesis, Structure, Properties and Applications*, 1st ed. Springer, 2001.

[2] L. Bogani and W. Wernsdorfer, "Molecular spintronics using single-molecule magnets," *Nature Materials*, vol. 7, no. 3, pp. 179–186, 2008.

[3] P. G. Collins, "Defects and disorder in carbon nanotubes," in *Oxford Handbook of Nanoscience and Technology: Frontiers and Advances*, Oxford: Oxford Univ. Press, 2009.

[4] F. Kuemmeth, S. Ilani, D. C. Ralph, and P. L. McEuen, "Coupling of spin and orbital motion of electrons in carbon nanotubes," *Nature*, vol. 452, no. 7186, pp. 448–452, Mar. 2008.

[5] J.-P. Cleuziou, N.-V. Nguyen, S. Florens, and W. Wernsdorfer, "Ultraclean carbon nanotube quantum dot in the Kondo regime with a strong negative spin-orbit coupling," *To be published*.

[6] M. Urdampilleta, N.-V. Nguyen, J.-P. Cleuziou, S. Klyatskaya, M. Ruben, and W. Wernsdorfer, "Molecular quantum spintronics: supramolecular spin valves based on single-molecule magnets and carbon nanotubes," *Int J Mol Sci*, vol. 12, no. 10, pp. 6656–6667, 2011.

Chapter 2. Structures and synthesis methods of carbon nanotubes

Since their discovery, carbon nanotubes (CNTs) have attracted tremendous interest due to their interesting physical properties. In particular, their (quasi) ideal 1D crystal structure combined with the C sp^2 hybridization, are responsible for intriguing electronic transport properties, interesting for both fundamental research as well as potential applications in nanotechnology and engineering. Besides, the controlled synthesis of high-quality CNTs has been the goal of many research endeavors and a wide variety of synthetic methods have been developed to produce the desired materials for specific scientific studies or technological applications.

This chapter has two main purposes. The first one is to introduce carbon based nanomaterials (section 2.1) and especially CNTs. The main CNT physical properties, specifically structural and electronic properties, are briefly reviewed (section 2.2). Then, we introduce the main strategies used for their synthesis (section 2.3). Section 2.4 particularly emphasizes on the description of the Catalytic Vapor Decomposition (CVD) technique used in this thesis.

2.1. SP^2 Hybridized Based Carbon Allotropes

An amazing property of the carbon atom is its versatility to form different kinds of solid state compounds with completely different physical and chemical properties. In particular, when carbon atoms combine altogether to constitute a crystalline solid, the $1s^2$, $2s^2$ and $2p^2$ carbon atomic orbitals can hybridize differently (mainly sp^2, sp^3) and form different kinds of C-C bonds. This explains, for instance, the striking different mechanical properties of graphite (sp^2) and diamond (sp^3).

The main crystalline solids resulting from sp^2 hybridized carbon atoms are depicted in Fig. 2.1a, including graphite (3D), graphene (2D), nanotube (1D), and fullerene (0D). A schematic representation of the sp^2 hybridization is shown in Fig. 2.1b. While the three atomic orbitals, 2s, $2p_x$, and $2p_y$, are hybridized into three sp^2 orbitals in the same plane, the $2p_z$ orbitals lie orthogonal to this plane, with a rotational symmetry around the perpendicular axis. The free electrons in the $2p_z$ orbitals contribute mainly to the electrical conduction and form respectively the π bounding and π^* anti-bounding conducting bands of the graphene (see the following of the section).

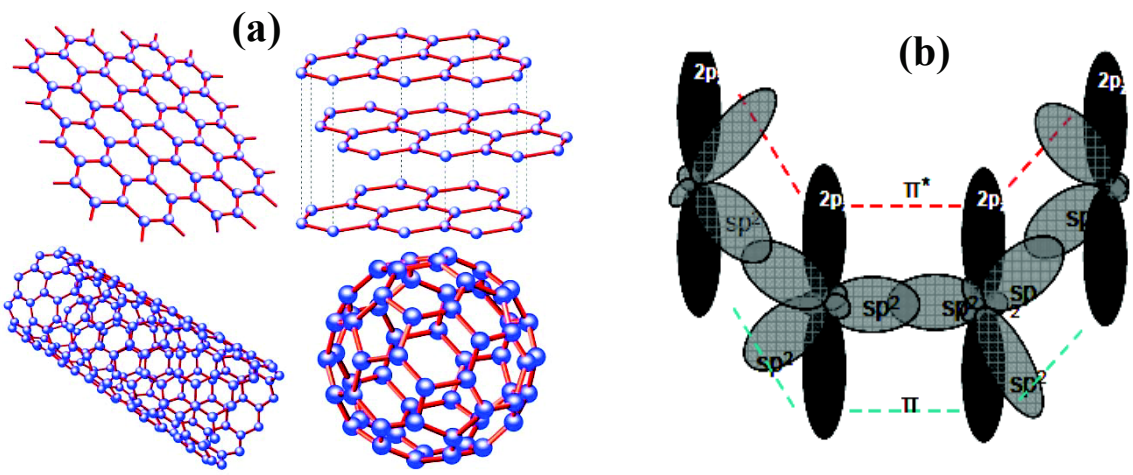

Figure 2.1. sp^2 hybridization of carbon and its derived materials. (a) From 3D to 0D carbon-based materials: bulk graphite (top right), graphene (top left), CNTs (bottom left), and fullerene (bottom right). (b) The three sp^2 hybridized orbital are in-plane, while the $2p_z$ orbital lies orthogonal to the plane. Adapted from refs. [1], [2].

After this brief introduction about carbon-based materials, we focus on the study of the CNTs in the following.

2.2. Carbon Nanotube Crystal Structure

2.2.1. Single Wall and Multi Wall Carbon Nanotubes

Carbon nanotubes can be divided into two main classes: single and multi wall carbon nanotubes. A single wall carbon nanotube (SWNT) is an atomic thick hollow cylinder formed by sp^2 hybridized carbon atoms (Fig. 2.1.b). A concentric multi wall carbon nanotube (MWNT) can be described as several SWNT shells arranged inside each other (like the "Russian dolls"). The distance between layers is approximately equal to the graphite inter-layer distance of 0.34 nm [3]. The diameter of CNTs typically varies from 1 nm (SWNTs) to few tens of nm (MWNTs), with lengths up to several centimeters. Figure 2.2 shows examples of respectively a Scanning Tunneling Microscopy (STM) spectrum (Fig. 2.2a) and Transmission Electron Microscopy (TEM) pictures of SWNT (Fig. 2.2b) and MWNT (Fig. 2.2c).

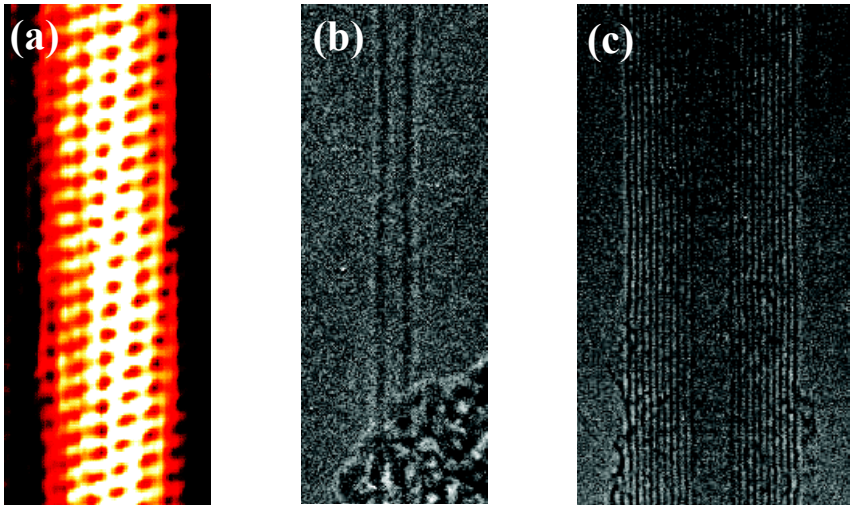

Figure 2.2. Evidence of the existence of carbon nanotubes. (a) Scanning tunneling microscopy (STM) picture confirming the atomic structure of a SWNT [4]. (b) and (c) are Transmission electron microscopy (TEM) images of respectively single wall (SWNT) and multi wall (MWNT) carbon nanotubes [5]. The single and multiple shell structures are well seen in (b, c).

2.2.2. From Graphene to Carbon Nanotubes

In order to describe the CNT structure, it is convenient to consider a SWNT as a rolled 2D graphite sheet (a graphene), thus forming a single carbon atom thick cylinder [6]. The graphene structure, depicted in Fig. 2.3, consists in a planar hexagonal network of carbon atoms (often called the honeycomb lattice), each atom having 3 closest neighbors, with an inter-atomic distance a = 1.42 Å. The graphene structure can be described by two independent lattice unit vectors (Fig. 2.3). These vectors can be expressed in the (x, y) plane as:

$$\vec{a}_1 = (\sqrt{3}\,a/2,\ a/2),\quad \vec{a}_2 = (\sqrt{3}\,a/2,\ -a/2) \tag{2.1}$$

The nanotube structure is obtained by rolling the one thick layer carbon sheet around a 'chiral vector' (also called wrapping vector). The chiral vector wraps the nanotube circumference so that the tip of the vector meets its own tail. It can be expressed as:

$$\vec{C} = n\vec{a}_1 + m\vec{a}_2, \qquad \text{where } 0 \le m \le n \tag{2.2}$$

The couple of the integer indices (n,m) describes the different ways to wrap the graphene structure on itself. Each pair of (n,m) defines the nanotube diameter d_t and its chiral angle ϕ which can be expressed as [7]:

$$d_t = \frac{C}{\pi} = \frac{a}{\pi}\sqrt{n^2 + m^2 + nm} \tag{2.3}$$

$$\phi = \arccos\left(\frac{\sqrt{3}(n+m)}{2\sqrt{n^2 + m^2 + nm}}\right) \tag{2.4}$$

An example of the (10,5) SWNT is shown in Fig. 2.3. The chiral vector $\vec{C}$ is perpendicular to the tube axis and the translational vector $\vec{T}$ is parallel to it.

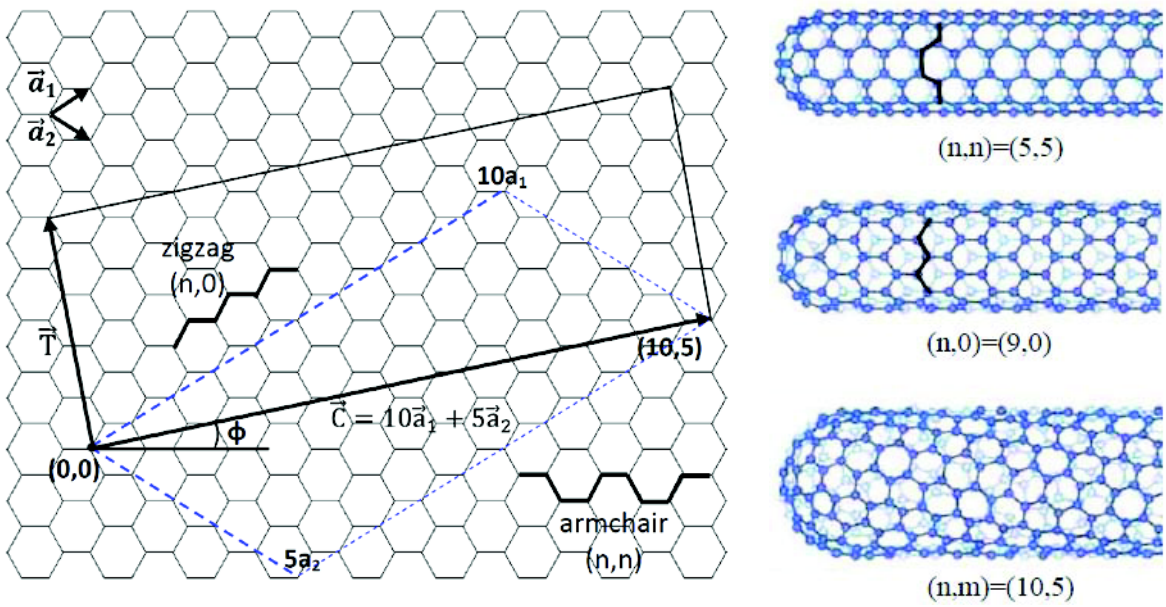

Figure 2.3. Formation of carbon nanotube from graphene sheet. (left) The way to construct the (10,5) SWNT. The rectangular defined by |T × C| is the unit cell of the nanotube. This nanotube has diameter d_t = 1nm and chiral vector 10.9°. (right) Carbon nanotubes with different structures: armchair (5,5), zigzag (9,0) and chiral (10,5) [8]. The zigzag and armchair lines (bold lines) are special symmetry directions.

Nanotubes with indices (n, n) (ϕ = 0°) and (n, 0) (ϕ = 30°) are rolled up along special symmetry directions of the graphene sheet. They are non-chiral and denoted as armchair and zigzag tubes, respectively. These names come from the 'armchair' and 'zigzag' shapes of carbon bonds along the circumference of the nanotubes.

2.2.3. Electronic band structure of carbon nanotubes

Following the same approach, electronic band structure of CNTs can be obtained by projecting the graphene band dispersion into the 1D longitudinal CNT dimension. The graphene energy band structure [8] can be calculated using the well known tight-binding method, also called the Linear Combination of Atomic Orbitals (LCAO) approximation [9]. We do not describe the calculation here, but just show the main results, plotted in Fig. 2.4.

The graphene energy dispersion consists of two branches (bonding and antibonding), touching at the 6 corners of the hexagonal Brilloin zone, called the Dirac K points. One particularly interesting feature of graphene is the unusual conical low energy dispersion [10] close to the Dirac points.

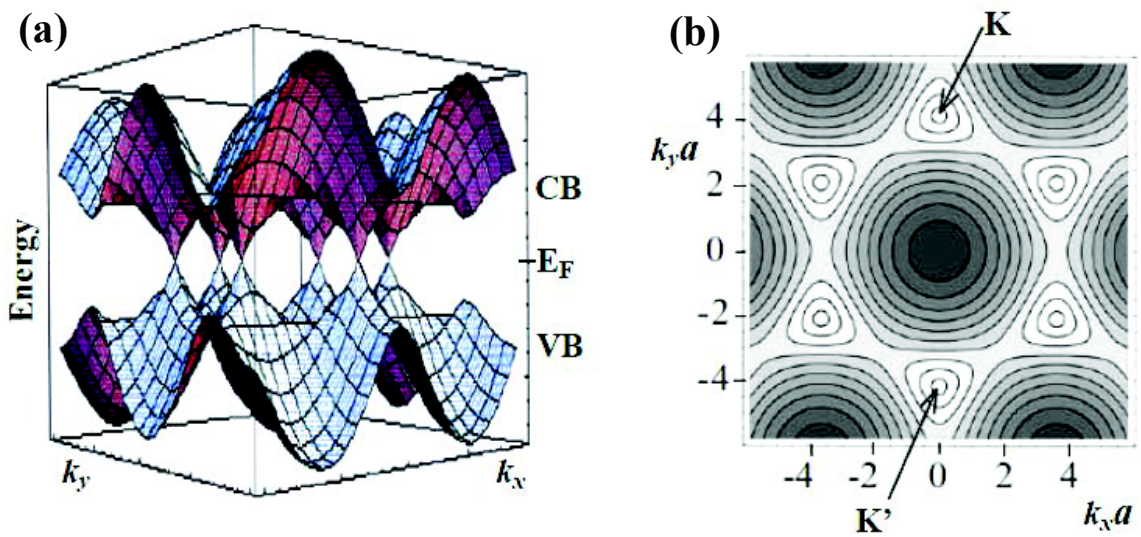

Figure 2.4. The energy dispersion of graphene. (a) There are six K points where the valence (VB) and conduction (CB) bands meet (E_F=0). (b) Contour plot of the valence band. The six K points define the first Brillouin zone of the graphene band structure. Two nonequivalent points K and K' are shown with the coordinates (k_x, k_y) = (0, ±4π/3a), respectively (adapted from ref. [10]).

The energy band structure of CNT is then obtained from the one of graphene, after introducing periodic boundary conditions due to the cylindrical geometry of the tube. Since a SWNT is considered as an infinitely long cylinder with a very small diameter, the wave vector $k_{//}$ (parallel to the tube axis) is continuous but the wave vector $k_{\perp}$ (perpendicular to the tube axis) becomes quantized, so that the following periodic boundary condition is fulfilled:

$$\vec{k}_{\perp}\vec{C} = \pi d k_{\perp} = 2\pi j \qquad (2.5)$$

where d is the SWNT diameter and j an integer.

The CNT band structure can be obtained by cutting the energy dispersion of graphene along the allowed $k_\perp$ lines values, as shown in Fig. 2.5a. Each intersection of the cross-sectional cut gives rise to a 1D subband. Due to the small diameter of the SWNT, the spacing between $k_\perp$ values is quite large ($\Delta k_\perp = 2/d$), which leads to strong observable effects of SWNT. The band structure of a SWNT is therefore dependent on the spacing between the allowed $k_\perp$ states and their angles with respect to the surface Brillouin zone of graphene. These values are determined by the diameter and chirality of a SWNT. For a given pair of (n,m) indices, the nanotube will be metallic with a finite density of states at the Fermi energy if the allowed $k_\perp$ lines pass directly through the K points (Fig. 2.5b). Otherwise, the SWNT will be semiconducting with a finite band gap (Fig. 2.5c).

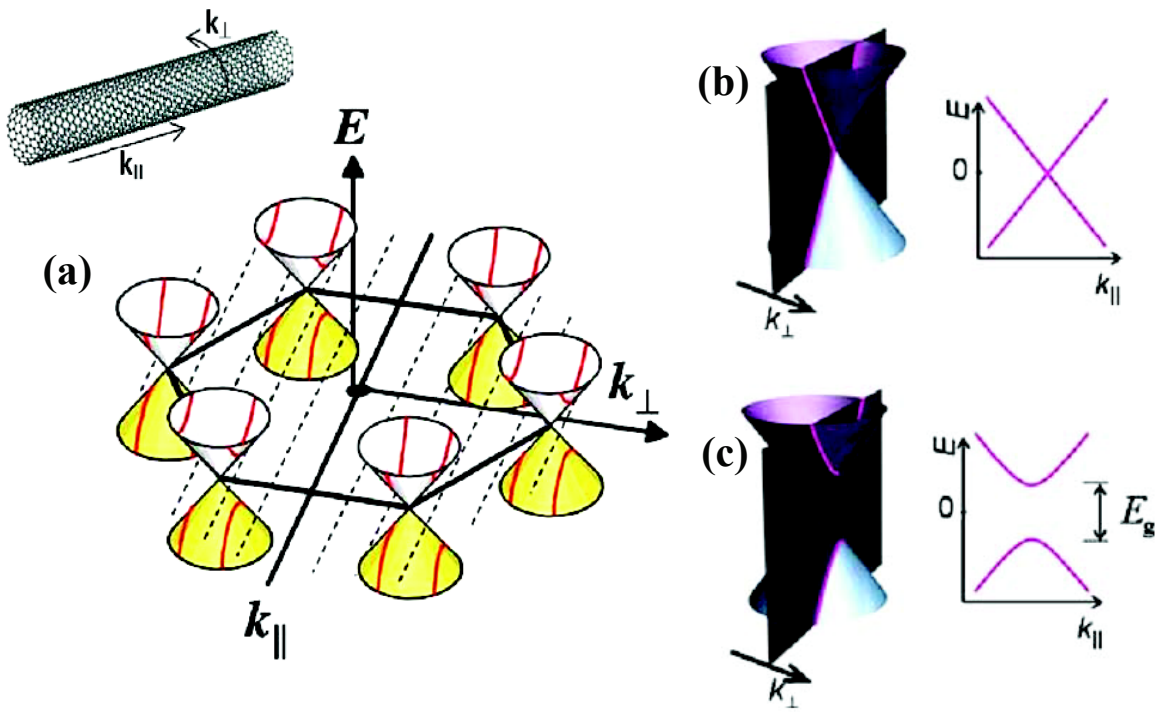

Figure 2.5. The band structure of SWNTs. (a) Quantized numbers of allowed $k_\perp$ by imposing periodic boundary conditions along the nanotube circumference. The band structure of a SWNT is obtained by cross-sections as indicated. (b) Low energy dispersion of a metallic SWNT: there is an allowed value of $k_\perp$ which passes through K. (c) Semiconducting SWNT with a finite band gap (adapted from refs. [10], [11]).

Semiconducting or metallic CNTs can be directly identified from the chiral indices (n, m). If the value of (n-m)/3 is an integer, the CNT is metallic. In other cases, the tube will be a semiconductor and the distance from closest $k_\perp$ misses the K-point by 2/3d [9]. The probability to find semiconducting and metallic nanotubes is in theory 2/3 and 1/3, respectively. Semiconducting SWNTs with diameters in the range of 0.8 to 3 nm have band gaps of 0.2 to 0.9 eV, which is inversely proportional to the diameter [1].

We highlight that this introduction of CNT band structure is quite simplified, mostly for pedagogical reasons. Indeed, it is valid only at low energies, where only one 1D subband can be considered. Besides, it does not take care of curvature effects which may translate the Dirac points of graphene and thus induce a small band gap in most of metallic CNTs (except for highly symmetric armchair CNTs), or the curvature effects responsible of the spin-orbit coupling in CNTs. When including the CNT curvature, π and σ orbitals are not completely orthogonal and the resulting π-σ hybridization has to be taken into account [9], [12]. In the following, we therefore call “small band gap” or “quasi-metallic” for the CNTs which have a small gap induced by such a perturbation.

After this short introduction of CNTs, we now turn to the overview of the CNT synthesis methods.

2.3. Carbon nanotubes synthesis methods

The synthesis of CNTs can be carried out using various methods, broadly divided into two main categories: physical and chemical, depending upon the process used to extract atomic carbon from the carrying precursor. Physical methods typically use high energy sources, such as plasma in an arc discharge experiment or laser ablation, to extract the carbon atoms. At the opposite, chemical methods rely on the extraction of carbon solely through catalytic decomposition of precursors on transition metal nanoparticles. While the two formers (arc discharge and laser ablation) are considered as high temperature methods, chemical vapor deposition is known as an ‘intermediate’ temperature method with the growth temperature in the range of 500 – 1200 °C [13].

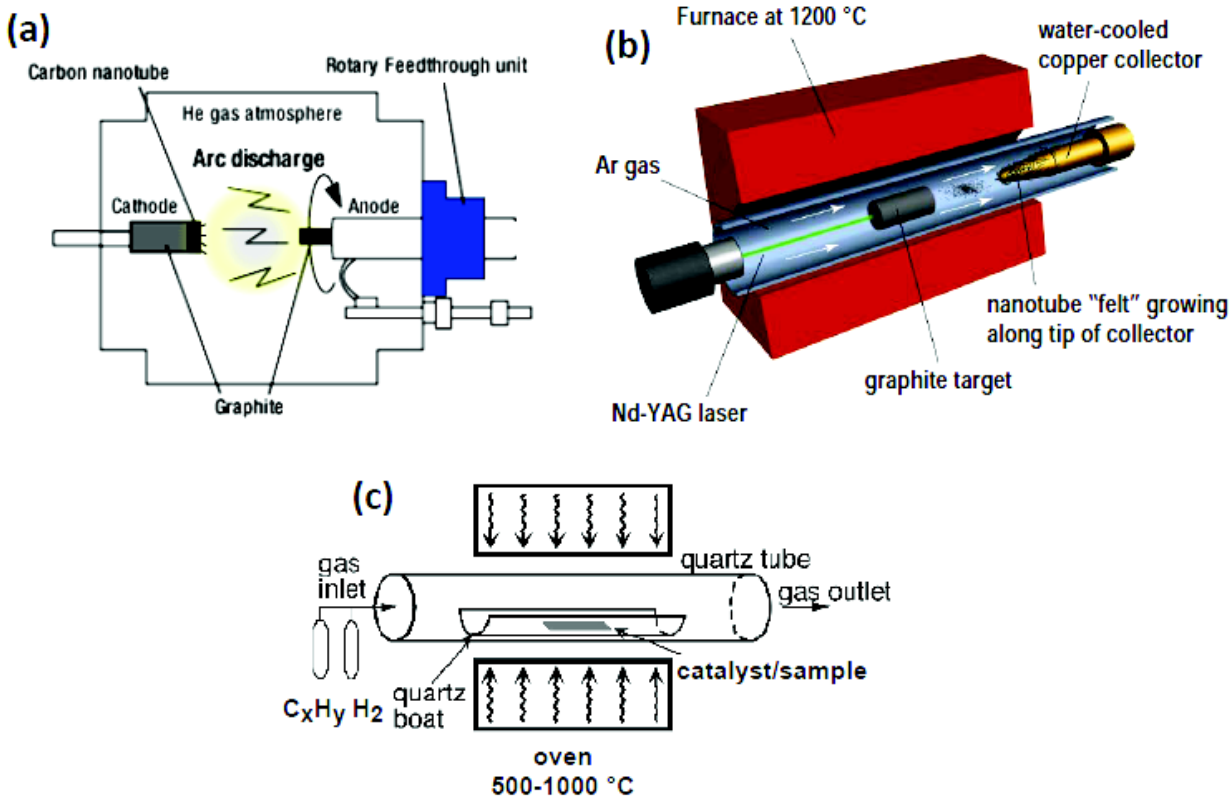

Figure 2.6. Schematics of experimental methods for CNT growth. (a) Arc discharge [14], (b) Laser ablation [15], and (c) Catalytic vapor deposition (CVD) [13].

2.3.1. The physical synthesis methods

Arc discharge

Arc discharge is the first known method to produce CNTs, dating for more than 20 years [16]. In this process, carbon atoms are evaporated by a plasma of inert He gas, created by passing a high current through two graphitic electrodes (Fig. 2.6a). This method can produce both MWNTs and SWNTs, with the coexistence of carbon whiskers, soot, fullerenes and amorphous carbon [3], [16]. While MWNTs can be obtained on the cathode without catalyst, SWNTs can only be formed by doping the anode with transition metals such as Co, Fe, Ni and their mixtures [17].

Laser ablation

Laser ablation is another technique to grow carbon nanotubes, which is also based on the evaporation of solid graphite. Intense laser pulses are used to ablate a graphite target, which is placed in an oven heated at ~ 1200 °C. A flowing inert Ar gas is added to push the grown products from the high temperature zone to the cooled copper collector outside the furnace (Fig. 2.6b). Like the case of arc discharge, the use of a pure graphite target leads to the formation of MWNTs, while a target doped with metallic catalysts (such as Co/Ni or Ni/Y) produces SWNTs [18], [19]. These SWNTs are mostly in the form of ropes consisting of tens of individual nanotubes, which are formed due to the Van der Waals interactions.

Despite that the physical growth methods yield to very well crystallized and high quality CNTs, the raw material may have to be purified and extracted from the carbon soot . Besides, even when dispersed in solutions, CNTs (especially the SWNTs) are mostly arranged into bundles and it is difficult to isolate individual CNTs on a surface. Furthermore, all these steps may damage or even functionalize the CNT structures [17]. This is not suitable for many applications. Such limitations directed most of current researches towards alternative chemical based methods [20], providing more versatility and better integration for the design of new device architectures [13].

2.3.2. Catalytic Decomposition

In the catalytic decomposition method (Fig. 2.6c), a hydrocarbon precursor reacts with catalyst nanoparticles. At moderate temperature of 600-800 °C, the carbon atoms decompose from hydrocarbon precursor and are adsorbed on the catalyst nanoparticle surface, which is followed by the nucleation and growth of the CNTs. In this work, we use the catalytic chemical vapor deposition (CVD) for the growth of SWNTs. Therefore, the main parameters of the synthesis are described in the following.

2.4. Catalytic Vapor Deposition Synthesis of SWNTs

2.4.1. Hydrocarbon decomposition

The decomposition of hydrocarbon occurs at high temperatures of the CVD process in absence of oxygen. This process is called pyrolysis. Different gas phase carbon based compounds have been used as precursors for the CVD growth of CNTs such as: CO [21], CH_4 [22], C_2H_4 [23], C_2H_5OH [24], … . Each precursor has its own decomposition temperature and therefore results in a different CNT growth temperature. Carbon atoms are supposed to be the end products of the decomposition and other species go away in gas phase. The released carbon radicals are very reactive since the unpaired electrons would like to combine with other electrons to form a filled outer shell of carbon [25], [26]. If the combination of carbon radicals happens without a crystalline nucleation, amorphous carbon is formed.

The formation of radicals requires energy which goes into the breaking of the bonds in the hydrocarbon precursor, and higher temperature leads to a larger number of radicals. For this reason, choosing a suitable carbon precursor for the CVD growth process is very important for achieving high quality SWNTs. A thermal stable hydrocarbon like CH_4 may be preferred, since it is easier to control the decomposition rate [13].

The CVD process can be controlled not only by changing the temperature, but also by changing the gas flows. During the decomposition of hydrocarbon, hydrogen is released as in Eq. 2.6. This reaction equilibrium can be influenced by changing the relative concentration of the reactants and products. A big surplus of hydrogen slows down the decomposition reaction of the hydrocarbon (Eq. 2.7) [27], [28].

$$CH_4 \rightarrow H_3C^{\bullet} + H^{\bullet} \rightarrow H_2C^{\bullet\bullet} + 2H^{\bullet} \rightarrow HC^{\bullet\bullet\bullet} + 3H^{\bullet} \rightarrow C^{\bullet\bullet\bullet\bullet} + 4H^{\bullet} \quad (2.6)$$

$$H_2 + H_3C^{\bullet} \rightarrow CH_4 + H^{\bullet} \quad (2.7)$$

In addition, the partial pressure of the species can affect the dissociation rates of the precursor. For example in a HiPCO process [29], high pressure CO is used to increase the dissociation rate and hence to achieve higher CNT yield. On the contrary, low pressure CVD has been used to decrease the decomposition rate and thus the catalyst poisoning to achieve ultra long CNTs [30].

2.4.2. Growth mechanism

Due to the small size of the catalyst nanoparticles and of the grown CNTs, the high reaction rate and the high temperature of the CVD process, it is very difficult to follow different steps of the nanotube growth. This motivates the recent development of experiments with *in situ* characterization during the growth [31–33]. Despite many aspects of the CNT growth mechanisms are unclear and still in argument, the Vapor-Liquid-Solid (VLS) mechanism is generally accepted [13], [20]. In this mechanism, catalyst nanoparticles play a very important role in decomposing hydrocarbon precursor and initiating the nanotube growth.

Figure 2.7 illustrates the different steps of the CNT growth following the VLS mechanism. First, the hydrocarbon molecules are adsorbed and catalytically decomposed on the nanoparticle surface. The released hydrogen (Eq. 2.6) then reduces the catalyst locally, and the released carbon atoms dissolve into the nanoparticle to form a metal-carbon solid state solution layer. When an over-saturation state of this solution is reached, the carbon precipitation happens leading to the formation of a cap and then of a CNT with sp^2 structure. Tubular shape is favorable since it contains no dangling bonds and has a lower energy than other forms of carbon, such as graphitic sheets with open edges. The CNT continues to grow from the particle until a termination happens, when the carbon supply is not enough or the catalyst particle loses its activity (catalyst poisoning). Figure 2.8 shows the TEM images of SWNTs grown from catalyst nanoparticles.

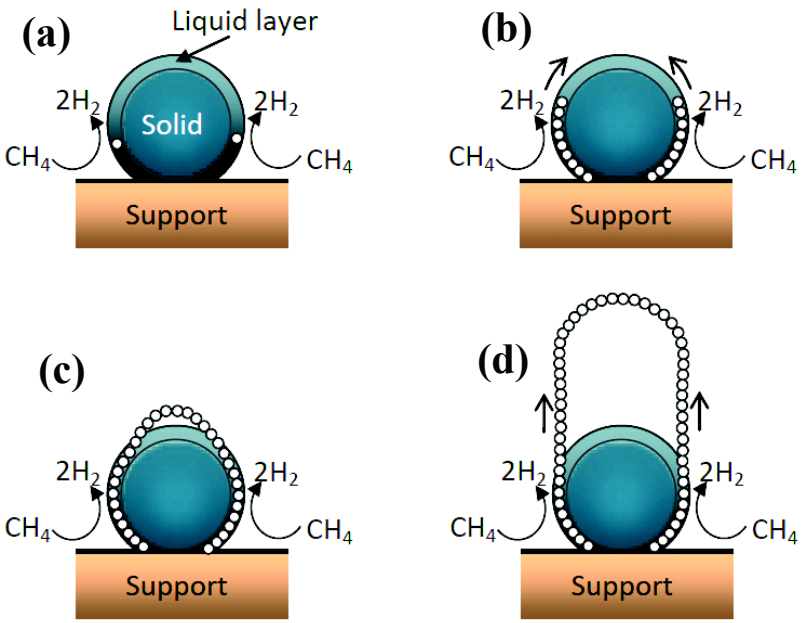

Figure 2.7. A schematic view of CNTs formation by VLS mechanism. (a) Adsorption and decomposition of the hydrocarbon. (b) Diffusion of carbon atoms in the liquid surface layer of the particle. (c) Over-saturation of the surface and formation of the cap. (d) Growth of the CNT. Adapted from ref. [34].

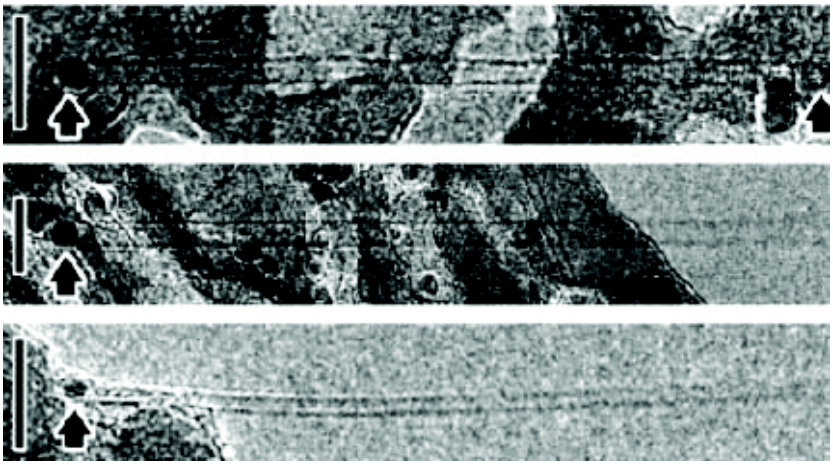

Figure 2.8. TEM images of SWNTs grown from catalyst particles [35]. The nanotube diameter is related to the catalyst particle size.

2.4.3. The catalyst

In chemistry, transition metals are widely used as catalysts for many reactions. A transition metal is an element whose atom has an incomplete d sub-shell so that it easily lends and takes electrons from other molecules, which is required for a chemical reaction. Catalysts thus provide an alternative, lower-energy pathway for the reaction to take place [36]. Equation 2.8 shows the incomplete sub-shell of a Fe atom.

Fe $4s^2\ 3d^6$: 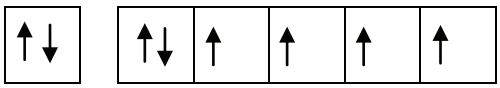 (2.8)

In a controlled growth, the catalytic decomposition of hydrocarbon is prominent. The growth temperature is thus lower than the thermal decomposition of the hydrocarbon source, which helps to avoid the formation of amorphous carbon. At growth temperatures, the catalyst particles adsorb and promote the decomposition of the hydrocarbon to form carbon radicals (Eq. 2.6). Each time a C-H or C-C bond is broken, one free electron will remain on the C (maximum 4 electrons). These radicals are very active and prefer to pair with other radicals they meet, that can terminate the reaction (Eq. 2.7). The transition metal, with incomplete d sub-shell (e.g. Eq. 2.8 for Fe), hence readily combines with the new released C atoms. The free electrons of the C radical pair with the haft-filled d orbitals of the catalyst, and the C atoms are adsorbed on the metal surface. If the catalyst has low (or zero) carbon solubility, these carbon atoms cannot go into the catalyst lattice, but stay on its surface and cover the whole particle. Amorphous carbon or onion-like graphic structures are formed without nanotube formation, and the catalyst particle then quickly loses its activity.

By checking different metal-carbon binary phase diagrams, [37], [38], one finds that only few metals have sufficient carbon solubility in the metal solid solution at the growth temperatures. Among them are Fe (~7 atomic percent (at.%) of C), Co (~2 at.%), Ni (~1 at.%) [39]. This prediction is in good agreement with the experiments, since these metals are the most commonly used catalysts for the CNT growth in a wide range of conditions. Other elements have either very low carbon solubility, or high solubility but there is multiple carbide formation before reaching the super-saturated state.

Figure 2.9 shows the phase diagram of Fe-C (in bulk materials). At the CVD growth temperature ~ 1000 °C, C atoms can insert into the Fe lattice, which first forms a metal solid solution named Austenite alloy (the orange dashed line). However, the carbide formation of FeC_3 requires more C atoms to be diffused and dissolved into the Fe lattice until 25 at.% (the red dashed arrow). Once passing this concentration, the system now becomes super-saturated and the C precipitation happens. The formation of carbide is thus not favorable for the growth of CNTs, since it consumes more C and Fe atoms of the CNT growth and needs more time for the C diffusion. The formed solid phase Fe_3C on the catalyst surface also reduces the diffusion rate of the reactants. To increase the yield and quality of the CNT growth, bimetallic catalysts have been used [40–42] instead of a single metal.

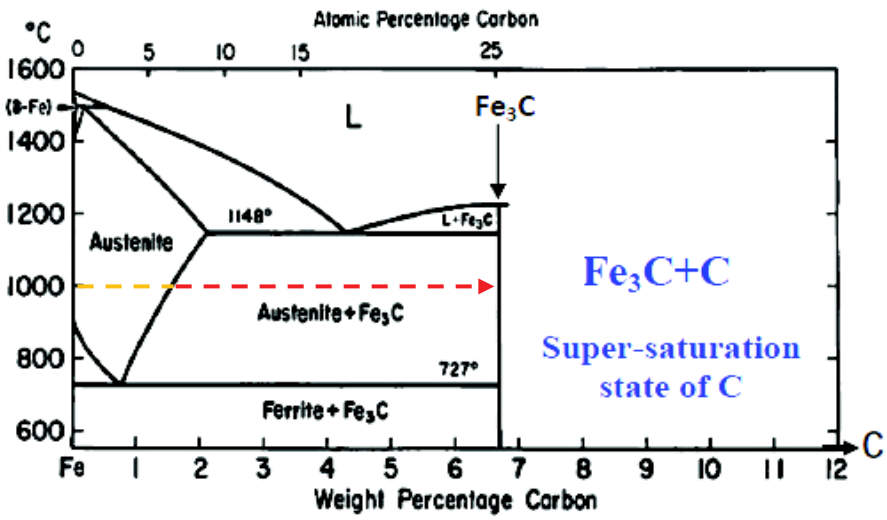

Figure 2.9. Fe-C phase diagrams of bulk materials [39].

As mentioned above, the catalytic hydrocarbon decomposition and carbon solubility are the key parameters for the CNT growth. While the later depends mostly on the catalyst composition, the former strongly depends on the particle size. For the CVD growth of CNTs, the size of catalyst particles varies from one to few tens of nanometers. When the size of the nanoparticle is reduced, the ratio of its surface atoms to internal atoms increases significantly. Since the surface atoms are electronically and coordinatively unsaturated, the smaller catalyst particles are more reactive than the larger ones. In the ideal case, one wants to prepare catalyst particles with the same size and composition, which are supposed to grow CNTs with the same diameter and chirality. However, these catalyst nanoparticles tend to aggregate at high temperatures of the CVD process, and the 'ideal CNTs' have not been obtained.

In the catalyst preparation, the metal nanoparticles are usually supported on an oxide, which is thermally and chemically stable under the synthesis conditions. The support increases the dispersion of the catalyst nanoparticles for the CNT growth. Strong metal-support interactions are needed to prevent the aggregation of nanoparticles, which could yield larger tubes or graphitic particles. Support oxides with a large surface area and a large pore volume are preferred. They can lead to high densities of catalytic sites, rapid diffusion and efficient supply of carbon feedstock to the catalytic sites [13], [41].

2.5. Conclusion

In this chapter, we gave an introduction on the nanotubes and their synthesis methods. Since the structures of the SWNTs decide their properties, a controlled synthesis of SWNTs is extremely important. Different synthesis methods were reviewed, among which the CVD was used for this thesis. We also described the main parameters of the CVD synthesis, which are useful for our experimental synthesis in the next chapter.

References

[1] B. Chandra, "Synthesis and Electronic Transport in Known Chirality Single Wall Carbon Nanotubes," Columbia, 2009.

[2] "Carbon allotropes." [Online]. Available: http://physics.bu.edu/~neto/Topic0.htm.

[3] M. S. Dresselhaus, G. Dresselhaus, and P. Avouris, Eds., *Carbon Nanotubes: Synthesis, Structure, Properties and Applications*, 1st ed. Springer, 2001.

[4] L. C. Venema, J. W. G. Wildoer, C. Dekker, G. A. Rinzler, and R. E. Smalley, "STM atomic resolution images of single-wall carbon nanotubes," *Applied Physics A: Materials Science & Processing*, vol. 66, no. 7, pp. S153–S155, Mar. 1998.

[5] "http://www.physics.berkeley.edu/research/zettl/projects/imaging.html," *http://www.physics.berkeley.edu/research/zettl/projects/imaging.html*. .

[6] K. S. Novoselov, A. K. Geim, S. V. Morozov, D. Jiang, M. I. Katsnelson, I. V. Grigorieva, S. V. Dubonos, and A. A. Firsov, "Two-dimensional gas of massless Dirac fermions in graphene," *Nature*, vol. 438, no. 7065, pp. 197–200, Nov. 2005.

[7] S. Reich, C. Thomsen, and J. Maultzsch, *Carbon Nanotubes: Basic Concepts and Physical Properties*. John Wiley & Sons, 2004.

[8] R. Saito, G. Dresselhaus, and M. S. Dresselhaus, *Physical Properties of Carbon Nanotubes*. Imperial College Press, 1998.

[9] J.-Y. Park, "Band Structure and Electron Transport Physics of One-Dimensional SWNTs," in *Carbon Nanotube Electronics*, Springer, 2009.

[10] E. D. Minot, "Tuning the band structure of carbon nanotubes," Cornell, 2004.

[11] P. D. Jarillo-Herrero, "Quantum transport in carbon nanotubes," TU Delft, 2005.

[12] C. L. Kane and E. J. Mele, "Size, Shape, and Low Energy Electronic Structure of Carbon Nanotubes," *Phys. Rev. Lett.*, vol. 78, no. 10, pp. 1932–1935, Mar. 1997.

[13] H. J. Dai, "Growth and Characterization of Carbon Nanotubes," in *Topics in Applied Physics*, vol. 80, Springer Verlag, 2000.

[14] "Arc discharge." [Online]. Available: http://en.rigaku-mechatronics.com/case/arc-discharger.html.

[15] B. I. Yakobson and R. Smalley, "Fullerene Nanotubes: C1,000,000 and Beyond," *American Scientist*, vol. 85, pp. 324–337, Jul. 1997.

[16] S. Iijima, "Helical microtubules of graphitic carbon," *Nature*, vol. 354, no. 6348, pp. 56–58, Nov. 1991.

[17] T. W. Ebbesen, *Carbon Nanotubes: Preparation and Properties*. CRC Press, 1997.

[18] C. D. Scott, S. Arepalli, P. Nikolaev, and R. E. Smalley, "Growth mechanisms for single-wall carbon nanotubes in a laser-ablation process," *Applied Physics A: Materials Science & Processing*, vol. 72, pp. 573–580, 2001.

[19] F. Kokai, K. Takahashi, M. Yudasaka, and S. Iijima, "Growth dynamics of single-wall carbon nanotubes synthesized by laser ablation," in *Microprocesses and Nanotechnology Conference, 2000 International*, 2000, p. 234.

[20] M. Kumar and Y. Ando, "Chemical vapor deposition of carbon nanotubes: a review on growth mechanism and mass production," *J Nanosci Nanotechnol*, vol. 10, no. 6, pp. 3739–3758, Jun. 2010.

[21] H. J. Dai, A. G. Rinzler, P. Nikolaev, A. Thess, D. T. Colbert, and R. E. Smalley, "Single-wall nanotubes produced by metal-catalyzed disproportionation of carbon monoxide," *Chemical Physics Letters*, vol. 260, no. 3–4, pp. 471–475, Sep. 1996.

[22] J. Kong, A. M. Cassell, and H. Dai, "Chemical vapor deposition of methane for single-walled carbon nanotubes," *Chemical Physics Letters*, vol. 292, no. 4–6, pp. 567–574, Aug. 1998.

[23] M. J. B. Jason H. Hafner, "Catalytic growth of single-wall carbon nanotubes from metal particles," *Chemical Physics Letters*, pp. 195–202.

[24] S. Maruyama, R. Kojima, Y. Miyauchi, S. Chiashi, and M. Kohno, "Low-temperature synthesis of high-purity single-walled carbon nanotubes from alcohol," *Chemical Physics Letters*, vol. 360, no. 3–4, pp. 229–234, Jul. 2002.

[25] D. A. F. Parsons, *An Introduction to Free-Radical Chemistry*, 1st ed. Wiley-Blackwell, 2000.

[26] M. J. Perkins, *Radical Chemistry: The Fundamentals*, 1st ed. Oxford University Press, USA, 2001.

[27] R. I. Masel, *Chemical Kinetics and Catalysis*. John Wiley & Sons, Inc., 2001.

[28] N. R. Franklin, Y. Li, R. J. Chen, A. Javey, and H. Dai, "Patterned growth of single-walled carbon nanotubes on full 4-inch wafers," *Applied Physics Letters*, vol. 79, no. 27, pp. 4571–4573, Dec. 2001.

[29] P. Nikolaev, M. Bronikowski, K. Bradley, F. Rohmund, D. Colbert, K. Smith, and R. Smalley, "Gas-phase catalytic growth of single-walled carbon nanotubes from carbon monoxide," *Chemical Physics Letters*, vol. 313, no. 1–2, pp. 91–97, Nov. 1999.

[30] T. Ikuno, M. Katayama, N. Yamauchi, W. Wongwiriyapan, S. Honda, K. Oura, R. Hobara, and S. Hasegawa, "Selective Growth of Straight Carbon Nanotubes by Low-Pressure Thermal Chemical Vapor Deposition," *Japanese Journal of Applied Physics*, vol. 43, no. 2, pp. 860–863, Feb. 2004.

[31] H. Yoshida, T. Shimizu, T. Uchiyama, H. Kohno, Y. Homma, and S. Takeda, "Atomic-Scale Analysis on the Role of Molybdenum in Iron-Catalyzed Carbon Nanotube Growth," *Nano Lett.*, vol. 9, no. 11, pp. 3810–3815, 2009.

[32] E. Einarsson, "Growth dynamics of vertically aligned single-walled carbon nanotubes from in situ measurements," *Carbon*, vol. 46, no. 6, p. 923, May 2008.

[33] S. Hofmann, R. Sharma, C. Ducati, G. Du, C. Mattevi, C. Cepek, M. Cantoro, S. Pisana, A. Parvez, F. Cervantes-Sodi, A. C. Ferrari, R. Dunin-Borkowski, S. Lizzit, L. Petaccia, A. Goldoni, and J. Robertson, "In situ Observations of Catalyst Dynamics during Surface-Bound Carbon Nanotube Nucleation," *Nano Lett.*, vol. 7, no. 3, pp. 602–608, 2007.

[34] J. Furer, "Growth of Single-Wall Carbon Nanotubes by Chemical Vapor Deposition for Electrical Devices," Basel, 2006.

[35] Y. Zhang, Y. Li, W. Kim, D. Wang, and H. Dai, "Imaging as-grown single-walled carbon nanotubes originated from isolated catalytic nanoparticles," *Applied Physics A: Materials Science & Processing*, vol. 74, no. 3, pp. 325–328, 2002.

[36] "Transition metals." [Online]. Available: http://en.wikipedia.org/wiki/Transition_metal.

[37] D. R. Lide, Ed., *Hand book of Chemistry and Physics 75th Edition*, 75th ed. CRC Press, 1994.

[38] A. S. for Metals, *Metals Handbook, Volume 8: Metallography, Structures and Phase Diagrams. 8th Edition*, 8th ed. American Society for Metals, 1973.

[39] C. P. Deck and K. Vecchio, "Prediction of carbon nanotube growth success by the analysis of carbon–catalyst binary phase diagrams," *Carbon*, vol. 44, no. 2, pp. 267–275, Feb. 2006.

[40] E. Lamouroux, P. Serp, and P. Kalck, "Catalytic Routes Towards Single Wall Carbon Nanotubes," *Catalysis Reviews*, vol. 49, no. 3, pp. 341–405, 2007.

[41] A. M. Cassell, J. A. Raymakers, J. Kong, and H. Dai, "Large Scale CVD Synthesis of Single-Walled Carbon Nanotubes," *J. Phys. Chem. B*, vol. 103, no. 31, pp. 6484–6492, 1999.

[42] W. E. Alvarez, B. Kitiyanan, A. Borgna, and D. E. Resasco, "Synergism of Co and Mo in the catalytic production of single-wall carbon nanotubes by decomposition of CO," *Carbon*, vol. 39, no. 4, pp. 547–558, Apr. 2001.

Chapter 3. Synthesis and characterization of single wall carbon nanotubes

3.1. Motivation

The goal of this thesis is to fabricate CNT devices and to study the electrical properties of the CNTs using these devices. In the common method of device fabrication, people usually use synthesized CNTs in a bulk form. The CNTs are first dispersed in a solution by sonication, spin coated on a surface, located by AFM or SEM, and finally connected with metal leads by using lithography and e-beam evaporation. All chemical treatment and fabrication processes may damage and contaminate the CNTs, and at the end these devices are not so good for the transport measurements [1]. For this reason, the trend on recent studies is to grow the CNTs directly on a surface using as few treatment steps as possible. Among the available synthesis methods, CVD is the only technique that can adapt this requirement [2].

At the beginning it was thought that high crystallized CNTs are formed only at high temperature arc discharge or laser ablation processes. Later, it was found that the CVD can also grow CNTs with a high crystallization [2], [3]. However, these synthesized CNTs can be either SWNTs or MWNTs, and they have a large range of diameter distribution. In addition, there could be also amorphous carbon and other unwanted by-products. The utilization of these randomly grown materials for the electrical transport measurements is thus a limitation for the deeper studies of CNT properties and their applications. Therefore, a selective growth of the CNTs of a wanted type is very important.

In this chapter, we try to synthesize the SWNTs in a more “controlled” manner. This is achieved by altering different growth parameters, such as the carbon precursors, temperatures, and especially the catalysts. After characterizing carefully the CNT grown at each condition, we find the optimal growth parameters for high quality SWNTs. All the possible information about the grown CNTs is studied. We can then utilize these synthesis conditions for a direct growth of CNTs on our devices and thus, we have a high certainty of the kind of CNTs which are connected and measured.

First, we describe the details of the experiments including the CVD setup, catalyst, sample preparation, and characterization techniques in the section 3.2. The optimization of CVD conditions including the use of different carbon precursors, gas flows, and temperature are then explained in section 3.3. The optimal CVD condition should lead to a growth of long, straight and well separated CNTs, as well as minimum formation of amorphous carbon. Section 3.4 describes the optimization of the catalyst composition for the synthesis of high quality SWNTs by studying two different catalyst systems, Fe-Mo and Fe-Ru. The grown CNTs corresponding to each catalyst composition are characterized and compared, which helps us to found the optimal high selectivity growth recipe for SWNTs with narrow diameter distribution.

3.2. Description of experiments

3.2.1. CVD setup

In this work, we used a commercial CVD setup (Easy Tube 2000 from the FirstNano company) for which we adapted several home-made technical modifications (Fig. 3.1). In Fig. 3.1b, we can see the whole reaction chamber, which is placed inside a “big box” and connected to an exhaust in order to operate the system in a safe condition.

The system typically includes a furnace with two clamped heaters surrounding a quartz tube of 4 inches diameter. The maximum operating temperature of the furnace is about 1100 °C, although we mainly used it in the processing range of 700 – 900 °C. The samples are transferred from a cold loadlock chamber into the furnace, operating at the desired temperature and desired gas flow conditions. The sample loading/unloading is made at a controlled speed, using the magnetic rod attached to the sample holder. The available gases are CH_4, C_2H_4, Ar and H_2. While CH_4 and C_2H_4 are used as the carbon precursors, Ar is simply an inert carrier gas and H_2 is mainly used to control the growth dynamics and to minimize the amount of amorphous carbon. Besides, the CVD system is equipped with a “bubbler” used to provide a controlled amount of vaporized liquid (typically C_2H_5OH as another possible carbon precursor). The different gas lines are controlled by electronic mass flow controllers allowing the flow rates up to 2 SLPM (Standard Litre Per Minute).

Moreover, the CVD setup is equipped by a roots pump with a base pressure of 50 mTorr, which enables a low pressure operation as well as removing the reacting gases from the chamber after the growth procedure.

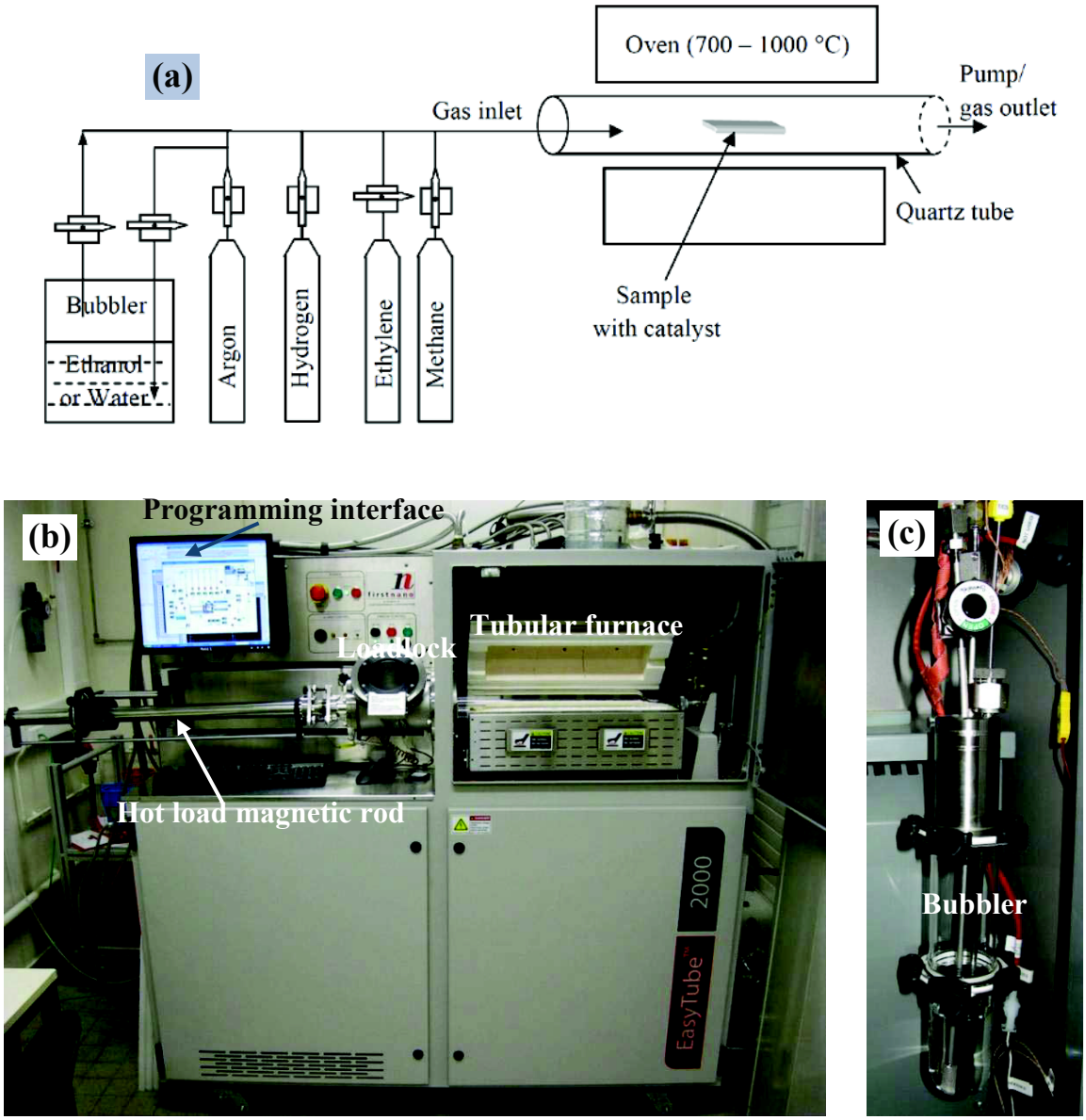

Figure 3.1. Our CVD system for the synthesis of CNTs. (a) Simplified scheme. (b) The EasyTube 2000 CVD system. (c) The bubbler is used to inject controlled amount of vapor from liquid precursor.

The whole system is operated through a real time controlled interface (Fig. 3.2). It makes possible to control all the operating conditions, as well as programming and editing the recipes.

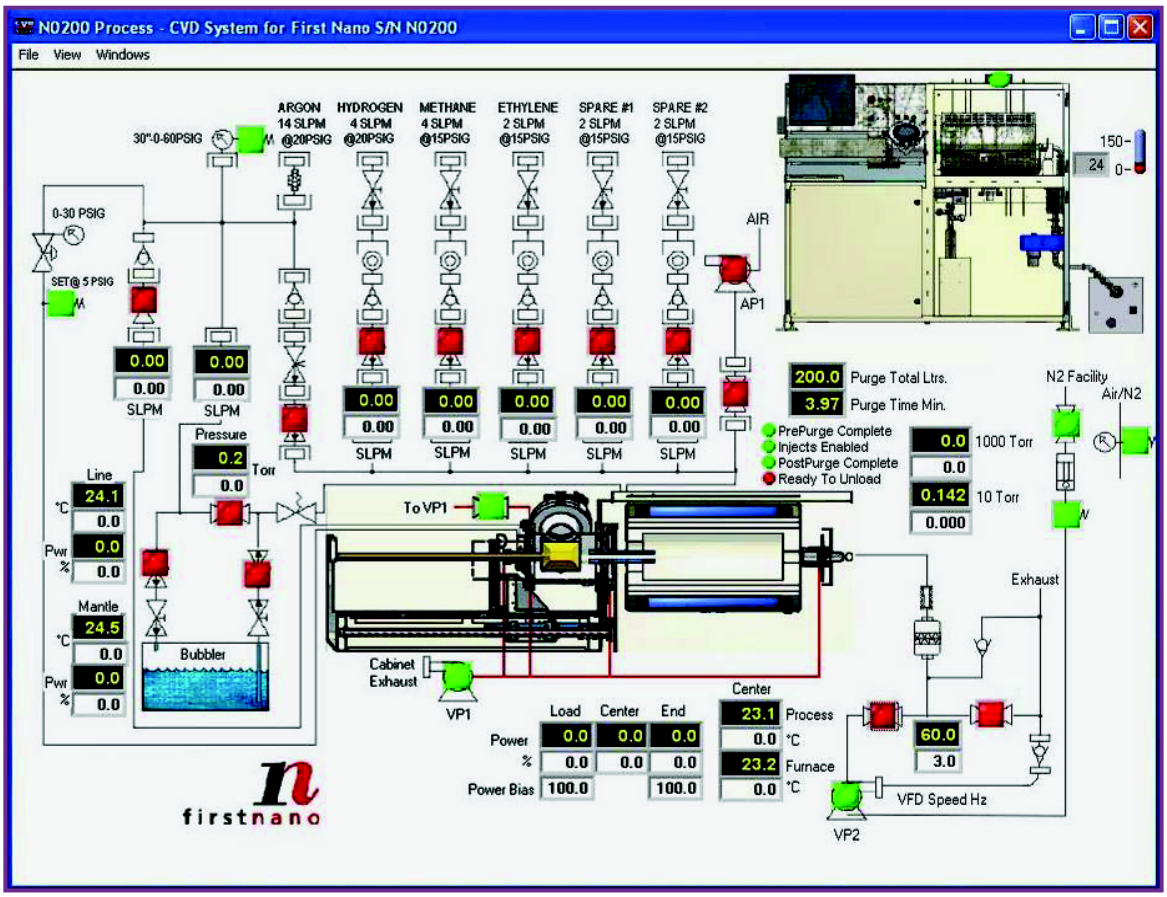

Figure 3.2. The user interface of the EasyTube 2000 CVD system. All the process parameters like temperature, gas flows, growth duration, sample loading/unloading are controlled by the software.

3.2.2. Catalyst composition and preparation

The preparation of the catalyst is a crucial part in the process due to its important role in the CNT growth. Many methods have been developed in the past years to prepare catalyst nanoparticles utilizing either physical [4] (e.g. de-wetting of a very thin metal film) or chemical [5], [6] approaches.

The most common and simple method is a solution, in which the metal salts (nitrates, chlorides or sulfates) and the support oxides are dissolved in a suitable solvent. The advantage of this method is that the chemical composition of the catalyst can be changed

easily. Another technique of catalyst preparation is thin film evaporation. A thin film (~ 1 nm) of metal catalyst is evaporated on a substrate, which is then exposed to controlled annealing treatments [4]. Although this technique can form relatively uniform catalyst particles, the ability to alter their chemical composition is limited. Moreover, some uniformly sized catalysts such as ferritin [7], dendrimer complexes [8], and molecular nanoclusters [9] have been prepared.

The catalysts used in this work are prepared by a chemical method in a solution. The nanoparticles are formed inside small nanopores of the support oxide. Following the previous works, we tried different kinds of support oxide nanoparticles, such as MgO [10], SiO_2 [6] and Al_2O_3 [11] (from Degussa and Sigma Aldrich). All the different support oxides gave different results in terms of CNT diameters, catalytic activity. We chose Al_2O_3 from Sigma Aldrich (mean nanoparticle size ~ 50 nm), which gave the best results, to be used in the rest of this work. The support oxide nanoparticles are impregnated by metal salts in a solvent, followed by 30 – 60 minutes of sonication. The solvent can be any of the following H_2O, isopropanol, or methanol. While H_2O gave rise to an aggregation of the support oxide particles, the dispersion of the Al_2O_3 particles was much more efficient in methanol. As a transition metal based salt, we used $Fe(NO_3)_3.9H_2O$, which gives Fe nanoparticles. In this work, we used two Fe catalyst systems, where the Fe based salt is mixed respectively with MoO_2 and $Ru(C_5H_8O_2)_3$ to form bimetallic Fe-Mo and Fe-Ru based nanoparticles [6], [12–14]. The bimetallic nanoparticles gave the best results and are depicted in the section 3.4. The used chemical agents are listed in Table 3.1.

Table 3.1. The chemicals used for the catalyst preparations [15]. The Fe-Mo catalysts base on $Fe(NO_3)_3.9H_2O$ and MoO_2. The Fe-Ru catalysts base on $Fe(NO_3)_3.9H_2O$ and $Ru(C_5H_8O_2)_3$.

Compound	**Molecular weight (g/mol)**	**Supplier, form**
Al_2O_3	101.96	Sigma Aldrich, nanopowders (d < 50nm)
$Fe(NO_3)_3.9H_2O$	404.02	Sigma Aldrich, powder
MoO_2	127.94	Sigma Aldrich, powder
$Ru(C_5H_8O_2)_3$	398.40	Sigma Aldrich, powder
CH_3OH	32.04	Sigma Aldrich, liquid

3.2.3. Local deposition of the catalyst on a surface

Since we are interested in the growth of isolated CNTs on a surface, we developed a technique to deposit a needed amount of catalyst, so called the "catalyst islands" controlled in both size and position. The deposition of the catalyst is done just before the CVD growth.

The substrate is a Si wafer covered by a SiO_2 oxide layer (Fig. 3.3a). The preparation of the samples starts with the patterning of the catalyst islands by either electron beam lithography or optical deep UV lithography (Fig. 3.3b). We used here LOR 3A resist (600 nm thickness) which has the advantage of being quite thick (good for the catalyst lift-off) and very resistant to the methanol solvent. The catalyst solution is then spin coated on the patterned resist and baked at 100 °C for 60 seconds (Fig. 3.3c). The coat-bake steps can be repeated for several times to get a high enough catalyst density. After lifting-off the LOR 3A resist by PG remover, we have catalyst islands of predefined size (Fig. 3.3d). After the deposition, the catalyst must be calcinated to remove all chemical contamination on the nanoparticle which is commonly done by high temperature oxidation in an air or oxygen atmosphere [6]. In this work, we used O_2 plasma treatment for 15 minutes instead of the high temperature process. Figure 3.4 shows an example of a sample that is ready for the CVD growth.

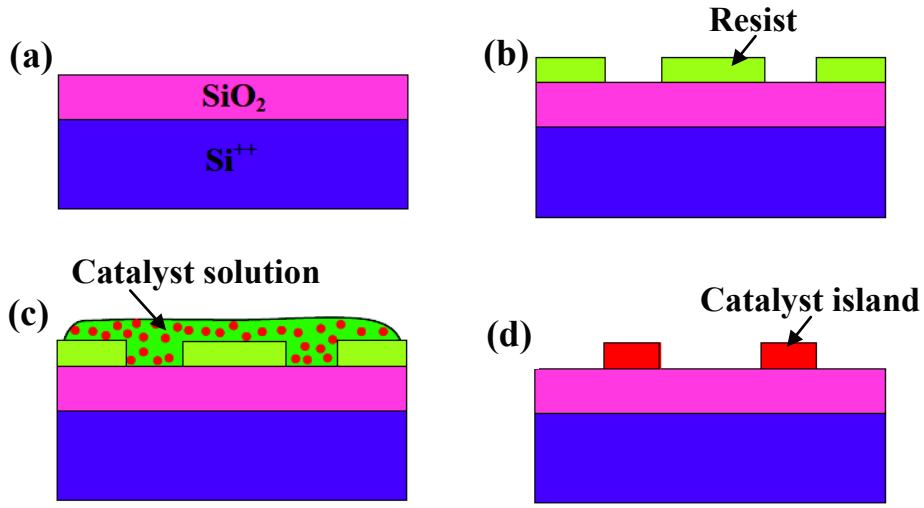

Figure 3.3. Catalyst deposition on a substrate. (a) Substrate preparation, (b) Patterning of a resist mask by lithography, (c) Spin coating of the catalyst solution and baking, (d) Lift-off of the resist.

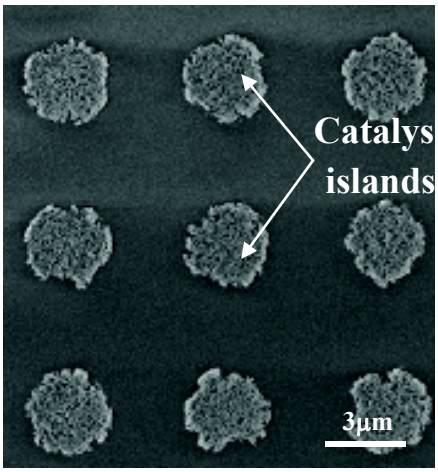

Figure 3.4. Localized deposition of the catalytic nanoparticles on a surface. Each of the catalyst islands contains many nanoparticles.

3.2.4. Characterization methods

Samples are characterized after the CVD growth by using several techniques which are available at the Néel Institute. ***Scanning Electron Microscope*** (SEM, Zeiss ULTRA PLUS system) is the first and most common characterization tool for the as-grown samples. It provides information about the length and density of the CNTs. ***Atomic Force Microscope*** (AFM, VEECO Dimension 3100) gives information about the nanotube diameters and may indicate traces of amorphous carbon on the sample surface. ***Resonant Raman Spectroscopy*** (Witec system with 532/633 nm laser wavelengths) provides information about the internal structure of the CNTs [16]. By studying the graphite band (G-band at $\omega \sim 1600$ cm^{-1}) of the Raman spectra, we can distinguish whether the grown CNTs are SWNTs or DWNTs, metallic or semiconducting, individual or bundled. The defect band (D-band at $\omega \sim 1330$ cm^{-1}) can give us information about the CNTs crystallinity, the defect rate, and the amorphous carbon on the sample. The radial breathing mode (RBM at $\omega \sim 100 - 300$ cm^{-1}), from which we can estimate the CNT diameter, is the indication of SWNTs. More information about Resonant Raman Spectroscopy of CNTs can be found in ref. [16].

The most important and intensively used technique in this chapter is ***Transmission Electron Microscopy*** (TEM, Philips CM 300 system), which gives direct and obvious information about the internal structure of the CNTs such as nanotube diameter, number of walls, defects, amorphous carbon, and other kinds of carbon products. The TEM grid used in

this work is a 50 nm thick Si_3N_4 membrane (Fig. 3.5b, c) which is bought from SPI Supplies. The catalyst solution is dispersed on the TEM grid by using drop casting technique. The grids with catalyst nanoparticles are then used as other common samples for oxygen plasma cleaning and CVD growth. The TEM images of the CNTs on these TEM grids are taken at 150 kV acceleration voltage. We captured 200 – 400 TEM images of the CNTs grown from each of the catalyst compositions. Images are then used for the statistical analysis of the nanotubes diameter distribution and the selectivity of SWNTs/MWNTs. The Philips CM 300 TEM system is shown in Fig. 3.5a.

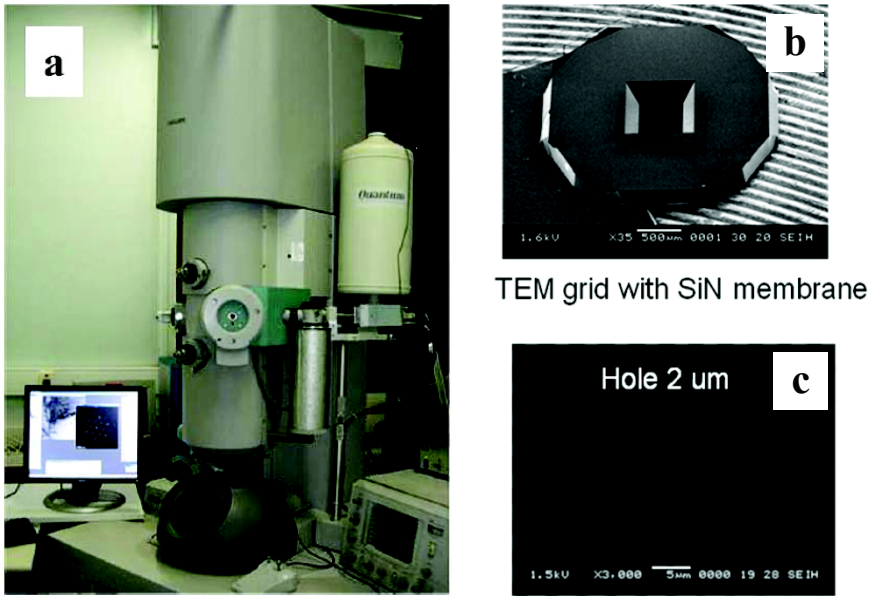

Figure 3.5. TEM for characterization of CNTs. (a) Philips CM-300 system (HT: 150-300 kV). (b) SiN grid and (c) its membrane for the catalyst deposition and CNT growth.

3.3. Optimization the CVD synthesis conditions

The two first and foremost important tasks in carbon nanotube CVD growth are the choosing of the carbon precursor and the optimization of the growth conditions. With the EasyTube 2000 system we can use three different precursor CH_4, C_2H_4 and C_2H_5OH. With each precursor we tried to optimize the gas flows, growth temperature and growth duration to achieve high quality SWNTs. The general protocol of a CVD process is shown in Fig. 3.6.

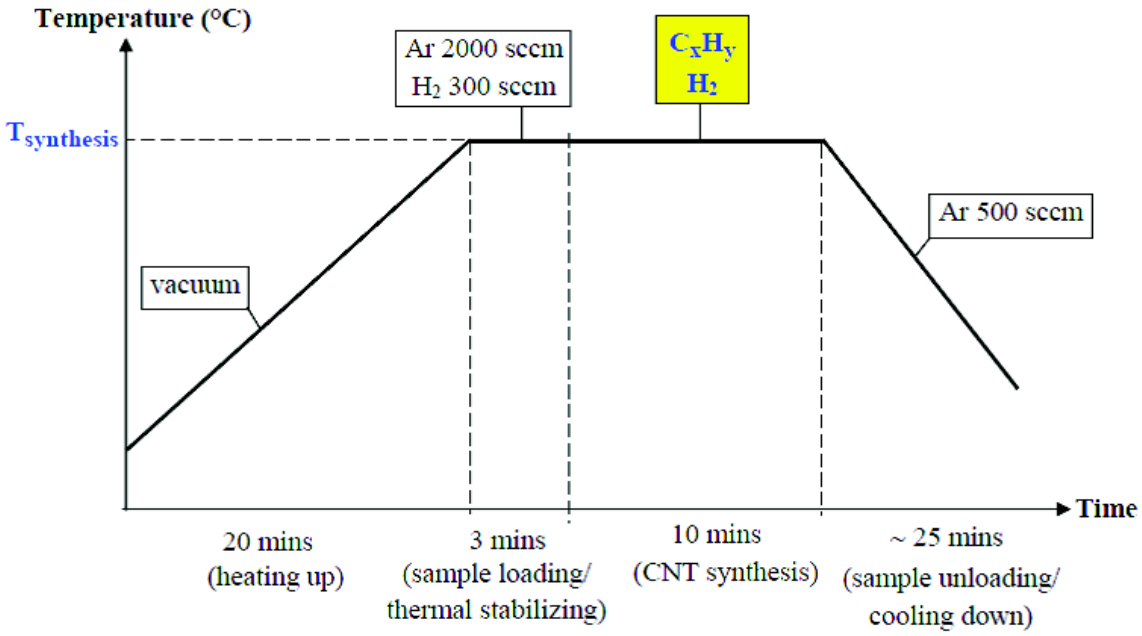

Figure 3.6. A general protocol of a CVD process. The studied parameters: carbon precursor, gas flows, and growth temperature.

In the thermal catalyst CVD high temperature is necessary. It provides the energy to break the bonds of the hyrdocarbon precusor and to excite the nanoparticles for catalyzing the CNT growth (see section 2.4). The carbon precusor should be stable against self-decomposition at the CVD temperature and the catalytic hydrocarbon decomposition is a prominent process. These can lead to a growth of high quality SWNTs with low amorphous carbon overcoating. In this section, we use catalyst Fe-Mo #3 (see section 3.4 for more details) for the optimization of the CVD processes.

3.3.1. Methane CVD

For the methane CVD, the growth temperature is tested in the range of 700 – 900 °C [17]. The methane flow is varied from 800 to 1800 sccm (1 sccm = 1/1000 SLPM), and the hydrogen flow is in a range of 300 to 1200 sccm.

Effect of the growth temperature

To study the effect of temperature on the nanotube growth, we fix the gas flows at 1200 sccm of CH_4 and 700 sccm of H_2 and the growth period in 10 minutes. At low temperature of 700 °C the nanotubes start to grow but they are quite short (1 – 2 μm) and low in density (Fig. 3.7a). Increasing the CVD temperature to 800 °C leads to a growth of longer tubes (3 – 15 μm) (Fig. 3.7b). These CNTs are quite straight ad their density is moderate. However, when the temperature goes up to 900 °C, many CNTs grow from the catalyst island but with a significant amount of amorphous carbon (Fig. 3.7c). At this temperature the CH_4 is supposed to self-decompose with high rate [17]. In addition, there are also many broken short tubes on the sample, which may be due to the fact that the catalyst nanoparticles start to evaporate at this high temperature or some elements from the substrate (or electrodes) start acting as catalyst for the growth.

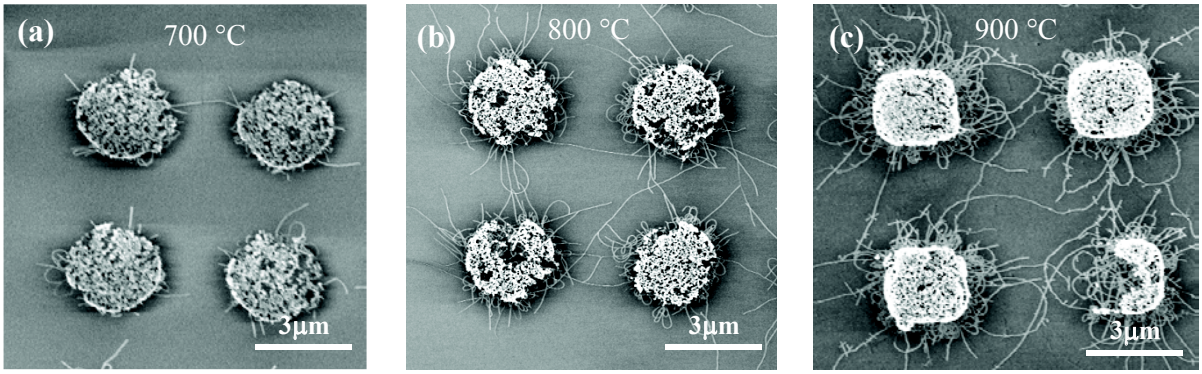

Figure 3.7. Nanotubes grown at (a) 700 °C, (b) 800 °C, and (c) 900 °C. The gas flows are fixed at 1200 sccm of CH_4 + 700 sccm of H_2, and the duration is 10 minutes.

We also check the effect of growth temperature by TEM imaging. These images show that the CNTs grown on Si_3N_4 grid at 800 °C temperature (Fig. 3.8a) are very clean from amorphous carbon. Most of the nanotubes are well crystallized SWNTs and they have diameters in a range of 1 – 3 nm. On the contrary, the CNTs grown at 900 °C are contaminated by amorphous carbon (Fig. 3.8b) which is found on the sides of the tubes. Moreover, larger tubes and higher percentage DWNTs are observed at this high CVD temperature, which may be due to the fact that the catalyst nanoparticles start to aggregate to form larger size particles [3]. In the C radicals rich environment created by the self-dissociation of CH_4, not only the small particles but also the larger ones have enough energy to catalyze the CNT growth [18].

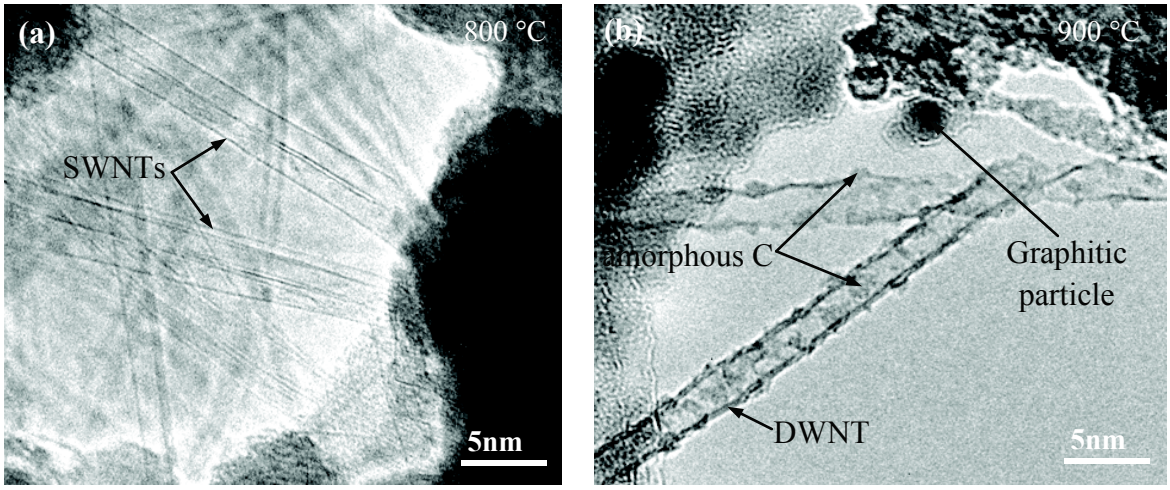

Figure 3.8. TEM images of CNTs grown at (a) 800 °C, and (b) 900 °C with gas flows 1200 sccm CH_4 + 700 sccm H_2 for 10 minutes. A high CVD temperature of 900 °C leads to the formation of amorphous carbon, graphitic particles and DWNTs.

After all the characterizations we find out that the temperature of 800 °C is the best for the growth of SWNTs in terms of the tube quality, diameter, length, density, and as well as the absence of amorphous carbon.

Effect of gas flows

Optimization of the gas flows of CH_4 and H_2 is done by "try and check" approach since there are two variabes of gas. This step is very time consuming and all the efforts cannot be described in details here. Therefore, we just present the main conditions which give significant changes in the CNT growth. In the following, the growth condition has been fixed to 800 °C and 10 minutes according to what we have found ealier. The catalyst Fe-Mo #3 is also chosen to be used in this step.

First, we want to study the effect of carbon supply. We fix the H_2 flow at 700 sccm and vary the CH_4 flow in a range from 700 to 1700 sccm. At low flow rate of 700 sccm CH_4 the grown CNTs are quite short (1 – 4 μm) and low in density (Fig. 3.9a). It seems that the used carbon supply is not enough for sustainable growth of CNTs. When we increase the CH_4 to 1700 sccm, the density of CNTs is larger but their straightness is worse (Fig. 3.9b). Although there are few tubes longer than before (some of them up to 15 μm), most of the remaining CNTs are quite short (~1 μm) and curved. Moreover, the higher magnification SEM image in Fig. 3.9c shows the presence of amorphous carbon and some broken short tubes. It seems that 1700 scmm CH_4 is too high a flux for the carbon supply forming an abundant amount of C radicals and thus amorphous carbon.

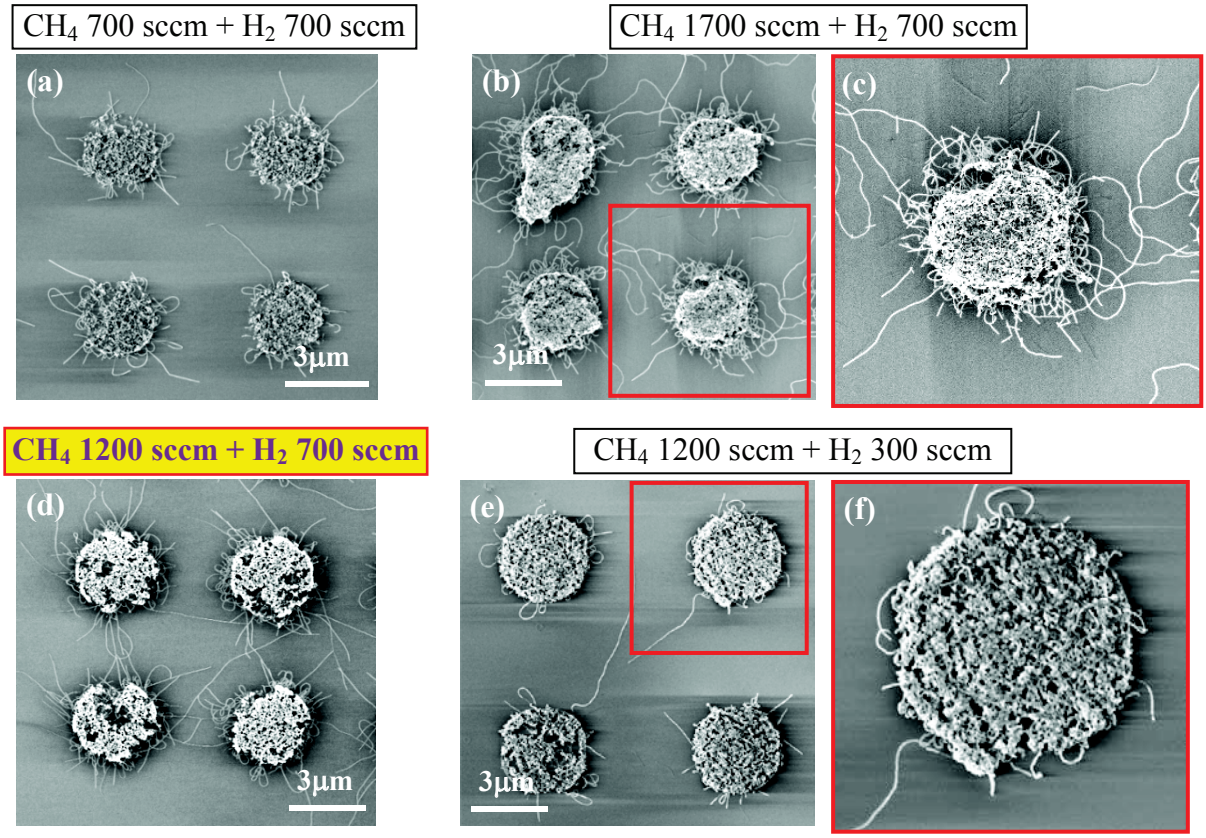

Figure 3.9. Optimization of the gas flows. From (a) to (d): H_2 flow is fixed at 700 sccm and CH_4 flow is varied from 700 sccm to 1700 sccm. (a) Low CH_4 flow of 700 sccm forms short CNTs. (b,c) A high CH_4 supply of 1700 sccm forms curved tubes and amorphous carbon. (d) A proper flow rate of 1200 sccm CH_4 + 700 sccm H_2 leads to the best growth in terms of straight and long CNTs. (e,f) The CH_4 flow is fixed at 1200 sccm and H_2 flow is reduced to 300 sccm. Low H_2 concentration favors the formation of amorphous carbon which can terminate the CNT growth after a short period of time.

Continue to tune the CH_4 flow, we find out that the flow rate of 1200 sccm CH_4 + 700 sccm H_2 leads to the wanted growth of CNTs (Fig. 3.9d). The nanotubes are straight, long (3 – 15 μm) and their number density is moderate. A TEM image of a sample grown in this condition shows that the CNTs are very clean and without any amorphous carbon coating (Fig. 3.8a).

In addition, we also study the effect of the H_2 flow on the CNT growth. The CH_4 flow is fixed at 1200 sccm and the H_2 flow is varied from 300 to 1200 sccm. When the H_2 flow is 300 sccm, it is too low and there are not so many CNTs growing (Fig. 3.9e, f). The equation 2.7 describes the role of H_2, which is keeping the proper formation rate of carbon radicals in the process. Moreover, H_2 is needed to reduce the catalyst from the other state to the metal, which has the catalytic properties [19]. During the growth, H_2 also removes the amorphous carbon forming on the particle surface that increases the diffusion of carbon atoms into the catalyst nanoparticle for the growth of longer nanotubes. However, too high a flow of H_2 of 1200 sccm is not good for the CNT growth neither. The SEM image of these samples (not shown) looks quite similar to that of Fig. 3.7b.

It is clear that a suitable ratio of CH_4:H_2 is the crucial parameter for growing nanotubes. This ratio keeps the balance of the hydrocarbon decomposition reaction to a constant rate, which is necessary for a stable growth of nanotubes. However a question is that, is the growth influenced or not if we keep the same gas ratio but alter the value of the total flow. We keep the CH_4:H_2 ratio at 1.71 (1200/700) but reduced the real values of CH_4 and H_2 flows to 800 sccm and 460 sccm, respectively. The SEM image after this process showed that the grown nanotubes are shorter and not straight (Fig. 3.10a).

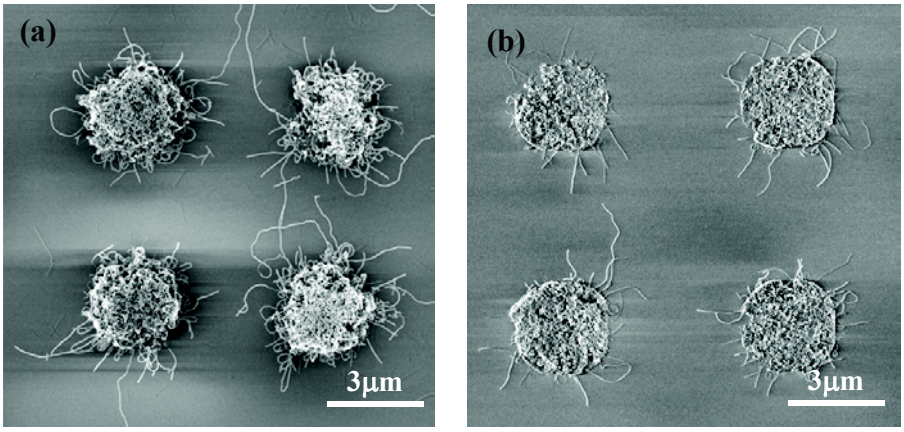

Figure 3.10. CNTs grown with (a) 800 sccm CH_4 + 460 sccm H_2 in 10 minutes, and (b) 1200 sccm CH_4 + 700 sccm H_2 in 1 minute.

Effect of growth time

The effect of the growth time on the nanotubes was also studied. Figure 3.10b are nanotubes grown with the optimized CVD parameters except the growth time, which is just 1 minute instead of 10 minutes. After the first minute the CNTs have already reached the length of 1-3 μm. On the contrary, samples grown for 60 minutes do not give much longer tubes than that of 10 minutes. For this reason, we chose the growth period of 10 – 15 minutes for our applications. Too long a growth process can increase the possibility to form more amorphous carbon due to hydrocarbon thermal decomposition.

Conclusion

We presented the main charateristics of the optimization process of methane CVD. We found an optimal condition for the CNT growth, which is at 800 °C using 1200 sccm CH_4 + 700 sccm H_2 for 10 minutes. These parameters lead to a growth of high quality CNTs which are long, straigth, and their number density is moderate. This was found out by altering growth parameters including temperature, gas flows and growth duration and characterizing the grown tubes. Very little amorphous carbon is formed on the sample, which is proved by the high resolution TEM observations.

3.3.2. Ethylene CVD

The ethylene (C_2H_4) precursor has a higher thermal decomposition rate than methane due to the π-bond in its molecule [21]. In our ethylene CVD process, we try with a very small flow of C_2H_4 in the range of 15 – 30 sccm while keeping the high flow rate for H_2. The Fe-Mo catalyst #3 is also used in this work. At temperature about 750 °C, the CNTs start to grow but there is also amorphous carbon formation (Fig. 3.11).

First, we fix the C_2H_4 at 15 sccm and vary the H_2 flow in a range of 200 – 900 sccm from one CVD run to another. At low H_2 concentration of 200 sccm growth (Fig. 3.11a), there is a lot of amorphous carbon covering the catalyst and the substrate. The H_2 flux is then increased to 600 sccm (Fig. 3.11b), which leads to a cleaner sample. Unfortunately, these

CNTs are short and mainly concentrated around the catalyst islands and thus cannot be connected to devices.

We then increase the flows of C_2H_4 and H_2 to higher values, which is expected to give longer tubes. However, the CNTs grown in a flow of 30 sccm C_2H_4 + 900 H_2 are in a form of carpet (Fig. 3.11c). The CNTs grown are large in number, but they are curly and sticked together. It seems that the decomposition of C_2H_4 changes quite a lot in the small range of 15-30 sccm and therefore, the growth of well separated CNTs is difficult to achieve.

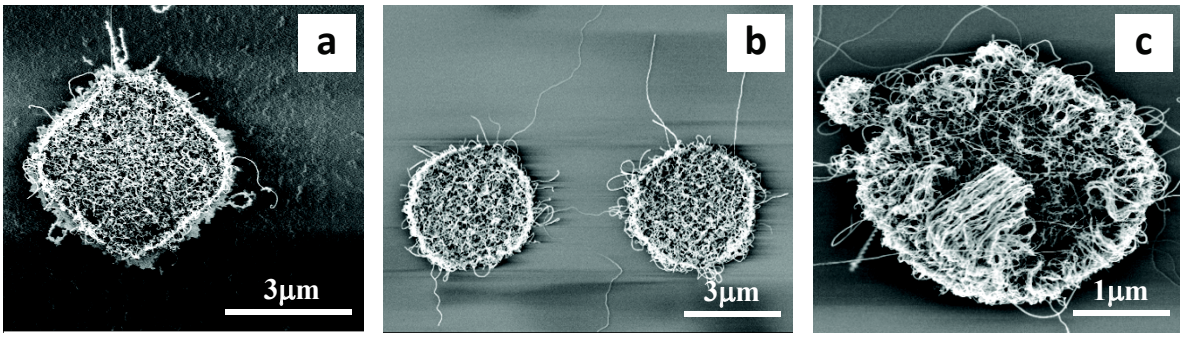

Figure 3.11. SEM images of CNTs grown by ethylene CVD at 750 °C. (a) 15 sccm C_2H_4 + 200 sccm H_2 forms amorphous carbon. (b) 15 sccm C_2H_4 + 600 sccm H_2 gives short and curly CNTs. (c) Higher gas flows of 30 sccm C_2H_4 + 900 sccm H_2 forms carpet of CNTs.

However, other studies have shown that water vapor can assist the growth of long CNT in ethylene CVD [22]. A hypothesis is that H_2O can clean the amorphous carbon covering the catalyst particles and hence increase their lifetime [23]. In our system, argon is injected through the water bubbler to carry the water vapor into the CVD reactor.

When a small amount of water is added to the process (by passing 40 sccm of Ar through the bubbler), the nanotubes are growing better. The best CVD condition we found is 30 C_2H_4 + 600 H_2 + 40 Ar through the water bubbler (Fig. 3.12a). The CNTs can grow out of the catalyst and have lengths of 3 – 7 μm. However, high resolution SEM and TEM images show that, there is still a large amount of amorphous carbon on the sample (Fig. 3.12b) and most of products are fibers and MWNTs which are defected and have large diameters (Fig. 3.12c). We also try with higher water concentrations but that leads to a very weak CNT growth. The cleaning effect of water seems to be so strong that it removes both the

amorphous carbon and the carbon atoms that are needed for the CNT growth. Apart from that, adding too much water to the process changes also the growth environment.

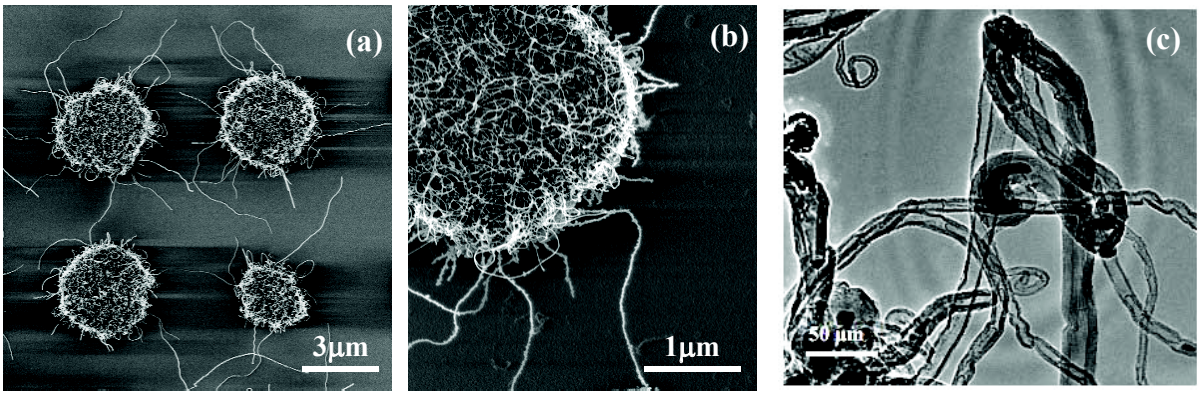

Figure 3.12. Water-assisted ethylene CNT growth with 30 sccm C_2H_4 + 900 sccm H_2 + 40 sccm of Ar through the water bubbler. (a, b) SEM, and (c) TEM images. Most of the growth products are MWNTs and carbon whiskers with high amount of defects and large diameters.

In conclusion, due to the high thermal self-decomposition rate of ethylene, it is difficult to control the CVD parameters accurately enough to produce high quality SWNTs. For this reason, we did not make any further studies using ethylene.

3.3.3. Ethanol CVD

Ethanol CVD is supposed to be a low temperature process of growing SWNTs [24–26]. This method utilizes argon as a carrier gas to introduce ethanol which acts as a carbon feedstock into the CVD chamber (Ar/bubbler). The bubbler is kept in an ice bath in such a way that the amount of ethanol carried by the unit volume of gas is controlled. OH radicals released from the decomposition of ethanol during the CVD process are believed to attack the carbon atoms with dangling bonds and in this way, amorphous carbon is efficiently removed from the catalyst particles in the early stages of the CNT growth. The absence of amorphous carbon accumulation can lead to a sustainable growth of SWNTs [24].

We try to optimize the growth conditions of our ethanol CVD process by varying the different gas flows. Catalyst Fe-Mo #3 is used as before which starts to grow CNTs at the

temperatures higher than 700 °C. During the gas flow optimization we keep the growth temperature at 800 °C and growth time in 10 minutes.

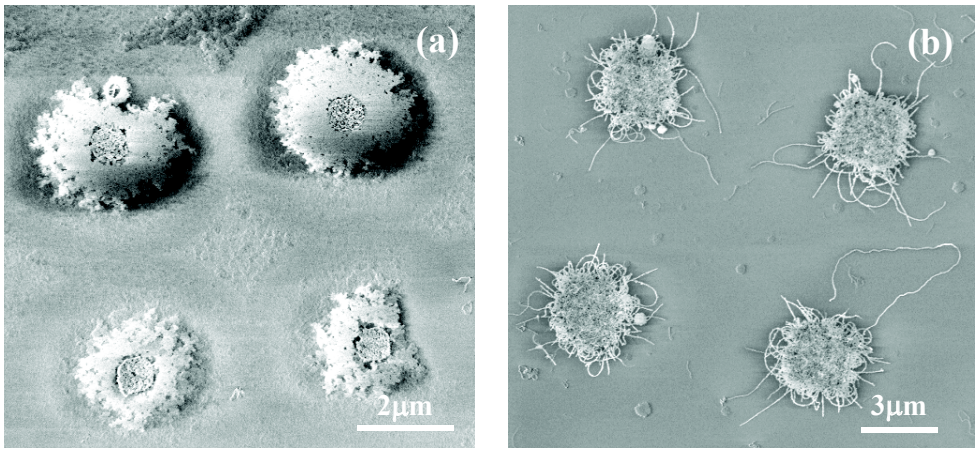

Figure 3.13. The samples grown by ethanol CVD process of (a) 1200 sccm, and (b) 700 sccm Ar through C_2H_5OH bubbler.

In the first tests, we use only ethanol vapor for the growth without any H_2 addition. The OH group released from decomposition of C_2H_5OH is expected to remove amorphous carbon. However, at high flows of ethanol (> 700 sccm Ar/bubbler), there is a large amount of amorphous carbon covering the catalyst and the CNT growth is limited (Fig. 3.13a, b). Then, we reduce the ethanol flow and add some H_2 and find out that, the CVD condition of 500 sccm Ar/bubbler + 500 sccm H_2 leads to an abundant growth of CNTs that are long and high in number (Fig. 3.14a). The TEM image shows that most of the tubes are SWNTs (Fig. 3.14b), but with larger diameter distribution (1 – 4.5 nm) than those grown with methane. A careful observation of the walls of the tubes shows that these tubes are less smooth and straight, which may indicate their lower crystallinity. Since the C-C and C-H bonds of ethanol are weaker than the C-H of CH_4 [6], the thermal decomposition of ethanol is higher than that of methane. The abundance of carbon radicals leads to an easier growth of CNTs with larger diameters, but also with lower quality.

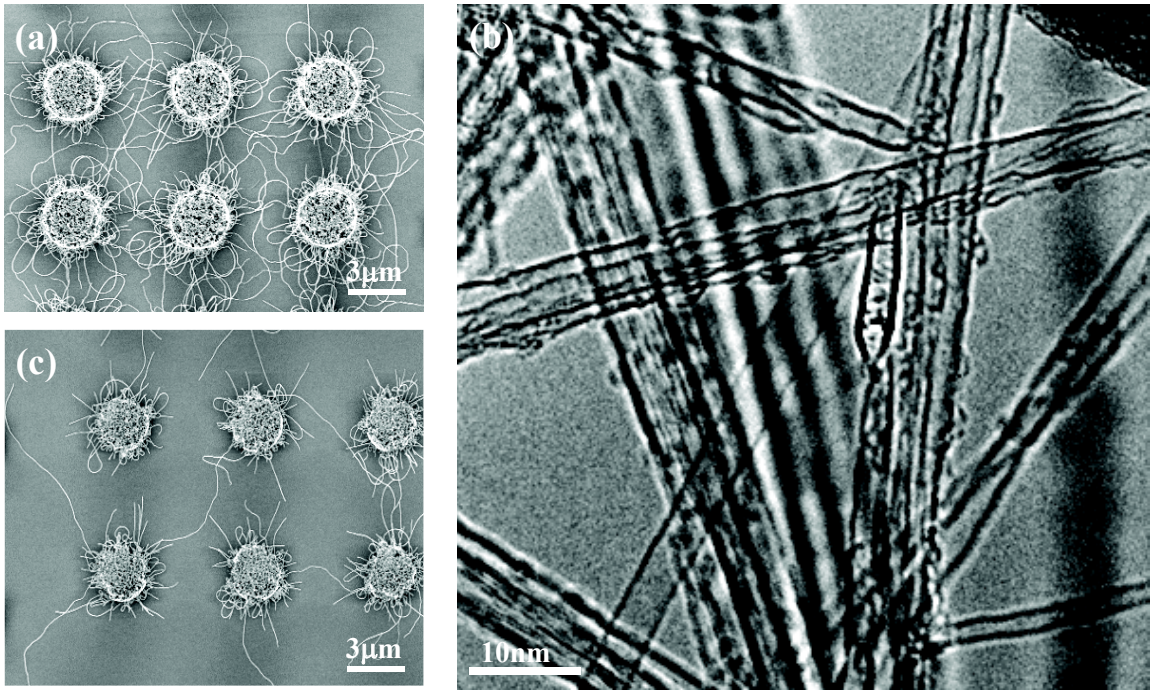

Figure 3.14. Samples after an ethanol CVD process with (a,b) 500 and (c) 50 sccm of Ar through liquid C_2H_5OH in the bubbler.

We continue to decrease the ethanol flow while keeping the 1:1 ethanol:H_2 ratio. It is surprising to observe that the nanotubes can grow in a large range of ethanol flow, from 500 sccm (Fig. 3.14a) to 50 sccm (Fig. 3.14c). Although the bubbler is thermally stabilized by ice-bath it seems quite difficult to control exactly the amount of C_2H_5OH in the process due to its liquid nature in the precursor. The ethanol CVD will be interesting to study in the future because it can lead to a high yield growth of long CNTs. However, the process parameters are more difficult to control.

Conclusions of section 3.3

In this section, we showed that it is possible to grow nanotubes with CH_4, C_2H_4 and C_2H_5OH CVD processes. The methane CVD was found to be the best process among them. The nanotubes grown with methane consist of mostly SWNTs with a high degree of crystallization. The CVD condition of 800 °C in 10 minutes using flow of 1200 sccm CH_4 + 700 sccm H_2 leads to a growth of long (3-15 μm) and straight SWNTs with moderate number density. The sample grown with this optimized condition is very clean from amorphous carbon. This CVD condition is used for the SWNT growth in the next section.

3.4. Optimization of the catalyst composition

Studies have showed that in the CVD synthesis of nanotube the chemical composition of the catalyst has very strong effects on the growth. At the beginning, single component catalysts like Fe, Co, Ni have been used for CVD, which gave relatively low yields and selectivities of the grown CNTs [5]. Later, it was found that combining common catalyst (Fe, Co) and one with non or low catalytic properties (Mo, Ru) can improve significantly the SWNT growth. Bimetallic catalysts like Fe:Mo [6], [27–29], Fe:Ru [6], [12], [13], [30], and Co:Mo [14], [31], [32] have been successfully used to grow SWNTs with a high yield, quality and selectivity. These enhancement effects on the growth have been explained in different ways, including the change on the catalyst particle size, hydrocarbon decomposition rate, and nanotube nucleation [3], [5], [6], [14], [18], [27], [33], [34]. Despite of the numerous studies of this subject, the roles of each catalyst component are still controversial issues. Answers are hard to find since the CNT growth occurs on very small particles at high temperatures and reaction rates.

In this section we study the effect of two Fe-based catalyst systems, namely Fe-Mo and Fe-Ru, on the growth of SWNTs. By investigating the binary phase diagrams of the addition metals (Mo or Ru) with Fe, we find out that at certain Mo or Ru concentration an alloy with Fe can form at the CVD temperatures. In these alloy regions, the two metals (Fe-Mo or Fe-Ru) form a homogeneous phase of solid solution with each other without a significant change of their lattices. We expect this can give a ‘doping’ effect, and the catalyst will lead to a significant improvement of SWNT growth. Moreover, the activity of these catalysts can be tuned by changing their chemical compositions.

3.4.1. Fe-Mo catalyst

The growth of SWNTs from Fe-Mo catalysts is well-known and the studies have showed that adding a small amount of Mo to Fe enhances significantly the catalytic activity [3], [6]. In the following, we explain our trials to optimize the catalyst by changing its compositions based on the phase diagram of the metals. Since the phase diagram of nanoparticles does not exist, we have used instead the phase diagram of bulk materials with some adjustments. We add an offset ΔT ~ 200 °C to the phase diagram because the nanoparticles have lower melting temperature than their bulk phase [33]. We assume the particles diameter varies from 1 to 10 nm. The different compositions of the Fe-Mo catalysts studied in this work are showed in Fig. 3.15 and table 3.2.

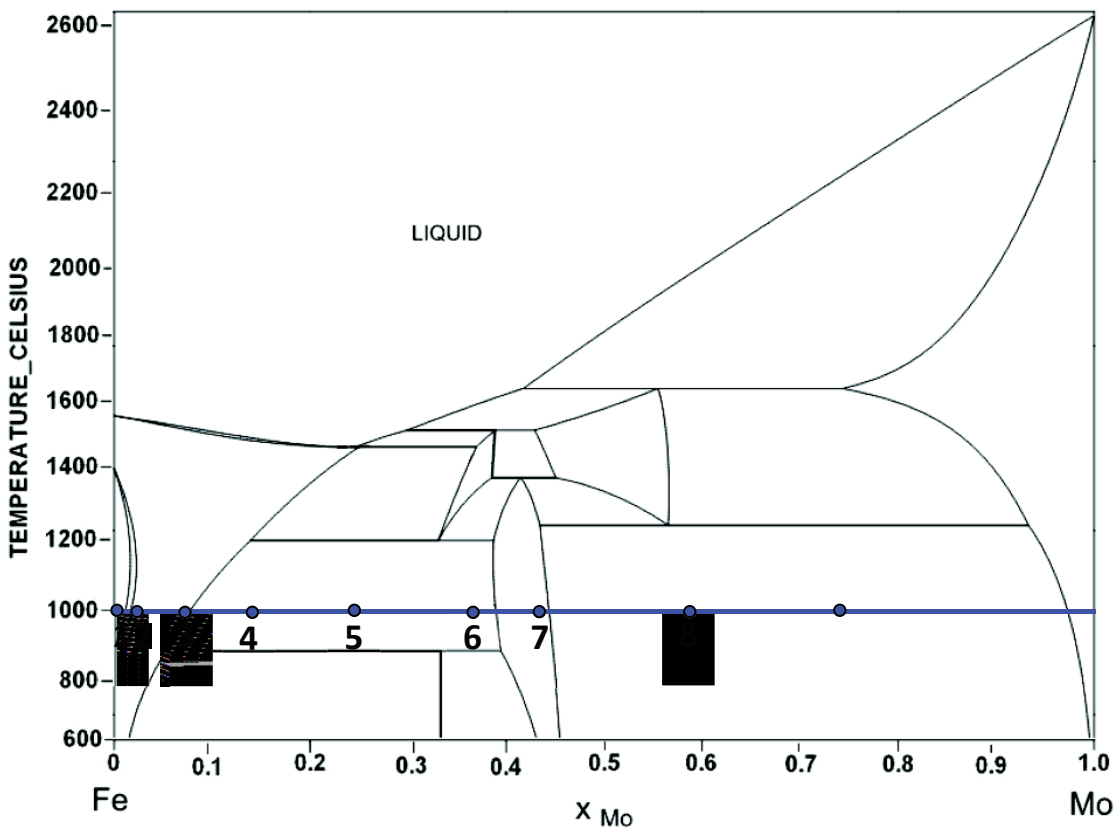

Figure 3.15. Different compositions of Fe-Mo catalysts used in this study [35] are marked with numbers. We consider the phase at about 1000 °C instead of the real CVD temperature of 800 °C of the CVD, since the nanoparticles have lower melting temperature than their bulk material.

Table 3.2. Fe-Mo catalysts with different concentrations of Molybdenum.

Catalyst name	Fe-Mo # 1	Fe-Mo # 2	Fe-Mo # 3	Fe-Mo # 4	Fe-Mo # 5	Fe-Mo # 6	Fe-Mo # 7	Fe-Mo # 8
Atomic ratio Mo:Fe (on Al_2O_3 support)	0	0.03	0.08	0.16	0.32	0.56	0.73	1.4

The catalysts (in table 3.2) are used for the CNT growth under the optimal methane CVD condition described in section 3.3. The first remark is that all these catalysts can lead to CNT growth. Figure 3.16 shows the SEM images of the CNTs grown from three representative catalysts Fe-Mo #1, #3, #8. In the case of catalyst #1 (only Fe), the CNTs have lengths of 2-5 μm and low number density (Fig. 3.16a). When ~ 8 at.% of Mo is added into the Fe catalyst, the CNTs grow clearly much better, which is manifested as high length (up to 15 μm) and number density of the tubes (Fig. 3.16b). However, when we increase the Mo concentration, the growth becomes weaker and the resulting CNTs are quite short and less dense (Fig. 3.16c), which is similar to the case of using pure Fe catalyst.

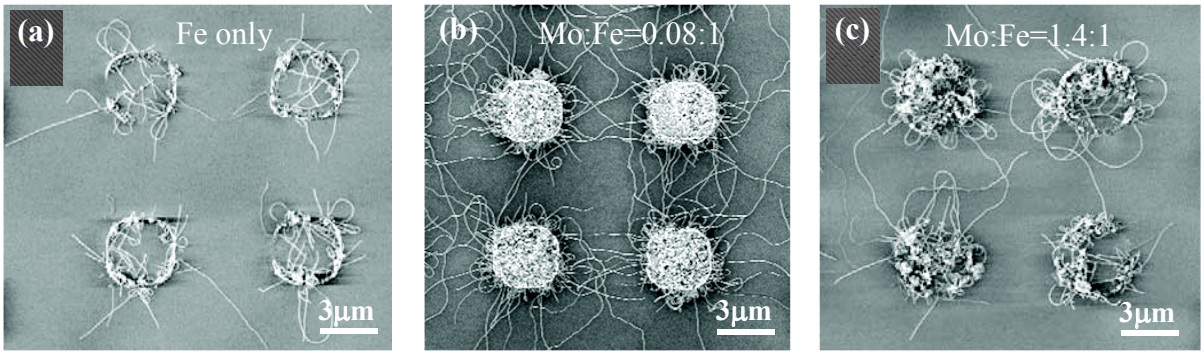

Fiure 3.16. SEM images of CNTs grown from Fe-Mo catalysts of different compositions. (a) Fe-Mo#1, (b) Fe-Mo #3, (c) Fe-Mo #8. The best growth is achieved with the catalyst Fe-Mo #3 (Mo:Fe=0.08:1).

It is clear that the ratio of Mo:Fe in the catalyst has a strong effect on the CNT growth. In addition to the SEM observation we use other methods like TEM and Raman spectroscopy to have a deeper view of the internal structure of the grown CNTs.

Figure 3.17 is the representative TEM images of the CNTs grown from the different catalyst compositions. In the samples with pure Fe (Fig. 3.17a) and high Mo concentrations

(Fig. 3.17d), DWNTs are quite often found together with SWNTs. Moreover, there is also a formation of carbon whiskers and large bamboo-like structures. The catalysts with high Mo concentrations also lead to growth of CNT bundles. On the contrary, the catalysts with a small amount of Mo produced mostly SWNTs (Fig. 3.17b,c). The catalyst with a ratio of Mo:Fe=0.08:1 is a special case, which grows almost purely SWNTs that were straight and well separated (Fig. 3.17b). From the TEM image (Fig. 3.17b), we can see that the SWNTs are well crystallized with very low defect content, and there is almost no amorphous carbon formation.

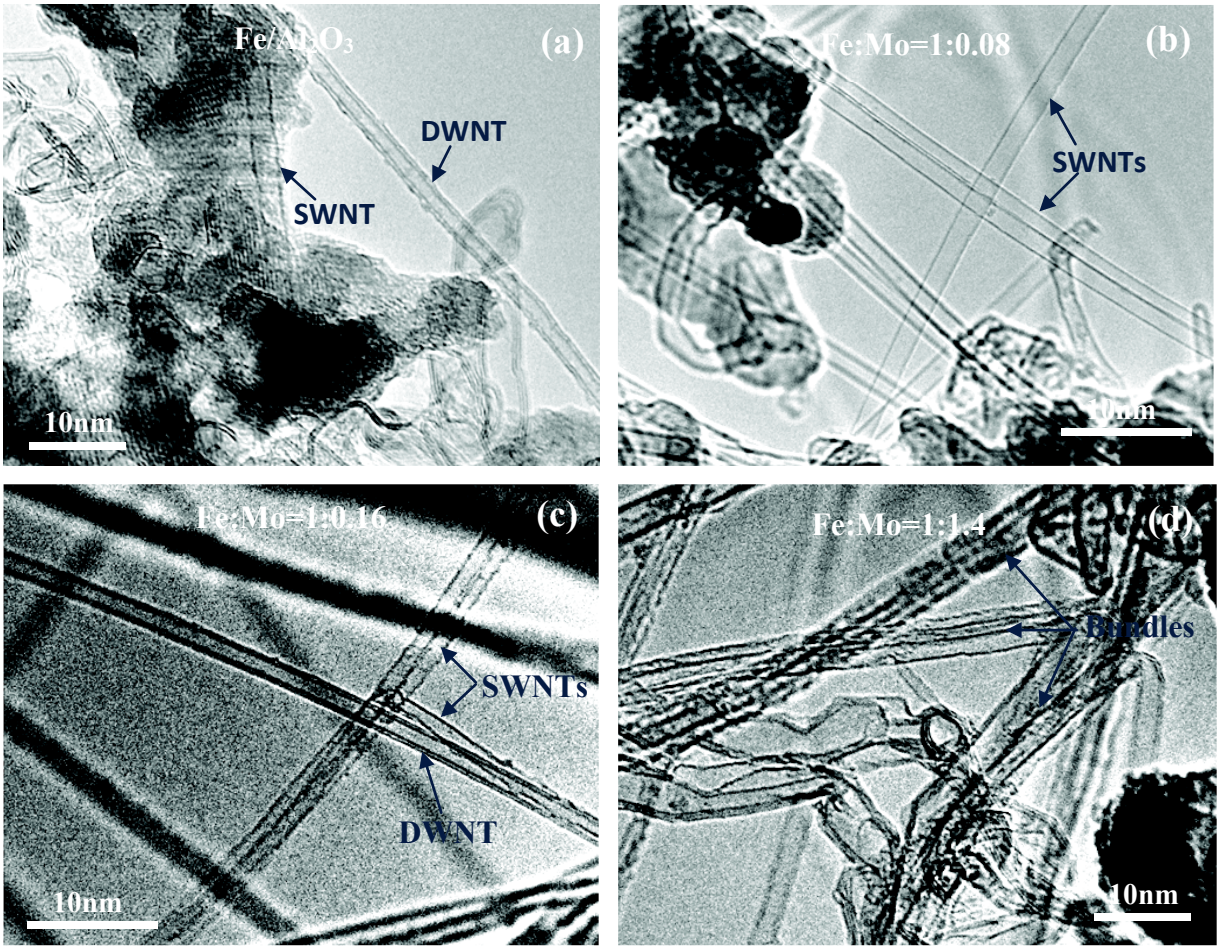

Figure 3.17. TEM images of nanotubes grown from the catalyst (a) #1, (b) #3, (c) #4, and (d) #8.

In addition, we made a statistics over 200 – 400 nanotubes for each of the catalyst composition to have a reliable conclusion. The ratio of SWNTs to MWNTs and the nanotubes diameter distributions measured from their TEM images are shown in Fig. 3.18.

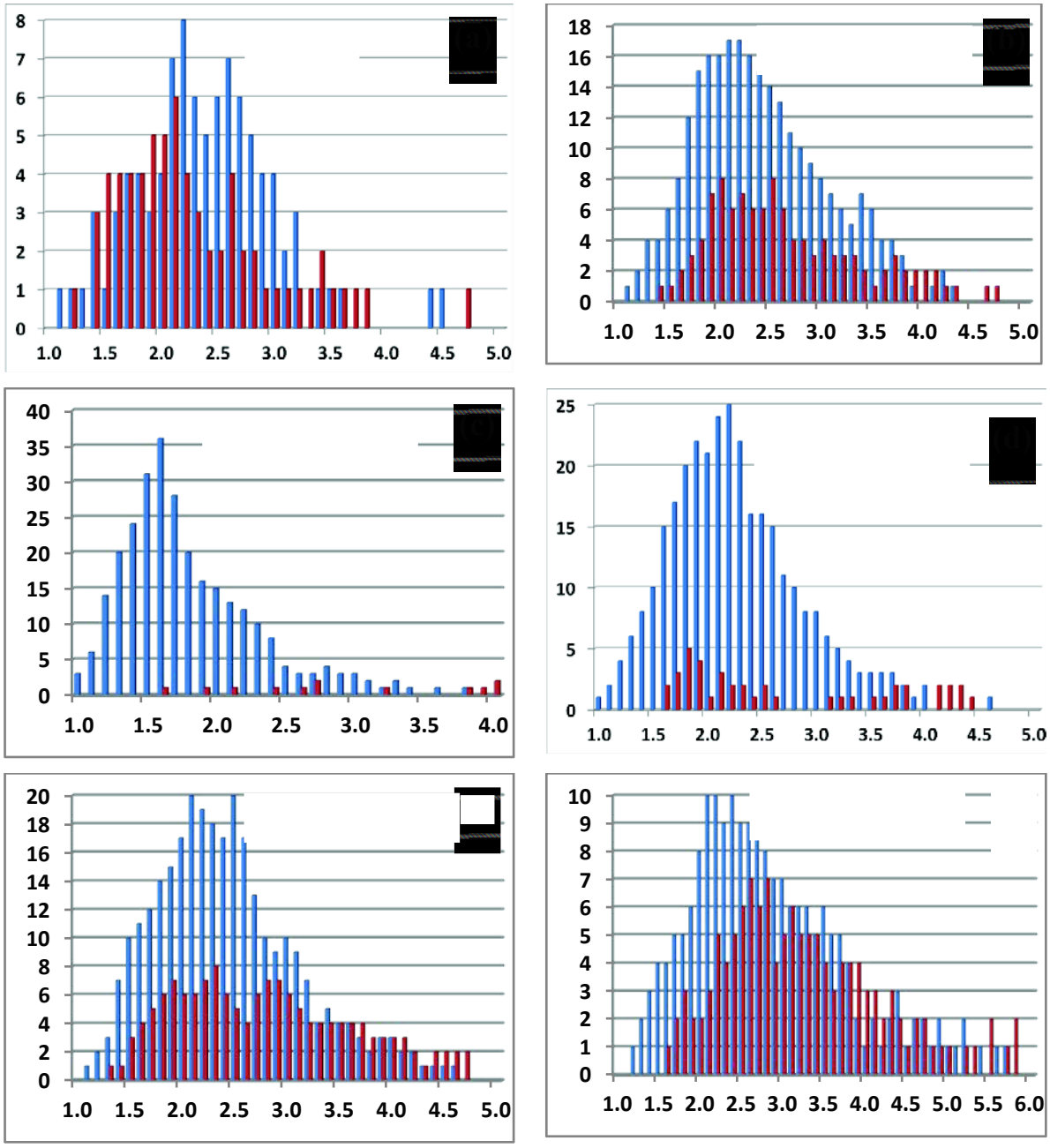

Figure 3.18. Diameter distribution of nanotubes grown from the catalyst (a) #1, (b) #2, (c) #3, (d) #4, (e) #5, and (f) #8. A very high ratio of SWNTs to DWNTs is obtained by using the catalyst Fe-Mo #3 with a molar ratio Fe:Mo = 1:0.08.

In the case of pure Fe catalyst the grown CNTs consist of 57% of SWNTs and 43% of DWNTs (Fig. 3.18a). In the statistics we have not taken into account the carbon whiskers and the large bamboo-like structures. The tubes diameter distribution varies in a range of 1 - 4.5 nm with a mean diameter of ~ 2.2 nm. When a small amount of Mo is added to the Fe-based catalyst (0 < Mo:Fe < 0.08) there was a significant improvement of the SWNTs/DWNTs ratio and CNT diameter distribution (Fig. 3.18b and c). The highest ratio of 96% SWNTs to 4% DWNTs is achieved with the **catalyst Fe-Mo #3** (Mo:Fe=0.08:1) as shown in Fig. 3.18c. The nanotubes have a narrow diameter distribution where 90% of them are in the range of 1 - 2.5 nm and the mean diameter is ~ 1.6 nm. This catalyst composition is also best for the growth of CNTs in sense of the tubes lengths and their number density (by SEM observations of Fig. 3.16). However, too high Mo concentration (Mo:Fe>>0.08) leads to a contrary effect (Fig. 3.18d to f). More and more DWNTs and MWNTs are formed with increasing Mo content, and the CNT diameters are shifted to larger values. The changes of the number of walls of the nanotubes grown with different Mo concentrations are shown in Fig. 3.19.

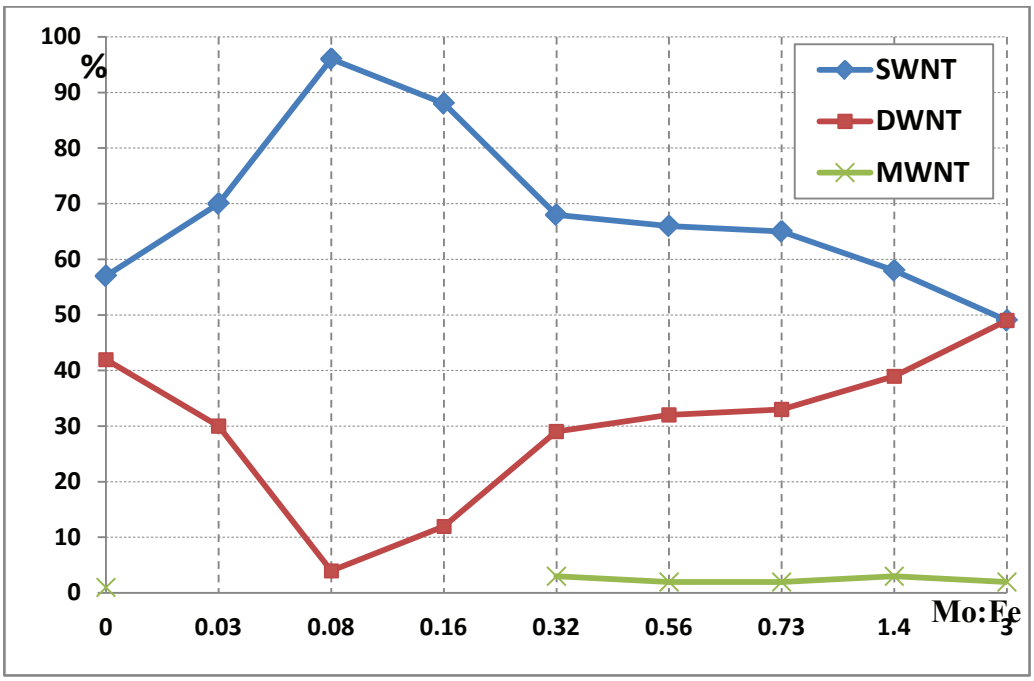

Figure 3.19. Percentage of different types of nanotubes (single wall, double wall, multi wall) in the samples grown from the catalysts with different Mo:Fe ratios.

The nanotubes are also characterized by resonance raman spectroscopy. Figure 3.20 shows a Raman map and the spectra of carbon nanotubes grown with the catalyst Fe-Mo #3. The spectra show a sharp G-band peak at 1588 cm^{-1} with a shoulder at around 1569 cm^{-1}, which is the signature of an isolated semiconducting SWNT [16]. The flat D-band at ~ 1330 cm^{-1} proves that the SWNT is defect-free and has a very low amount of amorphous carbon on it. The radial breathing mode (RBM) at 157 cm^{-1} indicates the nanotube is single wall and has diameter of 1.6 nm (d=248/ω [36]), that is in good agreement with the TEM statistic.

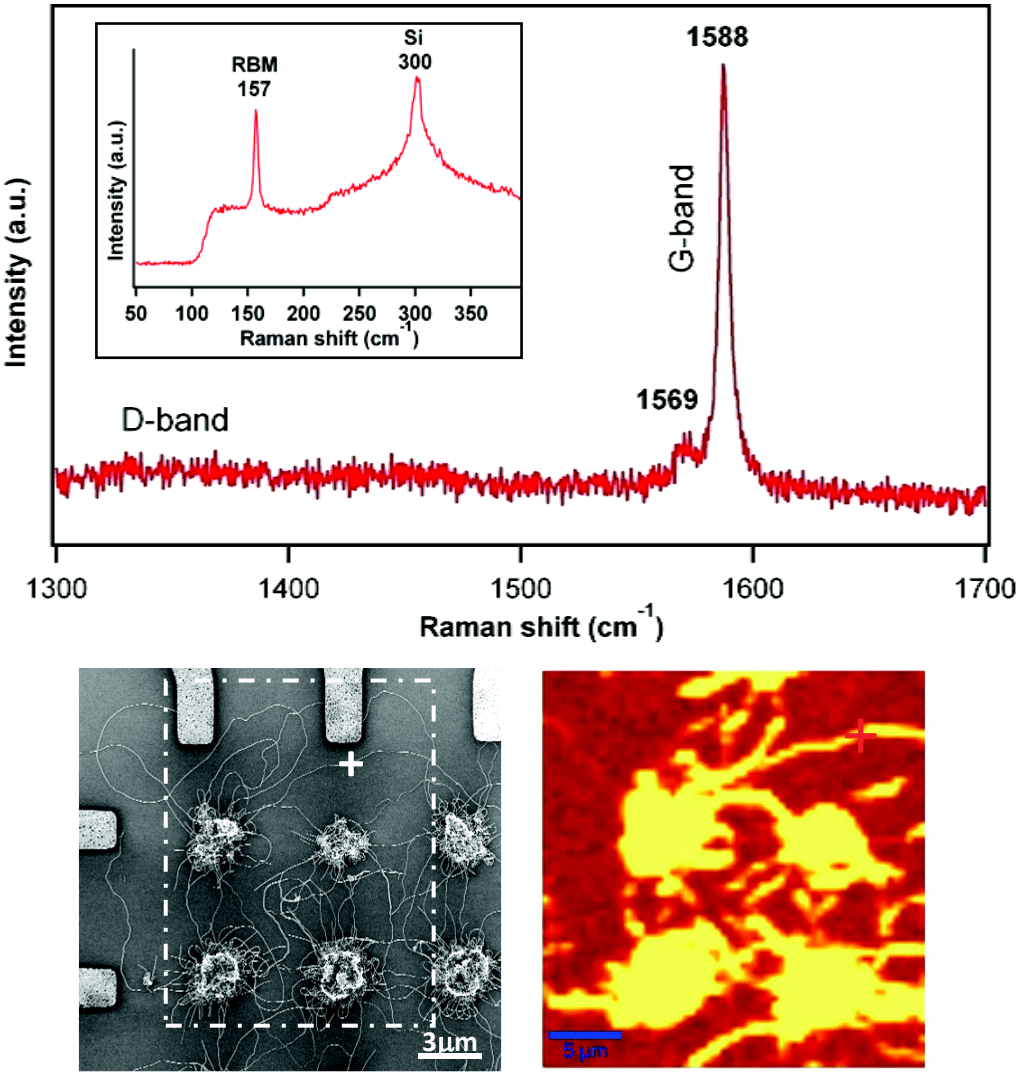

Figure 3.20. Raman map and spectra of SWNTs grown with the catalyst #3 by methane CVD. The RBM mode (inset) at 157 cm^{-1} corresponds to a SWNT of 1.6 nm diameter.

Moreover, we also check the CNT diameters by AFM imaging. Figure 3.21 shows a sample AFM image together with the profiles of the CNTs grown on a surface using the catalyst Fe-Mo #3. The nanotubes diameters are assumed to be the same than the heights of their AFM profiles, which are in a range of 1 - 2 nm in our sample. The sample surface is clean from amorphous carbon. Some particles are found on the surface that may have come from the damaging of metal electrodes at CVD high temperature. In addition to isolated CNTs, bundles of tubes are also found but their number is scarce.

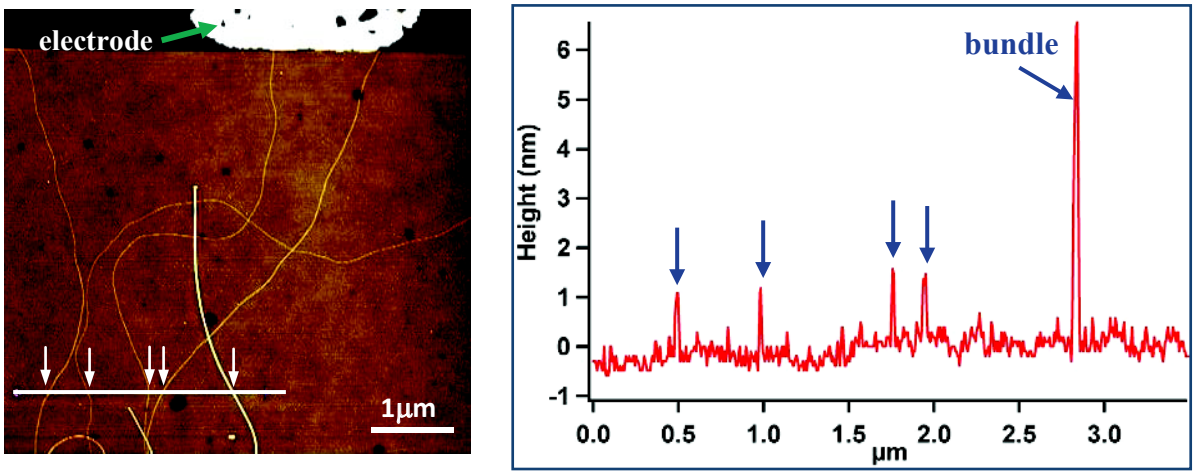

Figure 3.21 AFM image and profiles of nanotubes grown from the catalyst Fe-Mo #3.

In conclusion, we have found that the addition of Mo into Fe-based catalysts has strong effects on the nanotube growth. Small Mo:Fe ratio (~8 at.%) in the catalyst leads to a growth of mostly SWNTs with a narrow diameter distribution. The nanotubes are well separated, long and high in number density in comparison to those grown from single metal Fe catalyst. In contrast, high Mo concentrations (Mo:Fe>0.32) are not good for the SWNT growth, which prefer for the formation of more DWNTs and tubes in bundles. Since the role of Mo in bimetallic Fe-Mo catalyst is very interesting, we try to explain it in more detail as follow.

The role of Mo in Fe-Mo catalyst

There are several explanations of the role of Mo in Fe-Mo catalyst on the CNT growth, since many factors are influencing the growth of nanotubes. The explanations should take into account the size of the catalyst particles, the catalytic decomposition of hydrocarbon, the dissolving of carbon atoms into the catalyst, the wetting ability of nanoparticle droplets on supports (Al_2O_3, SiO_2…) for nucleation, the orbital electronic property of nanoparticles on the formation of graphene caps, etc [3], [18], [37–41]. Many efforts have been made on this issue, which could improve the understanding of CNT growth mechanism. Such investigations require a systematic and patient evaluation of different catalyst mix ratios of Mo:Fe. In principle, an *in situ* characterization of the catalyst particles during the CVD process is the most promising method. Several groups have tried this approach and managed to get some encouraging information [42–44]. However, it seems very difficult to realize the exact nanoparticle catalyzing CNT growth and to follow the growth process at the same time. The complexities include: the quick rate of the reactions, the variety of intermediate products, the high temperature, the small size of catalyst particle, the interaction of catalyst-support, which all contribute to the limitation of this approach. Alternatively, more efforts have focused to *ex-situ* characterizations of the catalyst before and after the different steps of CVD growth by using XRD, XPS, HRTEM, TGA, EDX, etc. As a result of these studies, many interesting information e.g. the phase of catalyst components, the evolution of particle size, the formation of carbide, and etc. has been found [27], [34], [45–47]. However, a clear and systematic explanation is still missing owning to the difficulties in characterizing small size particles, low concentration of metal component, interaction inside the catalyst system, as well as determining exactly the status of each growth process. In this work, we do not follow the above directions but instead utilize the phase diagrams to explain the effect of different Mo concentrations on the growth of nanotubes concerning the tube diameter distribution, number of walls, length and number density.

Mo is a transition metal which has a high ability to absorb and decompose hydrocarbons at CVD growth temperature [3], [21]. Mo has also a higher carbon solubility than Fe (see Fig. A1.1 of annex 1). However, the formation of multiple Mo carbides prevents this metal to become a good catalyst (see section 2.4.3). There are three carbide formations in the Mo-C phase diagram at ~ 32 at.%, 33.3 at.% (Mo_2C) and 50 at.% (MoC) at temperature

of 1000 °C. The CNT growth using a single metal Mo catalyst was reported only in carbon monoxide CVD at 1200 °C [40]. Although Mo alone is a poor catalyst, its combination with Fe have been widely used for the CNT growth [6].

In our work, the catalyst Fe-Mo #3 is the best for SWNTs growth. This catalyst composition is indicated in the binary phase diagram of Fig. 3.15. At the CVD temperatures Mo atoms can dissolve into the Fe lattice up to 8 atomic percent and form a Fe-Mo alloy. In this state, Fe and Mo form a solid solution with a unique phase. These Fe-Mo catalyst nanoparticles thus have higher carbon solubility than that of single metal Fe (25 at.%). This increase in solubility helps the catalyst particles to quickly go through the iron carbide formation (Fe_3C-see Fig. 2.9) and to reach the carbon super-saturation state. Therefore, the nanotube nucleation and formation happens easily, which reinforces the high yield and quality CNT growth.

On the contrary, higher Mo concentration than 8 at.% will form two separate phases of two compounds (see Fig. 3.15) [48]. Formations of these compounds not only consume the catalyst materials but also alter the chemical and electronic structure of the catalyst, which reduces its catalytic properties. In the CVD synthesis, the metallic state of the transition metals is supposed to be the active state for the CNTs growth [2], [19]. Moreover, the abundance of Mo, which cannot combine with Fe, will form multiple carbides nearby the Fe catalyst particles and prevent the CNT growth. The high Mo concentration catalysts thus have a low activity in the CNT growth.

In our experiments, the Fe-Mo catalyst composition affects strongly the selectivity of the SWNTs/MWNTs and the diameter distribution, which must be closely related to the size of catalyst nanoparticles. The catalyst prepared by the solution method has a wide range of nanoparticle diameters. However according to studies [18], there is only a certain range of particle sizes catalyzing the SWNT growth where the carbon supply rate (by catalytic decomposition) matches the CNT nucleation rate (Fig. 3.22). In a certain CVD growth condition, the very small particles are highly active in decomposing hydrocarbon rather than dissolving the C atoms which is mainly depended on their chemical composition. The excess carbon supply will form a continuous layer of amorphous carbon covering the nanoparticle surface, which prevents further carbon supply and hence stops the nanotube growth. The very

small particles needed for growing of small SWNTs are thus "poisoned". On the contrary, large nanoparticles cannot catalyze efficiently the decomposition of carbon stock and therefore, do not have enough carbon atoms for the CNTs nucleation. Only the nanoparticles with "moderate" size can ensure a suitable carbon supply and nucleation of the SWNTs. Moreover, MWNTs are believed either to grow from big catalyst particles or they are initiated from the thick graphitic layer covering the catalyst [2].

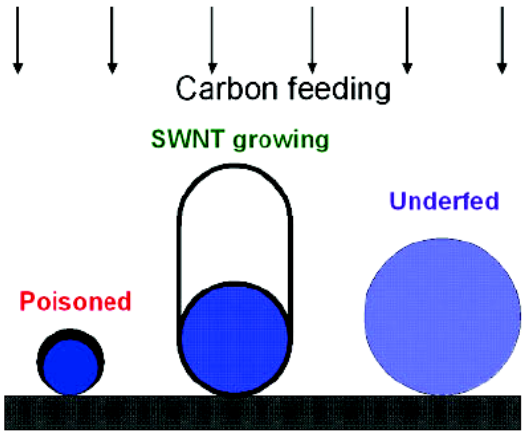

Figure 3.22. A scheme of the relation between the nanoparticle size and carbon feeding rate for the growth of SWNTs. Only catalyst with "suitable" size can growth SWNTs. Adapted from ref. [18].

Related to our Fe-Mo bimetallic catalyst, the alloy formation of 8 at.% Mo can significantly increase the carbon solubility of the nanoparticles. The new C atoms released on the particles surface are quickly diffused and dissolved into the catalyst, which is then followed by the nucleation and CNT formation. The small particles are hence staying active for the growth of small and single wall nanotubes. The absence of thick graphitic cover layer also eliminates the MWNTs formation as mentioned above. This stable "carbon supply-CNT nucleation" condition leads to a sustainable growth of long and well crystallized SWNTs.

On the contrary, catalyst compositions containing only Fe or Mo:Fe in high ratio do not match to the above mentioned condition, which leads to a growth favoring more DWNTs with lower yield and quality. Other by-products like carbon whiskers and bamboo-like structures are also formed (Fig. 3.17a, d).

In conclusion, the role of Mo in Fe-Mo catalyst is to increase the carbon solubility of the bimetallic catalyst. Since the first Mo carbide is formed at 32 at.% compared to 25 at.% of Fe, the addition of Mo (max 8 at.%) helps the catalyst (rich Fe) passing through the Fe_3C formation quickly to achieve the carbon super-saturation and CNT formation. Moreover, the diffusion rate of carbon into the catalyst particles is much higher, which prevents the formation of thick graphitic layer on the particle surface. In these conditions, the small catalyst particles stay active for the growth of small and single wall nanotubes. The optimal catalyst composition, Mo:Fe=0.08:1 of the catalyst Fe-Mo #3, can keep a proper proportion of hydrocarbon decomposition and CNT nucleation, which leads to a sustainable growth of long and well crystallized SWNTs.

3.4.2. Fe-Ru catalyst

It was shown in the last section of Fe-Mo catalyst that the carbon solubility of the nanoparticles plays an import role in the selective growth of SWNTs. Beside of adding high carbon solubility metal like Mo, some recent studies have shown interesting results of CNT synthesis by using low carbon solubility catalysts [6], [49]. The grown CNTs are very small in diameter and narrow distribution. We also try this direction in order to have a better understanding about the role of the bimetallic catalyst on the SWNT growth. Ruthenium (Ru) with very low carbon solubility is added to the Fe catalyst following the Fe-Ru phase diagram. Apart from that, the phase diagram of Ru with carbon does not show any carbide formation (Fig. A1.2 of annex 1).

The Fe-Ru catalysts are prepared in a solution with different compositions as shown in Fig. 3.23 and Table 3.3. The nanotubes are grown by methane CVD and characterized by the same techniques mentioned above.

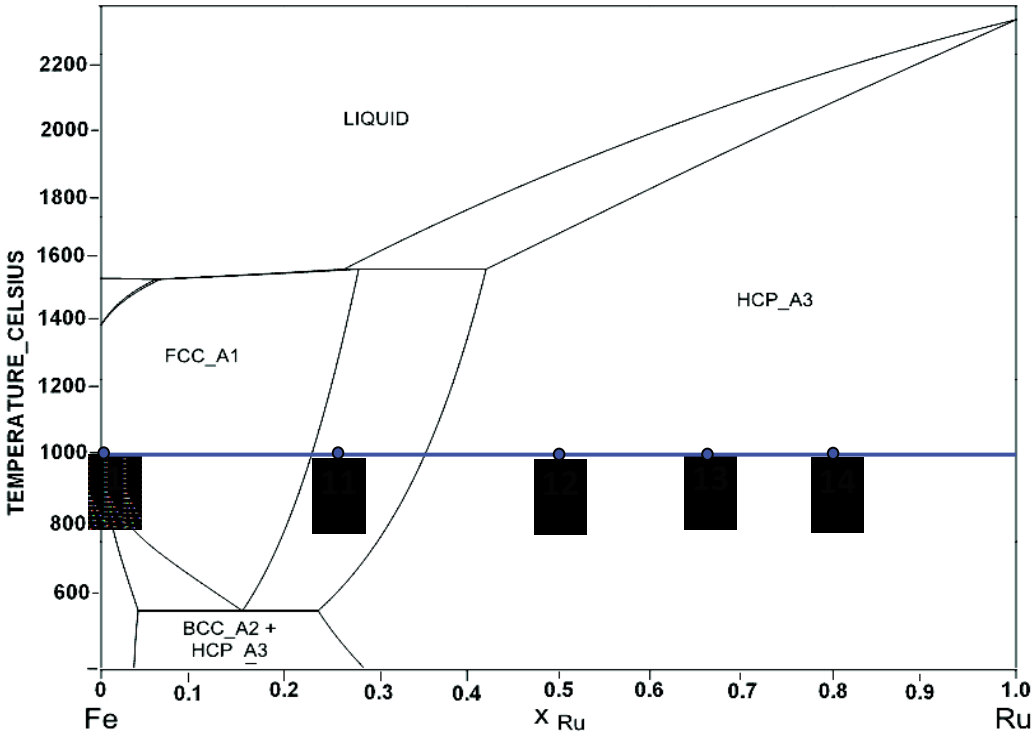

Figure 3.23. Fe-Ru catalysts with different molar ratios on their bulk binary phase diagram [50]. An offset of ΔT ~ 200 °C due to reduced melting temperature of the nanoparticles.

Table 3.3. Fe-Ru catalysts with different concentrations of Ru.

Catalyst name	Fe-Ru # 11	Fe-Ru # 12	Fe-Ru # 13	Fe-Ru # 14
Atomic ratio Ru:Fe (on Al_2O_3 support)	0.35:1	1:1	2:1	4:1

Figure 3.24 shows the SEM images of the CNTs grown from different catalyst compositions. First of all, the addition of Ru at the ratio Ru:Fe=0.35:1 (Cat #11, Fig.3.24b) leads to a weaker growth of CNTs than that of using only Fe (Fig. 3.24a). In general, this is logical since the low carbon solubility of Ru can reduce the catalytic activity of Fe-Ru catalyst. The TEM image in Fig. 3.25a also confirms the poor present of CNTs and the abundance of bamboo-like graphitic structures grown by this catalyst. However, it is surprising that the catalyst #12 with a higher Ru:Fe ratio (1:1, Fig. 3.24c) gives a better CNT growth. This contradiction can be explained when we look at the Fe-Ru phase diagram (Fig. 3.23). The composition of the catalyst #11 (~ 25 at.% of Ru) is in the region of Fe-Ru compound formation. These compounds do not favor the CNT growth as already discussed in the case of Fe-Mo.

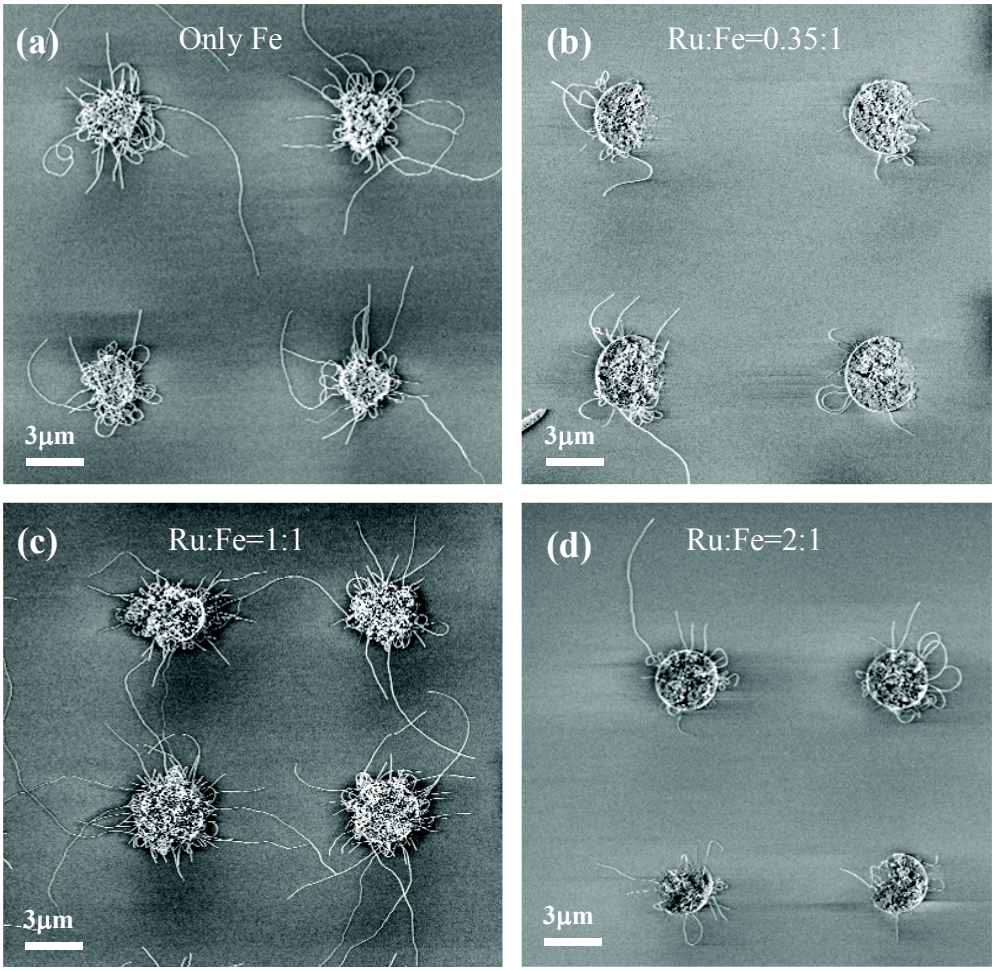

Figure 3.24. SEM images of CNTs grown from catalyst. (a) only Fe, (b) Fe-Ru #11, (c) #12, (d) #13.

On the contrary, the composition of the catalyst #12 is in the region of alloy formation. The Fe and Ru atoms can dissolve completely with each other without changing too much their chemical and electrical structures. Therefore, the CNT growth is enhanced due to a "doping" effect (will be explained below). The TEM image shows that most of the grown nanotubes are SWNTs with high crystallinity and with low amount of amorphous carbon (Fig. 3.25b). However, when we continued to increase the Ru concentration, e.g. the catalyst #13 with Ru:Fe=2:1, the catalytic activities are reduced significantly (Fig. 3.24d and 3.25c) due to the very low carbon solubility of Ru. One can recognize that the nanotubes grown with Fe-Ru catalyst are shorter and have lower number density than those grown with Fe-Mo catalyst.

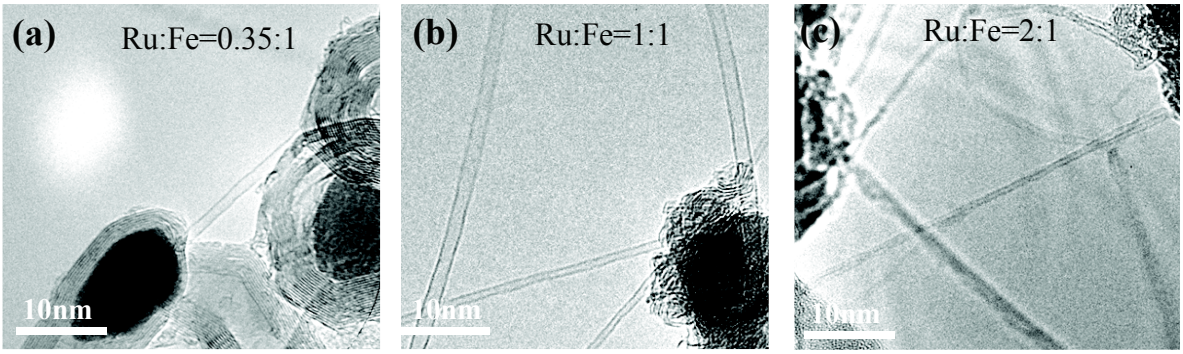

Figure 3.25. TEM images of CNTs grown from Fe-Ru catalyst (a) #11, (b) #12, and (c) #13.

We also make a statistics of the nanotube diameter distribution and SWNTs/MWNTs selectivity from the TEM images (Fig. 3.26). The nanotubes grown from Fe-Ru catalysts are smaller than those from Fe-Mo. The nanotube diameters are getting smaller and the ratio of SWNTs/DWNTs is higher with increasing the Ru:Fe ratio. CNTs grown from e.g. the catalyst #13 (Ru:Fe=2:1, Fig. 3.26d) have the diameter distribution in the range of 0.7 – 2.2 nm with the mean value of ~ 1.1 nm. Most of the nanotubes up to 94% are SWNTs.

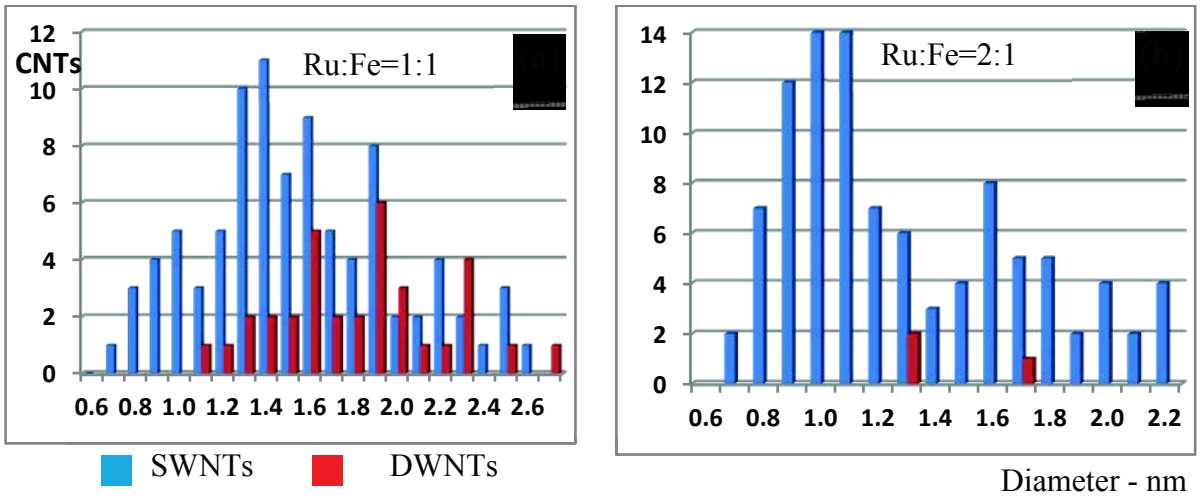

Figure. 3.26. Diameter distribution of CNTs grown from Fe-Ru catalyst (a) #12, and (b) #13.

We also characterize the nanotubes by resonance raman spectroscopy. Figure 3.27 shows Raman spectra of CNTs grown from the catalyst #13. The very narrow G-band peak at 1588 cm^{-1} together with the shoulder at around 1570 cm^{-1} is the signature of an individual semiconducting SWNT. Additionally, an RBM resonance mode has been observed at 259 cm^{-1}, which is characteristic for SWNT with a diameter of 0.9 nm [16]. The missing peak at defect band around 1330 cm^{-1} indicates that the CNTs have very high structural purity.

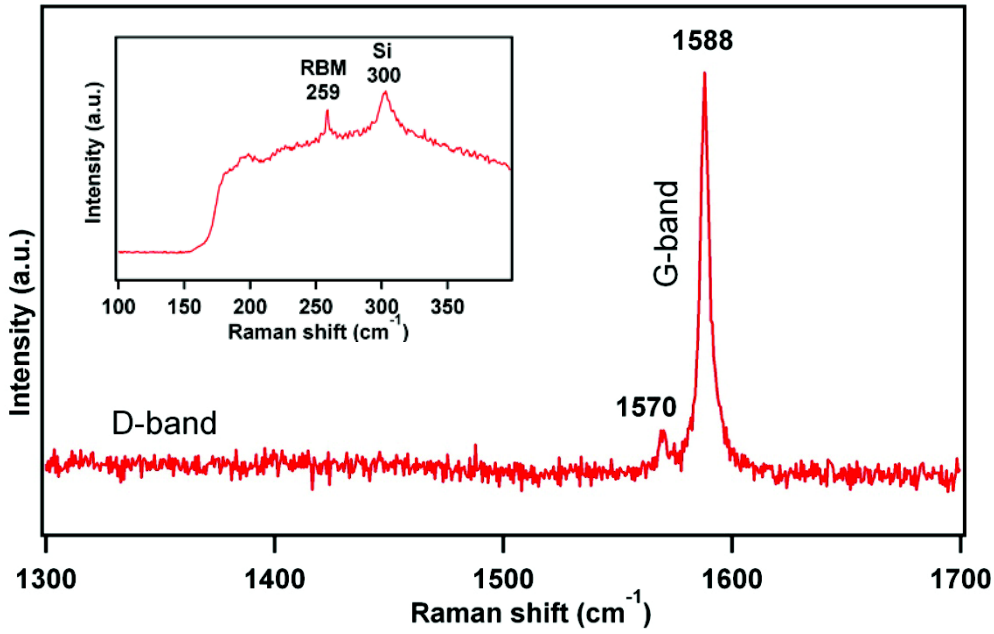

Figure 3.27. Raman spectra of nanotubes grown from the catalyst #13 (Ru:Fe=2:1)

AFM studies of the nanotubes diameter showed that most of the CNTs are as small as 1 nm, which is shown in Fig. 3.28.

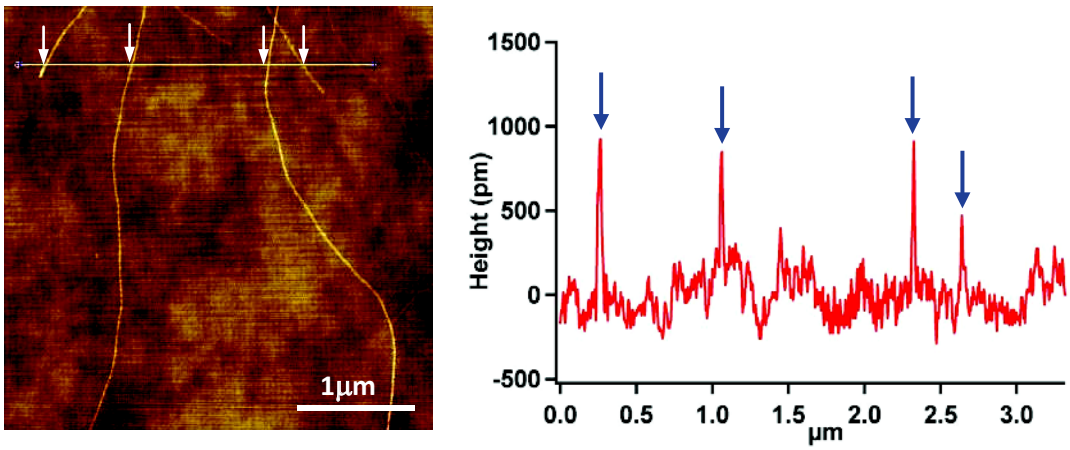

Figure 3.28. AFM image and profile of CNTs grown from the catalyst #13 (Ru:Fe=2:1). The arrows indicate the positions of the CNTs.

The role of Ru in Fe-Ru catalysts

The role of Ru in the catalyst should be contrary to Mo due to the very low carbon solubility of Ru. As mentioned in the previous section, small particles of pure Fe have a higher hydrocarbon decomposition activity than their ability to dissolve the released carbon atoms (due to the Fe_3C formation, see Fig. 2.9) and thus, the particles are covered by a thick layer of carbon and poisoned. In this case, the CNTs are growing from the larger particles for larger nanotube diameters or from the particles with a thick carbon cover resulting as MWNTs. However, when ruthenium is added to Fe, these metals can form a Fe-Ru alloy with a unique phase. At high Ru:Fe ratio (e.g. Ru:Fe=2:1 of catalyst #13) the Fe atoms are "diluted" into Ru lattice and the Fe-Ru catalyst particles have a lower hydrocarbon decomposition rate. All of the carbon atoms released at moderate rate now can diffuse into the catalyst for the CNT nucleation and formation [13]. Moreover, since the ruthenium main lattice does not form any carbide, the Ru-rich alloy then reduces the Fe_3C formation and keeps the small particles active for the growth. The medium and large catalyst particles now become "under fed" and the growth is shifted to small size particles with a narrow diameter distribution [18].

However, the Fe-Ru catalyst leads to the growth of CNTs with low number density and relatively short lengths. The growth is supposed to be terminated once there are not enough carbon atoms for the nucleation. With a very high Ru:Fe ratio of 4:1 (catalyst #14), the catalyst loses its activity and nearly no nanotubes can grow.

In conclusion, the Fe-Ru catalysts led to a growth of high quality SWNTs with very small diameters and narrow distribution. Ru dilutes Fe in its lattice, reduces the hydrocarbon decomposition rate, and increases the diffusion of carbon atoms into the catalyst particles for the CNT nucleation. A proper proportion of "carbon supply-CNT nucleation" can lead to a sustainable growth of high quality SWNTs. By tuning the catalyst composition, we were able to shift the CNT growth to smaller nanoparticles.

3.5. Conclusion

In this work, we have synthesized and characterized SWNTs. Different CVD protocols have been applied for the CNT growth and it was found that the methane CVD process is the best solution. We have optimized the CVD conditions such as gas flows and growth temperature for growing SWNTs of high quality.

The chemical composition of bimetallic catalysts (Fe-Mo and Fe-Ru) had a strong effect on the CNT growth concerning the selectivity of SWNTs/MWNTs, tube diameters, length and density, defect etc. We have combined the phase diagrams of the catalysts with the experimental results to find the optimal compositions, which can maintain a proper proportion between catalytic hydrocarbon decomposition and carbon solubility, in order to have a sustainable growth of SWNTs with narrow diameter distribution. Since the CNTs were elaborately characterized in this work, we could then apply the optimal synthesis condition to grow SWNTs on our devices and to have a high certainty about the tube quality. The applications of these SWNTs will be shown in the next chapters of device fabrication and electrical transport measurements.

References

[1] F. Triozon, S. Roche, A. Rubio, and D. Mayou, "Electrical transport in carbon nanotubes: Role of disorder and helical symmetries," *Physical Review B*, vol. 69, no. 12, Mar. 2004.

[2] M. Kumar and Y. Ando, "Chemical vapor deposition of carbon nanotubes: a review on growth mechanism and mass production," *J Nanosci Nanotechnol*, vol. 10, no. 6, pp. 3739–3758, Jun. 2010.

[3] H. J. Dai, "Growth and Characterization of Carbon Nanotubes," in *Topics in Applied Physics*, vol. 80, Springer Verlag, 2000.

[4] G. D. Nessim, A. J. Hart, J. S. Kim, D. Acquaviva, J. Oh, C. D. Morgan, M. Seita, J. S. Leib, and C. V. Thompson, "Tuning of Vertically-Aligned Carbon Nanotube Diameter and Areal Density through Catalyst Pre-Treatment," *Nano Lett.*, vol. 8, no. 11, pp. 3587–3593, 2008.

[5] E. Lamouroux, P. Serp, and P. Kalck, "Catalytic Routes Towards Single Wall Carbon Nanotubes," *Catalysis Reviews*, vol. 49, no. 3, pp. 341–405, 2007.

[6] A. M. Cassell, J. A. Raymakers, J. Kong, and H. Dai, "Large Scale CVD Synthesis of Single-Walled Carbon Nanotubes," *J. Phys. Chem. B*, vol. 103, no. 31, pp. 6484–6492, 1999.

[7] Y. Li, W. Kim, Y. Zhang, M. Rolandi, D. Wang, and H. Dai, "Growth of Single-Walled Carbon Nanotubes from Discrete Catalytic Nanoparticles of Various Sizes," *J. Phys. Chem. B*, vol. 105, no. 46, pp. 11424–11431, 2001.

[8] H. C. Choi, W. Kim, D. Wang, and H. Dai, "Delivery of Catalytic Metal Species onto Surfaces with Dendrimer Carriers for the Synthesis of Carbon Nanotubes with Narrow Diameter Distribution," *J. Phys. Chem. B*, vol. 106, no. 48, pp. 12361–12365, 2002.

[9] Y. Li, J. Liu, Y. Wang, and Z. L. Wang, "Preparation of Monodispersed Fe-Mo Nanoparticles as the Catalyst for CVD Synthesis of Carbon Nanotubes," *Chem. Mater.*, vol. 13, no. 3, pp. 1008–1014, 2001.

[10] H. S. Yang, L. Zhang, X. H. Dong, W. M. Zhu, J. Zhu, B. J. Nelson, and X. B. Zhang, "Precise control of the number of walls formed during carbon nanotube growth using chemical vapor deposition," *Nanotechnology*, vol. 23, no. 6, p. 065604, Feb. 2012.

[11] A. R. Harutyunyan, B. K. Pradhan, U. J. Kim, G. Chen, and P. C. Eklund, "CVD Synthesis of Single Wall Carbon Nanotubes under 'Soft' Conditions," *Nano Lett.*, vol. 2, no. 5, pp. 525–530, 2002.

[12] X. Li, X. Tu, S. Zaric, K. Welsher, W. S. Seo, W. Zhao, and H. Dai, "Selective Synthesis Combined with Chemical Separation of Single-Walled Carbon Nanotubes for Chirality Selection," *J. Am. Chem. Soc.*, vol. 129, no. 51, pp. 15770–15771, 2007.

[13] H. Wang, L. Sun, S. Wang, and Z. Xiao, "Influence of catalyst structures on carbon nanotubes growth via methane-CVD," *J Nanosci Nanotechnol*, vol. 9, no. 2, pp. 848–852, Feb. 2009.

[14] W. E. Alvarez, B. Kitiyanan, A. Borgna, and D. E. Resasco, "Synergism of Co and Mo in the catalytic production of single-wall carbon nanotubes by decomposition of CO," *Carbon*, vol. 39, no. 4, pp. 547–558, Apr. 2001.

[15] D. R. Lide, Ed., *Hand book of Chemistry and Physics 75th Edition*, 75th ed. CRC Press, 1994.

[16] M. S. Dresselhaus, G. Dresselhaus, R. Saito, and A. Jorio, "Raman spectroscopy of carbon nanotubes," *Physics Reports*, vol. 409, no. 2, pp. 47–99, Mar. 2005.

[17] O. Yu, L. Daoyong, C. Weiran, S. Shaohua, and C. Li, "A Temperature Window for the Synthesis of Single-Walled Carbon Nanotubes by Catalytic Chemical Vapor Deposition of CH4over Mo2-Fe10/MgO Catalyst," *Nanoscale Res Lett*, vol. 4, no. 6, pp. 574–577, Mar. 2009.

[18] Y. Li, R. Cui, L. Ding, Y. Liu, W. Zhou, Y. Zhang, Z. Jin, F. Peng, and J. Liu, "How Catalysts Affect the Growth of Single-Walled Carbon Nanotubes on Substrates," *Advanced Materials*, vol. 22, no. 13, pp. 1508–1515, Mar. 2010.

[19] C. T. Wirth, S. Hofmann, and J. Robertson, "State of the catalyst during carbon nanotube growth," *Diamond and Related Materials*, vol. 18, no. 5–8, pp. 940–945, May 2009.

[20] Y. Ando, X. Zhao, T. Sugai, and M. Kumar, "Growing carbon nanotubes," *Materials today*, vol. 7, p. 22, 2004.

[21] J. Furer, "Growth of Single-Wall Carbon Nanotubes by Chemical Vapor Deposition for Electrical Devices," Basel, 2006.

[22] G. D. Nessim, A. Al-Obeidi, H. Grisaru, E. S. Polsen, C. Ryan Oliver, T. Zimrin, A. John Hart, D. Aurbach, and C. V. Thompson, "Synthesis of tall carpets of vertically aligned carbon nanotubes by in situ generation of water vapor through preheating of added oxygen," *Carbon*, vol. 50, no. 11, pp. 4002–4009.

[23] K. Hata, D. N. Futaba, K. Mizuno, T. Namai, M. Yumura, and S. Iijima, "Water-Assisted Highly Efficient Synthesis of Impurity-Free Single-Walled Carbon Nanotubes," *Science*, vol. 306, no. 5700, pp. 1362–1364, Nov. 2004.

[24] R. Xiang, E. Einarsson, J. Okawa, T. Thurakitseree, Y. Murakami, J. Shiomi, Y. Ohno, and S. Maruyama, "Parametric study of alcohol catalytic chemical vapor deposition for controlled synthesis of vertically aligned single-walled carbon nanotubes," *Journal of nanoscience and nanotechnology*, vol. 10, no. 6, pp. 3901–3906, Jun. 2010.

[25] S. Maruyama, R. Kojima, Y. Miyauchi, S. Chiashi, and M. Kohno, "Low-temperature synthesis of high-purity single-walled carbon nanotubes from alcohol," *Chemical Physics Letters*, vol. 360, no. 3–4, pp. 229–234, Jul. 2002.

[26] A. Ansaldo, M. Haluška, J. Čech, J. C. Meyer, D. Ricci, F. Gatti, E. Di Zitti, S. Cincotti, and S. Roth, "A study of the effect of different catalysts for the efficient CVD growth of carbon nanotubes on silicon substrates," *Physica E: Low-dimensional Systems and Nanostructures*, vol. 37, no. 1–2, pp. 6–10, Mar. 2007.

[27] S. Curtarolo, N. Awasthi, W. Setyawan, A. Jiang, K. Bolton, T. Tokune, and A. R. Harutyunyan, "Influence of Mo on the Fe:Mo:C nanocatalyst thermodynamics for single-walled carbon nanotube growth," *Physical Review B*, vol. 78, no. 5, p. 054105, 2008.

[28] A. J. Hart, A. H. Slocum, and L. Royer, “Growth of conformal single-walled carbon nanotube films from Mo/Fe/Al2O3 deposited by electron beam evaporation,” *Carbon*, vol. 44, no. 2, pp. 348–359, Feb. 2006.

[29] L. Qingwen, Y. Hao, C. Yan, Z. Jin, and L. Zhongfan, “A scalable CVD synthesis of high-purity single-walled carbon nanotubes with porous MgO as support material,” *Journal of Materials Chemistry*, vol. 12, no. 4, pp. 1179–1183, Mar. 2002.

[30] X. Wang, W. Yue, M. He, M. Liu, J. Zhang, and Z. Liu, “Bimetallic Catalysts for the Efficient Growth of SWNTs on Surfaces,” *Chem. Mater.*, vol. 16, no. 5, pp. 799–805, 2004.

[31] V. M. Irurzun, Y. Tan, and D. E. Resasco, “Sol−Gel Synthesis and Char acterization of Co−Mo/Silica Catalysts for Single-Walled Carbon Nanotube Production,” *Chem. Mater.*, vol. 21, no. 11, pp. 2238–2246, 2009.

[32] D. E. Resasco, W. E. Alvarez, F. Pompeo, L. Balzano, J. E. Herrera, B. Kitiyanan, and A. Borgna, “A Scalable Process for Production of Single-walled Carbon Nanotubes (SWNTs) by Catalytic Disproportionation of CO on a Solid Catalyst,” *Journal of Nanoparticle Research*, vol. 4, no. 1, pp. 131–136, 2002.

[33] A. Moisala, A. G. Nasibulin, and E. I. Kauppinen, “The role of metal nanoparticles in the catalytic production of single-walled carbon nanotubes—a review,” *Journal of Physics: Condensed Matter*, vol. 15, no. 42, pp. S3011–S3035, Oct. 2003.

[34] X. Xu, S. Huang, Z. Yang, C. Zou, J. Jiang, and Z. Shang, “Controllable synthesis of carbon nanotubes by changing the Mo content in bimetallic Fe–Mo/MgO catalyst,” *Materials Chemistry and Physics*, vol. 127, no. 1–2, pp. 379–384, May 2011.

[35] MTDATA, “Phase Diagram Software from the National Physical Laboratory (Fe-Mo),” 2003. [Online]. Available: http://resource.npl.co.uk/mtdata/phdiagrams/femo.htm.

[36] R. Saito, C. Fantini, and J. Jiang, “Excitonic States and Resonance Raman Spectroscopy of Single-Wall Carbon Nanotubes,” in *Carbon Nanotubes*, vol. 111, Springer Berlin / Heidelberg, 2008, pp. 251–286.

[37] S. V. Rotkin and S. Subramoney, Eds., *Applied Physics of Carbon Nanotubes: Fundamentals of Theory, Optics and Transport Devices*, 1st ed. Springer, 1899.

[38] D. S. Bethune, C. H. Klang, M. S. de Vries, G. Gorman, R. Savoy, J. Vazquez, and R. Beyers, “Cobalt-catalysed growth of carbon nanotubes with single-atomic-layer walls,” *Nature*, vol. 363, no. 6430, pp. 605–607, Jun. 1993.

[39] P. Mauron, “Growth Mechanism and Structure of Carbon Nanotubes,” Freiburg, 2003.

[40] H. J. Dai, A. G. Rinzler, P. Nikolaev, A. Thess, D. T. Colbert, and R. E. Smalley, “Single-wall nanotubes produced by metal-catalyzed disproportionation of carbon monoxide,” *Chemical Physics Letters*, vol. 260, no. 3–4, pp. 471–475, Sep. 1996.

[41] P. Walker, J. Rakszawski, and G. Imperial, “Carbon Formation from Carbon Monoxide-Hydrogen Mixtures over Iron Catalysts.I. Properties of Carbon Formed,” *The Journal of Physical Chemistry*, vol. 63, no. 2, pp. 133–140, Feb. 1959.

[42] S. Hofmann, R. Sharma, C. Ducati, G. Du, C. Mattevi, C. Cepek, M. Cantoro, S. Pisana, A. Parvez, F. Cervantes-Sodi, A. C. Ferrari, R. Dunin-Borkowski, S. Lizzit, L. Petaccia, A. Goldoni, and J. Robertson, “In situ Observations of Catalyst Dynamics

during Surface-Bound Carbon Nanotube Nucleation," *Nano Lett.*, vol. 7, no. 3, pp. 602–608, 2007.

[43] E. Einarsson, "Growth dynamics of vertically aligned single-walled carbon nanotubes from in situ measurements," *Carbon*, vol. 46, no. 6, p. 923, May 2008.

[44] H. Yoshida, T. Shimizu, T. Uchiyama, H. Kohno, Y. Homma, and S. Takeda, "Atomic-Scale Analysis on the Role of Molybdenum in Iron-Catalyzed Carbon Nanotube Growth," *Nano Lett.*, vol. 9, no. 11, pp. 3810–3815, 2009.

[45] L. Durrer, J. Greenwald, T. Helbling, M. Muoth, R. Riek, and C. Hierold, "Narrowing SWNT diameter distribution using size-separated ferritin-based Fe catalysts," *Nanotechnology*, vol. 20, no. 35, p. 355601, Sep. 2009.

[46] A.-N. A. El-Hendawy, R. J. Andrews, and A. J. Alexander, "Impact of Mo and Ce on growth of single-walled carbon nanotubes by chemical vapour deposition using MgO-supported Fe catalysts," *Applied Surface Science*, vol. 255, no. 16, pp. 7446–7450, May 2009.

[47] V. V. Chesnokov, V. I. Zaikovskii, A. S. Chichkan, and R. A. Buyanov, "The role of molybdenum in Fe–Mo–Al2O3 catalyst for synthesis of multiwalled carbon nanotubes from butadiene-1,3," *Applied Catalysis A: General*, vol. 363, no. 1–2, pp. 86–92, Jul. 2009.

[48] "Introduction to Phase Diagrams." [Online]. Available: http://www1.asminternational.org/asmenterprise/apd/help/intro.aspx.

[49] Y. Qian, C. Wang, G. Ren, and B. Huang, "Surface growth of single-walled carbon nanotubes from ruthenium nanoparticles," *Applied Surface Science*, vol. 256, pp. 4038–4041, Apr. 2010.

[50] MTDATA, "Phase Diagram Software from the National Physical Laboratory (Fe-Ru)," 2005. [Online]. Available: http://resource.npl.co.uk/mtdata/phdiagrams/feru.htm.

Chapter 4. Nanofabrication and Measurement Setup

In this chapter, we demonstrate the nanofabrication of the "ultraclean" nanotube devices and the techniques used to perform the electrical transport experiments.

4.1. Motivation

During the past few years, several strategies [1–3] have been developed for making electrical contacts to carbon nanotubes (CNTs). Such devices typically consist of isolated CNTs connected to two metallic electrodes, one for the source electrode and the other one for the drain. A third electrode, the gate, is used to apply an electrostatic potential to the CNT. The device fabrication requires state of the art nanofabrication techniques and special care to obtain devices as "clean" as possible.

In the most popular fabrication procedure, CNTs are first deposited onto an isolating surface (often used as a back gate) with predefined markers. The deposition is done either by dispersing of bulk-grown CNTs separated into solution, or by *in situ* CVD growth on substrate (see chapter 3). Then, the CNTs are located with respect to the markers either by scanning electron beam microscopy (SEM) or atomic force microscopy (AFM). The metallic contacts are fabricated on top of the CNTs by aligned electron beam lithography (EBL) and a subsequent metal evaporation (Fig. 4.1a). This method has been successfully used for studying high transparent CNT junctions and interesting physical properties of metallic CNT quantum dots. However, the CNT junctions are inevitably contaminated chemically (solvents and resist residues...) and even structurally disturbed during sample preparation (sonication and purification of CNTs in solution, SEM observation, EB lithography…). The resulting chemical functionalization and induced defects in the CNT structure may have notable influences on its both transport and magnetic properties (backscattering centers, charge traps [4], paramagnetic defects [5] …).

In order to overcome most of the uncontrolled artifacts coming from the device processing and interaction with inhomogeneities of the substrate, efforts have been directed towards the study of "ultraclean" suspended CNT devices. The fabrication scheme is quite different from the previous one. It starts with the fabrication of predefined source and drain electrodes. CNT are then grown *in situ* by the CVD technique (chapter 3) from patterned

catalyst islands, which are deposited on top of the electrodes (Fig. 4.1b). The resulting CNT junctions lie freely suspended on top of the source and drain electrodes without any contact with the device substrate. In this scheme there is no need for any post-treatment steps after the CNT growth because the CNTs are directly grown on the chip at the very last step of the fabrication.

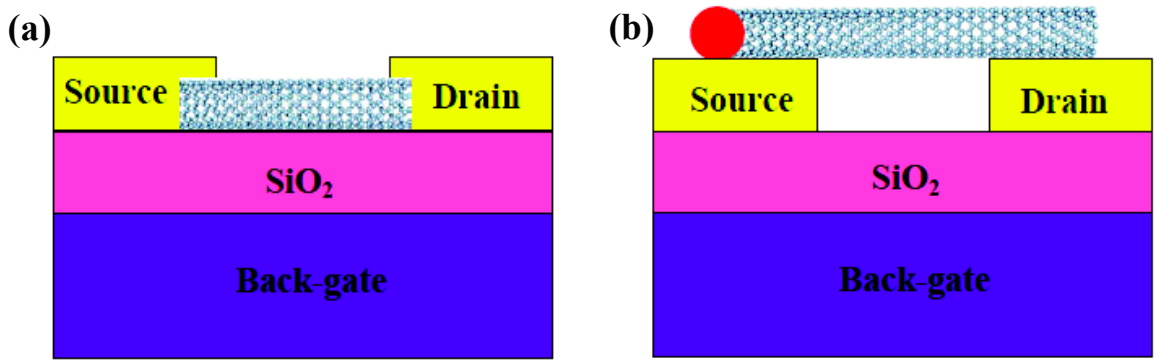

Figure 4.1. Schematics of two different types of CNT device. (a) Conventional device: metallic electrodes contact on top of the nanotube pinned on the surface. (b) Ultraclean device: the suspended CNT contact on top of the source and drain electrodes.

Such ultraclean CNT devices have attracted considerable attention during the last few years. They enabled, e.g., to deepen the understanding of the electronic properties of semiconducting CNTs (mostly small band gap) in the few charge carrier regime [6], where only one electron (or hole) can be controllably trapped in the CNT. Remarkably, the nanotube electronic structure has been resolved with unprecedented resolution and clarity. This enables the observation of intriguing physical phenomena, such as the spin-orbit coupling arising from the CNT cylindrical geometry [7]. This result came as a surprise to most of researchers, since it was in contradiction with a large number of earlier experiments, in which interactions coming from the electronic disorder and multiple electrons in the dot have masked this effect. The observation has recently motivated many theoretical studies to understand this effect and new concepts have been proposed to manipulate electron spin states in CNT-based devices. Moreover, since the CNTs are suspended, they also enable to study the mechanical degree of freedom in CNT-based nanoelectromechanical (NEMS) resonators. Due to the low mass of CNT combined with very high Q factors (~ 10^5), a strong coupling between mechanical and electronic properties of CNTs have been demonstrated [8]. This effect is interesting both from fundamental point of view as well as for applications (sensitive force detectors…).

The advantages of using ultraclean CNTs to study the electronics properties of nanotubes were our prime interest in this work. A special care has been taken to optimize and overcome the intrinsic difficulties of this strategy of fabrication. The fabrication procedure is first presented in section 4.2. After the different fabrication steps, the as-prepared samples are selected according their transport characteristics at room temperature (section 4.3) and then mounted in a dilution refrigerator equipped with a home-made 3D magnetic coil system. The setup used for the measurements at very low temperatures is described in section 4.4.

4.2. Fabrication of ultraclean suspended CNT devices

The device fabrication includes several main steps which are schematically depicted in Fig. 4.2. All these steps are crucial to obtain a working device at the end. The fabrication starts with creating alignment marks on a Si^{++}/SiO_2 wafer. Source and drain electrodes are fabricated by EBL followed by metallization and lift-off. The catalyst is then deposited on top of the electrodes at predefined positions. At the end of the process, the chips are placed in the CVD furnace for the CNT growth.

4.2.1. Fabrication of the electrodes

As mentioned before, the CNTs grow directly in random orientations on top of the predefined electrodes without any preferential alignment. The probability to get a single isolated carbon nanotube lying in between the contacts is thus rather low (even if it can be optimized), which results in a very low success probability to get a working device. Therefore, it is necessary to fabricate many structures, each of which requires several lithography steps with accurate alignments and high enough resolutions.

We tried several strategies of fabrication. At the beginning of this thesis, we developed a fabrication procedure based only on the optical lithography (using the MJB3 DUV system of Nanofab). This approach has the advantage to fabricate structures quickly and easily on a whole 2 inches wafer (all the structures are exposed simultaneously through a quartz mask). By the time, we developed the same kind of fabrication procedure by using a state of the art electron beam lithography system (JEOL 6300FS at PTA), enabling more

accurate alignment, higher resolution and more flexibility to change the device design. Besides, this electron beam system operates at a high acceleration voltage (100 kV), which reduces the proximity effects arising in the fabrication of the two electrodes (5-10 μm wide) separated by only 100 nm - 500 nm. We also highlight that the optimization of all the parameters (choice of the resists, system operating conditions, sample design…) took us a lot of efforts and time and cannot be completely described here in details. In the following, we only describe the main conditions of the device fabrication using an all electron beam strategy.

The electrode fabrication steps are represented in Fig. 4.2 (a, b) and the final chip design in Fig. 4.3. The design typically consists of 14 pairs of electrodes connected to larger metallic pads, which are later used to connect the devices on the electrical measurement setup. All the gaps are connected to a common ground electrode in order to increase the number of possible junctions.

The substrate used for the device fabrication is a Si wafer of 2 or alternatively 4 inches in diameter, which is degenerately doped (n-doped in our case) and covered by a 300-800 nm thick SiO_2 layer. The Si^{++} is used as a back gate for the devices while the oxide layer isolates the junctions from the conducting back gate. First, alignment marks are patterned on the wafer surface by EBL, followed by a metal deposition of Pt/Cr (50 nm/10 nm) and a lift-off (Cr is used as a sticking layer). Two main types of markers are fabricated: the global marks (for the whole wafer shift and rotation corrections) and the chip marks (for alignment and beam focus corrections of each set of electrodes). In a second step, the contact pads and electrode connections are fabricated. This step can be done either by aligned optical lithography or EBL. At the end of the thesis, this step was carried out by EBL with very high beam currents (~ 20-30 nA). In order to significantly reduce the insolation time of the electron beam, we used an UV5 photoresist (normally used for optical lithography). Indeed, this resist needs a very low electronic dose of typically 30 $\mu C/cm^2$ (in comparison, a dose of 1000-1500 $\mu C/cm^2$ is required for PMMA). This results in a large gain of insolation time while keeping a good enough resolution. The UV5 resist is spin coated at a speed of 4000 rpm for 60 seconds (~ 500 nm thickness) and baked at 130 °C for 60 seconds. The insolated resist is then baked again at 130 °C and developed in the LCD26 developer for about 30 seconds. The metal deposition step is made in an electron beam evaporator at the PTA and

consists of a 10 nm of Cr followed by a 50 nm of Pt. The lift-off of Pt/Cr is carried out in acetone for few minutes with a support of low power sonication. Residues of resist and deposited metal are then rinsed away in isopropanol (IPA) and the sample is dried by nitrogen blow. The third step consists in the fabrication of the aligned metallic electrodes on which the CNTs are being connected. This step needs a better resolution than the previous ones. The ZEP520A electron beam resist is spin coated at 4000 rpm speed for 60 seconds (~ 350 nm thickness) and then baked at 180 °C for 60 seconds. The subsequent e-beam insolation uses a current of 1 nA and a dose of 550 μC/cm^2. At these conditions, a slight over-exposure is obtained resulting in an undercut profile for the metal lift-off. The development of the resist includes 3 steps: 60 seconds in MIBK:IPA (1:1), then 20 seconds in MIBK:IPA (1:89), and rinsing in IPA. The metal evaporation consists again in 10 nm of Cr and 50 nm of Pt. The lift-off is done in the AR-300 remover.

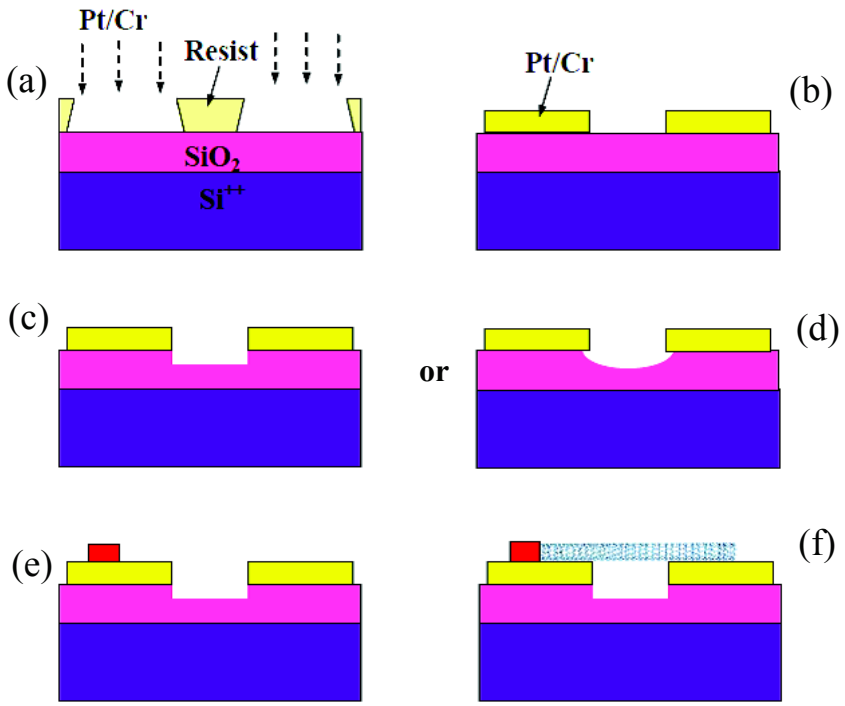

Figure 4.2. Main steps of the device fabrication. (a, b) Fabrication of predefined metallic gaps, including standard EBL (a), followed by the evaporation of Pt/Cr and lift-off to obtain the structure depicted in (b). The underlying SiO_2 surface is then partially etched away by dry etching (c) or anisotropic wet etching (d). Catalyst islands are localized on top of the electrodes (e) followed by the *in situ* CVD growth (f).

The substrate after the electrode fabrication (Fig. 4.2 a, b) is cleaned in an oxygen plasma for a few minutes to remove the organic residues resulting from the lithography. Thereafter, the SiO_2 is partly etched (~ 100 nm) by using either a dry reactive ion etching (CHF_3 feedstock gas) (Fig. 4.2c) or a wet etching buffered HF (Fig. 4.2d). This step ensures that the CNTs are effectively suspended between the source and the drain electrodes after the growth step. Layout of a chip after the fabrication of electrodes is shown in Fig. 4.3.

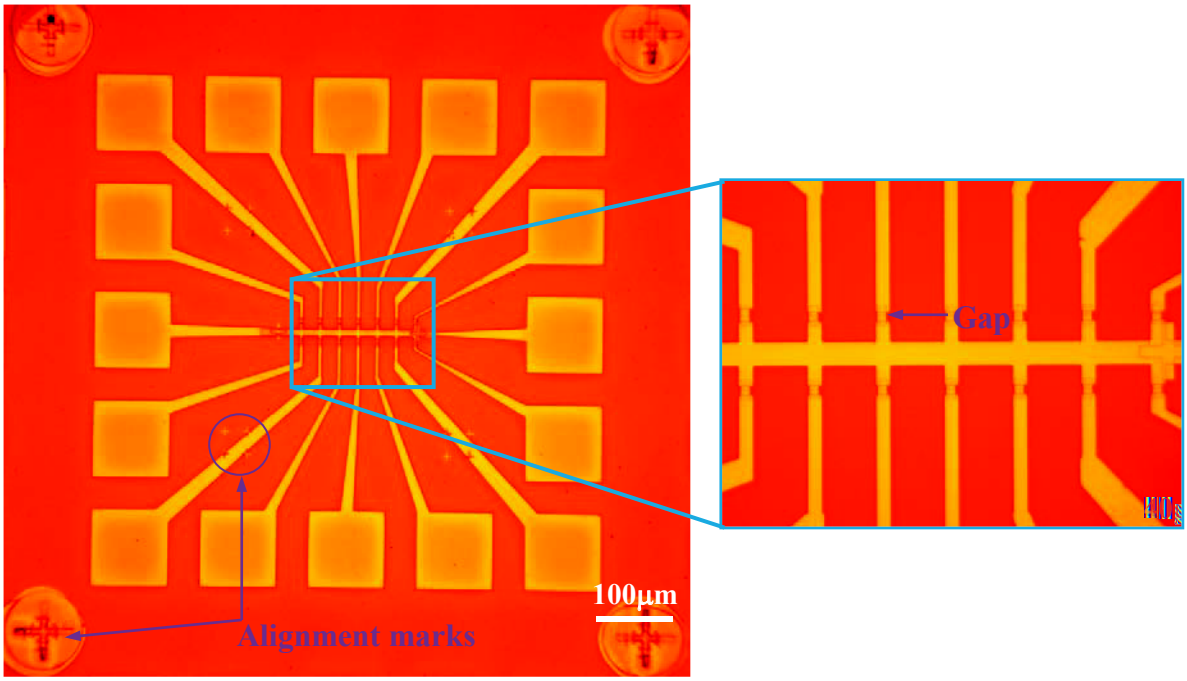

Figure 4.3. The chip after fabrication of the electrodes. (left) Layout of a chip. There are 14 pairs of electrodes connected to large bonding pads. A common ground electrode (horizontal straight pattern in the middle) is used in order to increase the number of possible junctions. (right) Zoom of the working area containing 14 gaps.

4.2.2. In situ CVD growth of the suspended CNTs

Following the preparation of the device substrate and the metallic electrodes (Fig. 4.2a-d), the last step consists in the localized growth of the CNTs (Fig. 4.2e, f). An aligned EBL step creates openings in a resist (here LOR 7A), which are used as a mask for the catalyst deposition (Fig. 4.4a). These openings are located in close proximity of the electrode edges.

The catalyst solution (Fe-Mo #3, see Chapter 3) is spin coated on the sample at a speed of 3000 rpm in 30 seconds, followed by a baking step at 100 °C in 1 minute. After lifting off the resist by PG remover, only catalyst islands remain on pre-defined positions (Fig. 4.2e). A subsequent oxygen plasma step is essential to remove all organic residues on the catalyst particles, which may reduce the catalytic activity, as well as to clean the electrode surface for an improved CNT-metal contact.

The *in situ* growth of CNTs is done by CH_4 CVD at 800 °C in 10 minutes, with gas flows of 1200 sccm CH_4 and 800 sccm H_2 (already described in Chapter 3). One can notice that the CNTs in this *in situ* growth method grow randomly from the catalyst islands and just few of them have good contacts with the metallic electrodes. We managed to achieve a high probability of one CNT over one gap by changing various parameters of the device fabrication, such as the size of the catalyst islands, the distance from the catalyst to the gap, the density of the deposited catalyst, the duration and the temperature of the CVD growth. To select the good CNT junctions, we do not use any SEM observation in order to keep the as-grown CNT as clean as possible. Probing the I-V characteristic of junctions is realized instead (see Section 4.3). For these reasons, many structures have been used for the CNT growth. A SEM image of a typical suspended CNT device is shown in Fig. 4.4b.

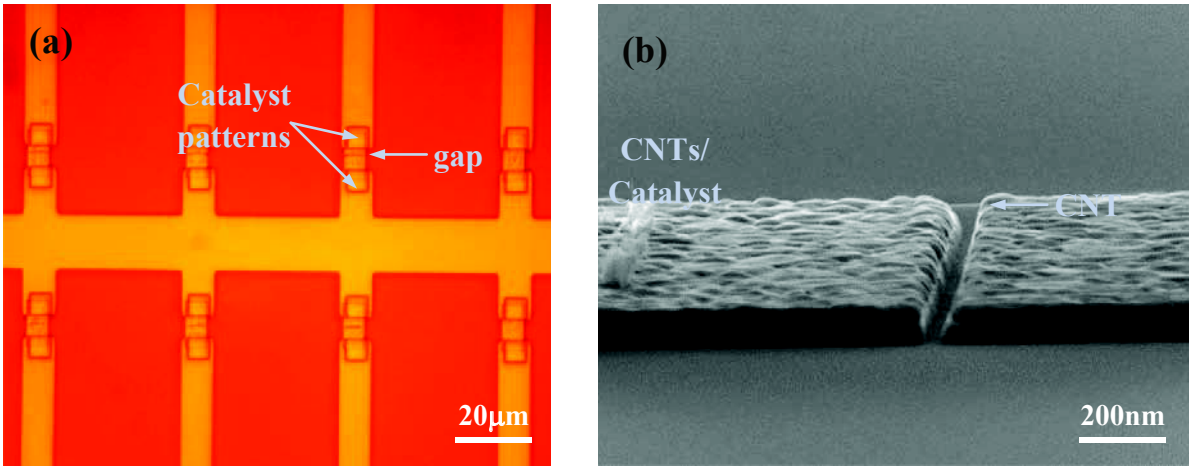

Figure 4.4. In situ growth of the suspended CNTs. (a) Preparation of the substrate for the patterning of the catalyst islands on top of the contact electrodes. (b) SEM image of a final suspended CNT device after the CVD growth.

4.2.3. Fabrication of devices with local gate

In addition to samples including source-drain and back gate, we also fabricated devices with an additional local gate (Fig. 4.5a). Due to the small gap size of the source-drain electrodes, the local gate is placed at a lower level than the electrodes to avoid electrical shortcuts between them [9]. Figure 4.5 shows a schematic and a SEM image of a local gate device.

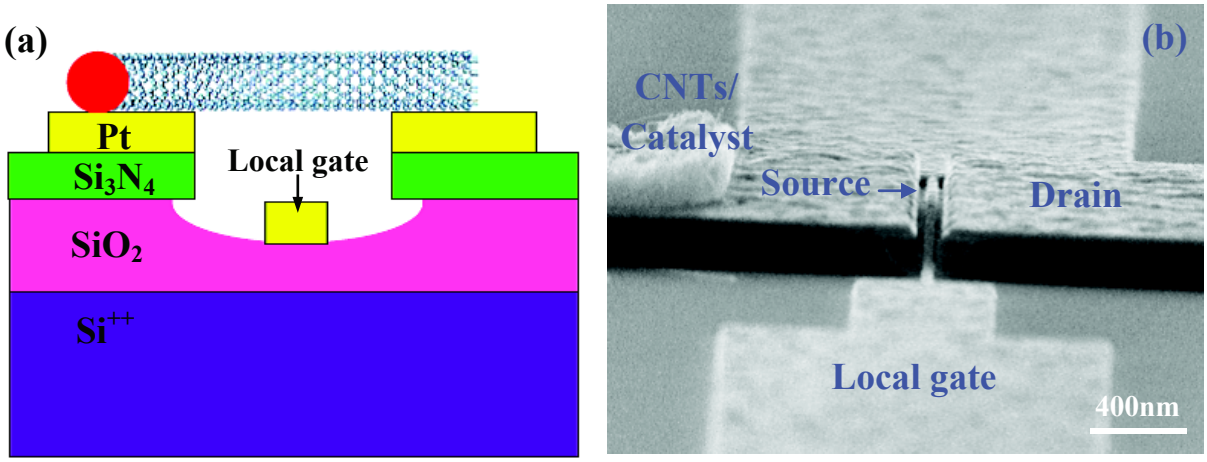

Figure 4.5. Fabrication of a local gate device. (a) Schematic and (b) SEM image of a final device. The arrow is at the position of the suspended CNT.

The fabrication of the local gate devices is similar to what was described in the previous sections, except some additional steps. At the first step, a layer of 50 nm Si_3N_4 is deposited on top of the wafer. The source-drain electrodes are then fabricated as shown in section 4.2.1. The following etching steps, anisotropic etching of Si_3N_4 by SF_6 RIE and then buffered HF isotropic etching of SiO_2, form an undercut of ~ 150 nm. The local gate is then aligned in the middle of the source and drain, using two electron beam lithography and metal evaporation steps comparable to those described before. We noticed that the use of the Si_3N_4 layer and the undercut profile are necessary to avoid any current leakage when a voltage is applied between the local gate and the source/drain electrodes.

4.3. Device characterizations at room temperature

After all the patterning steps, the wafer is cut into many small pieces for catalyst deposition and CVD growth. The samples after the CVD growth are first characterized at room temperature in a probe station. Each sample includes 4x4 chips and each chip has 14 junctions for the design of Fig. 4.4. Then in each sample, there are typically ~ 200 possible junctions. It is indeed necessary to probe and select many junctions at room temperature, since fabrication success rate is rather low (only 2 – 5 % of the junctions are further studied at very low temperatures). In the following, we describe the measurement setup used to characterize the devices (section 4.3.1). This characterization gives us interesting information about the nanotube type (metallic or semiconducting) and the amount of gate hysteresis (section 4.3.2).

4.3.1. Measurement setup

Room temperature device characterization typically consists in measuring the conductance between source and drain electrodes, while sweeping the gate voltage. This is done using a cryogenic probe station (mainly used at room temperature here), connected to the measurement chain controlled by the home-made NanoQt software.

Probe Station

The cryogenic probe station used in this work is the commercial LakeShore TTPX model, which can operate over a temperature range of 4.2 K (of liquid ^{4}He) to 475 K (by a heater). The system is configured with six ultra-stable micromanipulated probe arms providing a precise 3-axis control to land the probe tip accurately on device features. Since the working chamber is connected to a Turbo pump, samples are probed in vacuum, which is important to avoid the effect of adsorbed molecules on the gate hysteresis of the CNT measurement. Moreover, the CNT is well isolated and screened inside the probe station because an electrical or thermal shock from the user or the measurement chain may indeed destroy the CNT junctions. Our probe station is shown in Fig. 4.6.

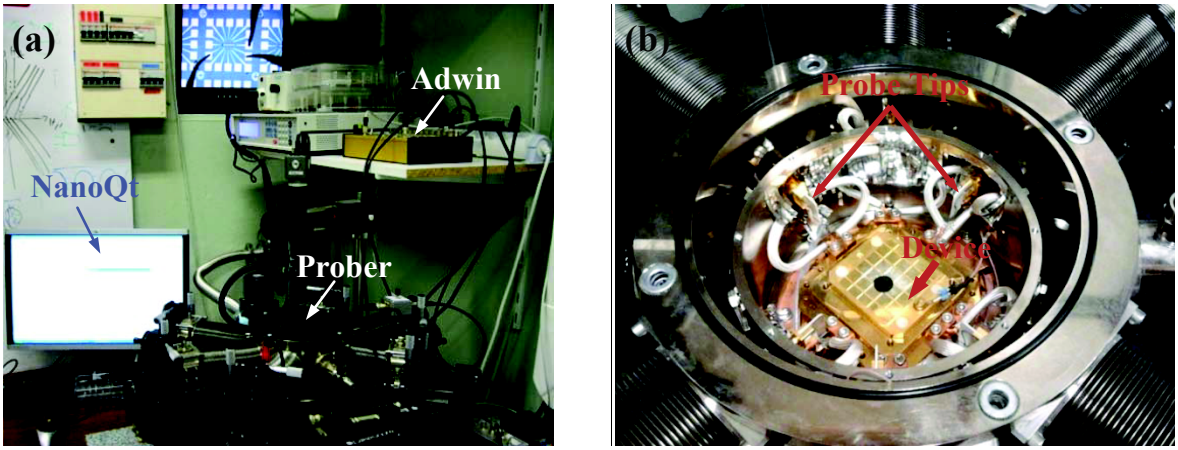

Figure 4.6. The probe station setup for characterization of the CNT samples at room temperature. (a) Outside view of the whole measurement setup. (b) Inside of the probe chamber.

Measurement chain

In this thesis, we mainly used a voltage bias measurement scheme schematically represented in Fig. 4.7a. The nanotube junctions are subjected to an applied voltage in the typical range of few mV. The induced current passing through the device is then converted to a voltage, amplified, and measured by lock-in technique (ADwin Pro). The gain of the pre-amplifier, typically ranging from 10^7 to 10^9 in our measurements, can be tuned by changing the value of R_c of the I-V converter. In addition to this, voltages are applied to the gate electrodes (V_{BG}: back gate, V_{LG}: local gate), through 1 MΩ resistors.

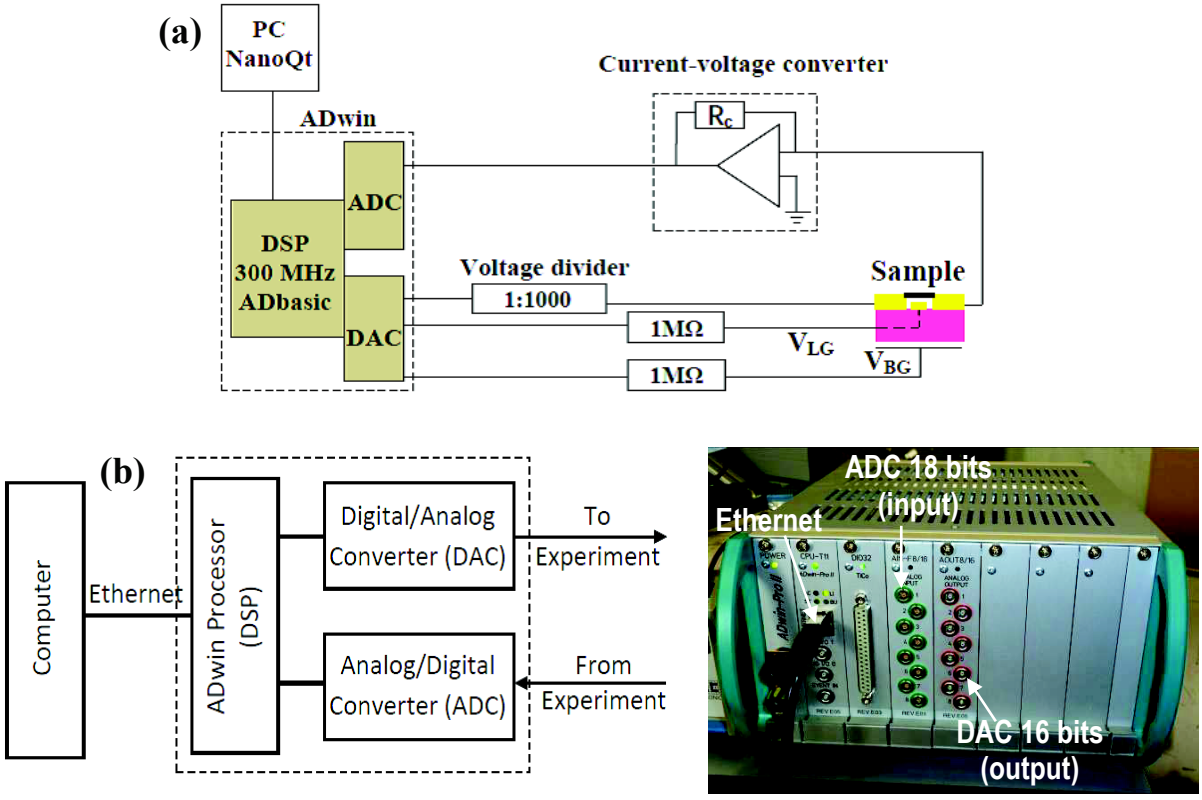

Figure 4.7. Measurement scheme of the CNT junction. (a) Schematic of the entire chain. The computer provides a graphical interface to the user and allows the storage of data. ADwin processor (Digital Signal Processor (DSP) optimized for calculating) ensures real-time function. The digital/analog converter (DAC) and analog/digital converter (ADC) respectively generates and receives the experimental signals. The conversion resistor (R_c) of the current-voltage converter sets the amplifier gain. (b) Schematic and front view of the ADwin-Pro. The different inputs (DAC) are circled in green while the outputs (ADC) are circled in red.

During the electrical measurement of CNTs, it is necessary to generate and measure simultaneously more than one voltage and to detect very weak signals using lock-in detection. These can be done by using a standard measurement chain with various devices for each task. All these devices are linked together by the common mass, which may form several "ground loops". This typically results in a strong noise in the measurements. However, we use an ADwin [10], which make the interface between the computer and all the analog parts of the measurement chain in one box. The number of loops is therefore limited and the noise is reduced. The digital/analog converter (DAC) and analog/digital converters

(ADC) in the Adwin are encoded on 16 and 18 bits, respectively. A schematic and the front of an Adwin-Pro are shown in Fig. 4.7b.

In addition, ADwin provides the advantage of being a "real time" electronic system with its own processor. The processor of the ADwin, with 300 MHz clock frequency, ensures that the sequence of instructions defined by the user is repeated every 3.3 ns. In contrast to the ADwin, computers and associated operating systems (Windows, Mac OS, Linux) provide a "multi-task" platform. They are developed to perform several tasks in parallel (office, internet, video ...) but not to ensure a time base. It is thus difficult to repeat a loop with a period less than ten milliseconds using a software such as LabView or LabWindows running on a multi-task platform.

All the measurements in this work are performed by using an ADwin Pro real time acquisition system programmed in a lock-in mode [11]. Communication between the Adwin and the PC is achieved by a program named NanoQT, which has been developed by Edgar Bonet and Christophe Thirion in the group and is in operational since 2009. The program is compiled on the PC and its instructions are sent to ADwin via a RJ45 wire (ethernet). Programming of the ADwin processor offered by the manufacturer is the ADbasic language. In order to have a versatile and user-friendly interface, NanoQT is based on two layers of programming: C^{++} low-level layer and JavaScript in the user layer. The user just defines the sequences of his action by the intermediate scripts, which are then interpreted into C^{++} and sent to the ADwin following exchange protocols. The ADwin subsequently sends the instructions and receives the measured data in its own time base and then returns to NanoQt for processing in the PC time base.

4.3.2. Room temperature conductance measurements

In this characterization, we measure the gate dependence of the differential conductance $G = \mathrm{d}I/\mathrm{d}V$ between source and drain electrodes. The gate voltage (back gate or local gate) is swept from negative to positive values (trace) and via reverse (retrace). The bias voltage is usually kept at zero.

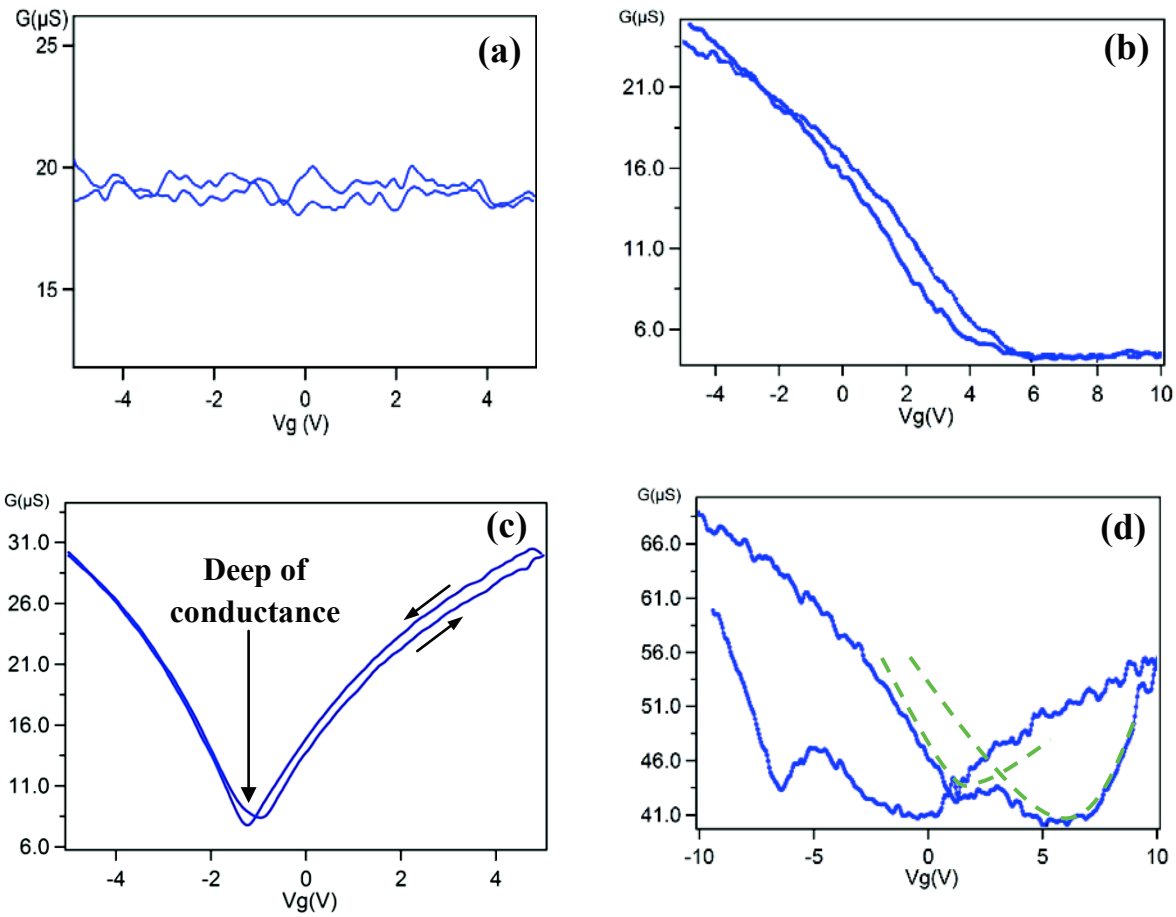

Figure 4.8. Typical gate dependence of the conductance at room temperature. The main behaviors are of respectively: (a) metallic, (b) semiconducting (only the p band is seen here), (c, d) small band gap CNTs.

First of all, any junction having a conductance higher than four times of the conductance quantum, $G > 4G_0 = 152$ μS (or $R < 6.45$ kΩ, with G[S] = 1/R[Ω]) is rejected since these cannot be individual nanotubes [12]. Instead of that, junctions with a relatively moderate conduction $G \sim 10$-100 μS at $V_g = 0$ (R ~ 100 – 10 kΩ) are preferred in our studies. In this range of G, different types of $G(V_g)$ can be found, which represent different electrical characteristics of the CNTs (Fig. 4.8).

Figure 4.8a shows a flat G (V_g) curve with almost no gate dependence. This is the expected behavior of a metallic CNT. Due to the "zero-gate dependence" characteristic of the metallic CNT, we do not know whether the measured data are from one or several CNTs, or even from some conductive objects which are not CNTs.

Figure 4.8b, however, is the gate dependence of conductance of a semiconducting CNT. The conduction band (for electrons) of the CNT cannot be reached even when we applied a relatively large positive voltage.

Figure 4.8c is the G (V_g) of a small band gap CNT, which shows a deep in conductance near $V_g = 0$. The single deep is also a signature of an individual CNT over the junction. For the studies carried out in this work, we mainly used small band gap nanotubes, where the electron and hole regimes can be reached easily with relatively small voltages.

Figure 4.8d also shows the characteristics of small band gap nanotube junctions. Nevertheless, the two deeps in the $G(V_g)$ curve (two green dashed lines) are an indication that probably several nanotubes are electrically connected to the junction. As mentioned in section 4.2.2, the CNTs grow randomly from the catalyst islands, and several tubes may be in contact with the same pair of source-drain electrodes.

After identifying promising devices with the probe station, the wafer piece is glued, wirebonded onto a chip carrier and then mounted in a dilution refrigerator. The next section will briefly describe the cryogenic techniques used to reach very low temperatures.

4.4. Dilution refrigerator

The electronic transport properties of CNT devices are measured in a cryogenic system at very low temperatures. The easiest way is to dip the sample in a liquid helium dewar and perform the measurement at 4.2 K. Lower temperatures (40 mK) can be reached by using the ^{3}He/^{4}He dilution refrigerator (Fig. 4.9). In the following, its operation principle is briefly described. First, the whole system including the sample is immersed in a liquid ^{4}He dewar and stabilized at 4.2 K. Then, a high vacuum jacket has to be created to thermally isolate the dilution unit from the dewar before starting the cooling process.

The ^{3}He/^{4}He mixture is first condensed and cooled down to 1.2 K by using the cooling power of a ^{4}He pumped evaporator (1 K pot). By pumping the ^{3}He gas in the still operated at 0.7 K, ^{3}He of the diluted phase flows from the mixing chamber up to the still due to an osmotic pressure difference. The ^{3}He percentage of the diluted phase in the mixing chamber is then reduced, which leads to the transfer of ^{3}He from the concentrated phase to the diluted phase to uphold the right concentration (6.6%) of ^{3}He in the mixing chamber.

Since the enthalpy of ^{3}He in the dilute phase is larger than that of in the concentrated phase, cooling is achieved by transferring ^{3}He atoms from the pure ^{3}He phase to the diluted phase. The system can reach a base temperature of 40 mK. The flow of cold 3He from the mixing chamber to the evaporation chamber is utilized to pre-cool the incoming ^{3}He in a heat exchanging process. The closed circuit allows a continuous condensation and maintains the system at base temperature, and the measurements can be performed for months. The electronic temperature is estimated of ~ 150 mK. More theoretical and practical details of the dilution and cooling mechanism can be found in ref. [13].

The principle of measurements at very low temperatures is similar to those at room temperature, except there is an additional application of magnetic field. The cryostat setup is equipped with superconducting magnets, where the magnetic amplitudes of x, y, z direction (and their combinations) can be control through an Adwin and a NanoQt software. The maximum amplitude of x and y components is 3 T and 1.5 T, respectively.

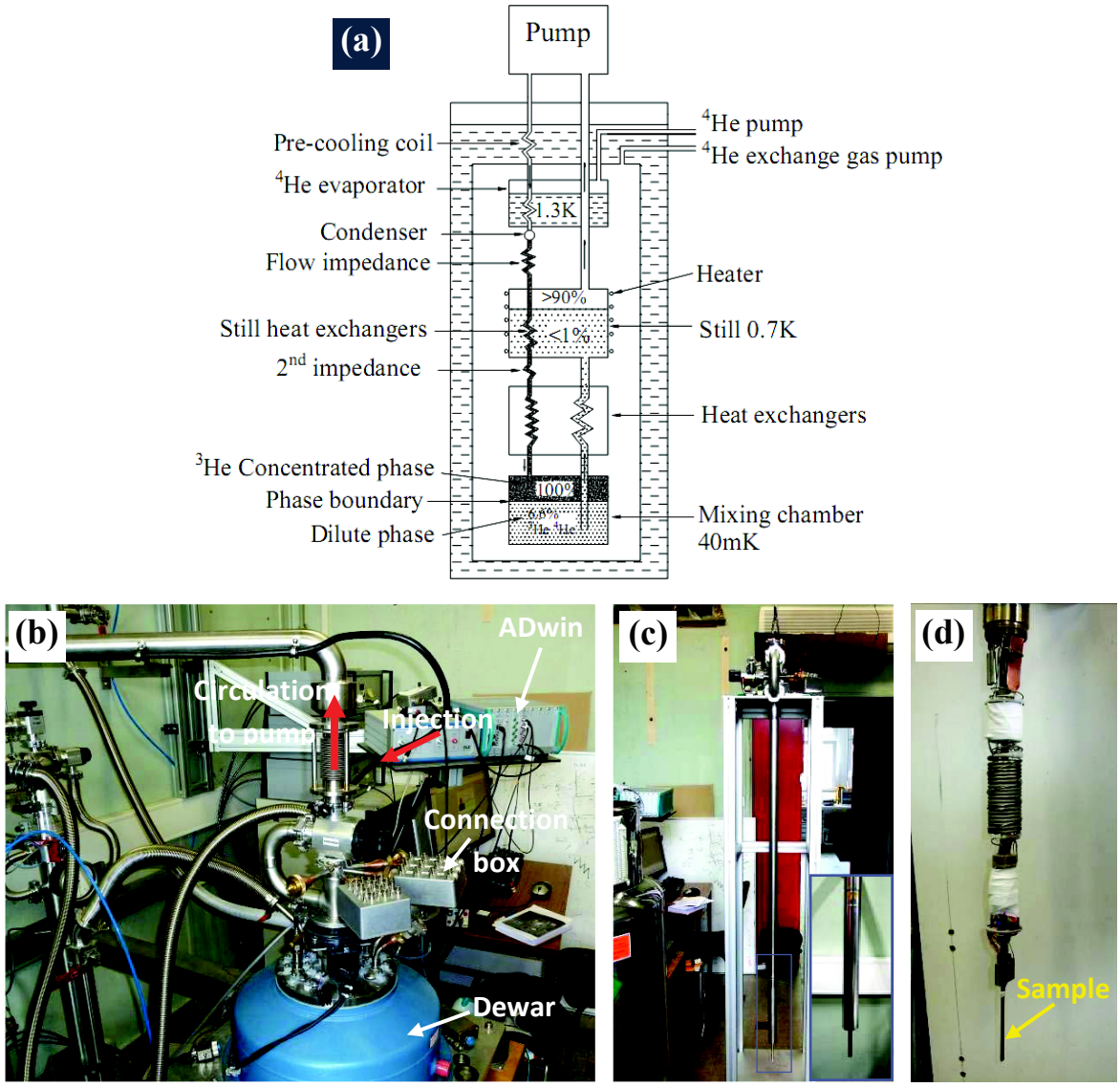

Figure 4.9. (a) Schematic of ^{3}He/^{4}He dilution system. This part sits in a vacuum chamber that is immersed in a ^{4}He bath at 4.2 K. The incoming ^{3}He gas is condensed on a continuously operating ^{4}He pot at 1.2 K. A rotary pump drives the mixture around in the circuit. The mixture separates in two phases in the mixing chamber, where the condensed phase of ^{3}He floats on the diluted phase of ^{3}He/^{4}He. When we pump the ^{3}He from the diluted phase at the still, ^{3}He in the concentrated phase traverses through the phase boundary to the dilute phase to maintain a certain percentage of ^{3}He in the diluted phase (6.6%), and cool the mixing chamber down to 40 mK [13]. (b) Image of the whole setup from outside. (c) The dilution before dipping into the dewar. (d) Sample on sample holder fixed with connection socket.

4.5. Conclusion and perspectives

In conclusion, we have fabricated ultraclean CNT devices and presented the techniques for room and low temperature measurements. State of the art EB lithography process has been used for the nanofabrication of the devices with different designs. The as-grown CNT junctions are selected at room temperature by probing in a station without any SEM observation. The selected junctions are then studied at very low temperatures as will be described in the next chapters.

The developed fabrication technique enabled us to make very high quality nanotube junctions. Nevertheless, it should be noted that this technique still suffers from its main drawback of high CVD temperature, which may damage the metallic electrodes and restrict the choice of material (high melting and boiling point, no metal carbide formation at high temperature …). To avoid this, another strategy have been developed very recently [14], where the CNTs are first grown on a separate quartz substrate, and then aligned and directly transferred to the prefabricated electrodes at room temperature. This technique may open more opportunities for ultraclean CNT device fabrication, especially regarding material choice. Despite the interesting perspectives of this technique, few studies have been published yet.

References

[1] M. S. Dresselhaus, G. Dresselhaus, and P. Avouris, Eds., *Carbon Nanotubes: Synthesis, Structure, Properties and Applications*, 1st ed. Springer, 2001.

[2] J. Kong, H. T. Soh, A. M. Cassell, C. F. Quate, and H. Dai, "Synthesis of individual single-walled carbon nanotubes on patterned silicon wafers," *Nature*, vol. 395, no. 6705, pp. 878–881, Oct. 1998.

[3] N. R. Franklin, Q. Wang, T. W. Tombler, A. Javey, M. Shim, and H. Dai, "Integration of suspended carbon nanotube arrays into electronic devices and electromechanical systems," *Applied Physics Letters*, vol. 81, no. 5, pp. 913–915, Jul. 2002.

[4] P. G. Collins, "Defects and disorder in carbon nanotubes," in *Oxford Handbook of Nanoscience and Technology: Frontiers and Advances*, Oxford: Oxford Univ. Press, 2009.

[5] A. Candini, C. Alvino, W. Wernsdorfer, and M. Affronte, "Hysteresis loops of the magnetoconductance in graphene devices," *arXiv:1101.3030*, Jan. 2011.

[6] J. Cao, "Ultra high quality suspended carbon nanotubes: Electro-mechanical and Electro-magnetic properties," Stanford, 2005.

[7] F. Kuemmeth, S. Ilani, D. C. Ralph, and P. L. McEuen, "Coupling of spin and orbital motion of electrons in carbon nanotubes," *Nature*, vol. 452, no. 7186, pp. 448–452, Mar. 2008.

[8] A. K. Huttel, G. A. Steele, B. Witkamp, M. Poot, L. P. Kouwenhoven, and H. S. J. van der Zant, "Carbon Nanotubes as Ultrahigh Quality Factor Mechanical Resonators," *Nano Letters*, vol. 9, no. 7, pp. 2547–2552, Jul. 2009.

[9] J. Kong, B. J. LeRoy, S. G. Lemay, and C. Dekker, "Integration of a gate electrode into carbon nanotube devices for scanning tunneling microscopy," *Applied Physics Letters*, vol. 86, no. 11, pp. 112106–112106–3, Mar. 2005.

[10] "ADwin." [Online]. Available: http://www.adwin.de/us/produkte/proII.html.

[11] "About Lock-In Amplifiers." [Online]. Available: http://www.thinksrs.com/downloads/PDFs/ApplicationNotes/AboutLIAs.pdf.

[12] P. McEuen, "Nanostructures," in *Introduction to solid state physics*, 8th ed., John Wiley & Sons, Inc., 2004.

[13] F. Pobell, *Matter and Methods at Low Temperatures*, 2nd ed. Springer, 2002.

[14] C. C. Wu, C. H. Liu, and Z. Zhong, "One-Step Direct Transfer of Pristine Single-Walled Carbon Nanotubes for Functional Nanoelectronics," *Nano Letters*, vol. 10, no. 3, pp. 1032–1036, Mar. 2010.

Chapter 5. Electronic properties of carbon nanotubes quantum dots

5.1. Introduction

Since their discovery, carbon nanotubes (CNTs) have attracted tremendous interest of the scientific community due to their unique physical properties. When a CNT short segment is connected to metal electrodes, it behaves as a quantum dot (QD) at low temperatures. The QDs are known as artificial atoms, with features close to those of real atoms. However, QDs present the advantage over the real atoms, that the attractive potential of a positive nucleus is replaced by a confinement potential which can be controlled and tuned to a certain amount in laboratory conditions. In this chapter, we review the main characteristics of CNT quantum dots. Section 5.2 introduces the QDs in general, which is followed by the electrical transport in Coulomb blockade regime of weakly coupled QD to electrodes (section 5.3). In section 5.4, we introduce the properties of CNT QDs. In particular, we present the typical four-fold degenerate energy shell structure of CNT QDs. More recently, the study of ultraclean CNT QDs contradicted these previous finding, showing that orbital and spin degrees of freedom in CNTs are not independent. This spin-orbit coupling, affecting strongly the CNT energy spectrum is presented in section 5.5. In section 5.6, we go beyond the sequential electron tunneling regime of Coulomb Blockade and introduce higher-order electron tunneling (co-tunneling) and the Kondo effect, arising in a CNT QD more strongly coupled to the metallic leads. In particular, we introduce the typical SU(4) symmetric Kondo effect in CNT QDs.

5.2. Quantum dots

Quantum dots are 'small' structures that can be filled with electrons or holes. In quantum mechanics, the wave vector of the electron will be quantized when its wavelength is comparable to dimension of the system, thus a set of discrete energy states is formed. A system is called quantum dot when the electrons are confined in all spatial directions and the system becomes zero dimensional. The separation between the energy levels must be

observable at the experimental temperature at below a few Kelvin. Because a quantum dot is such a general kind of system, there are quantum dots existing in different sizes and materials: single molecules [1], metallic nanoparticles [2], lateral or vertical dots in semiconductor heterostructures [3], [4], semiconducting nanowires [5], or carbon nanotubes [6], as shown in Fig. 5.1.

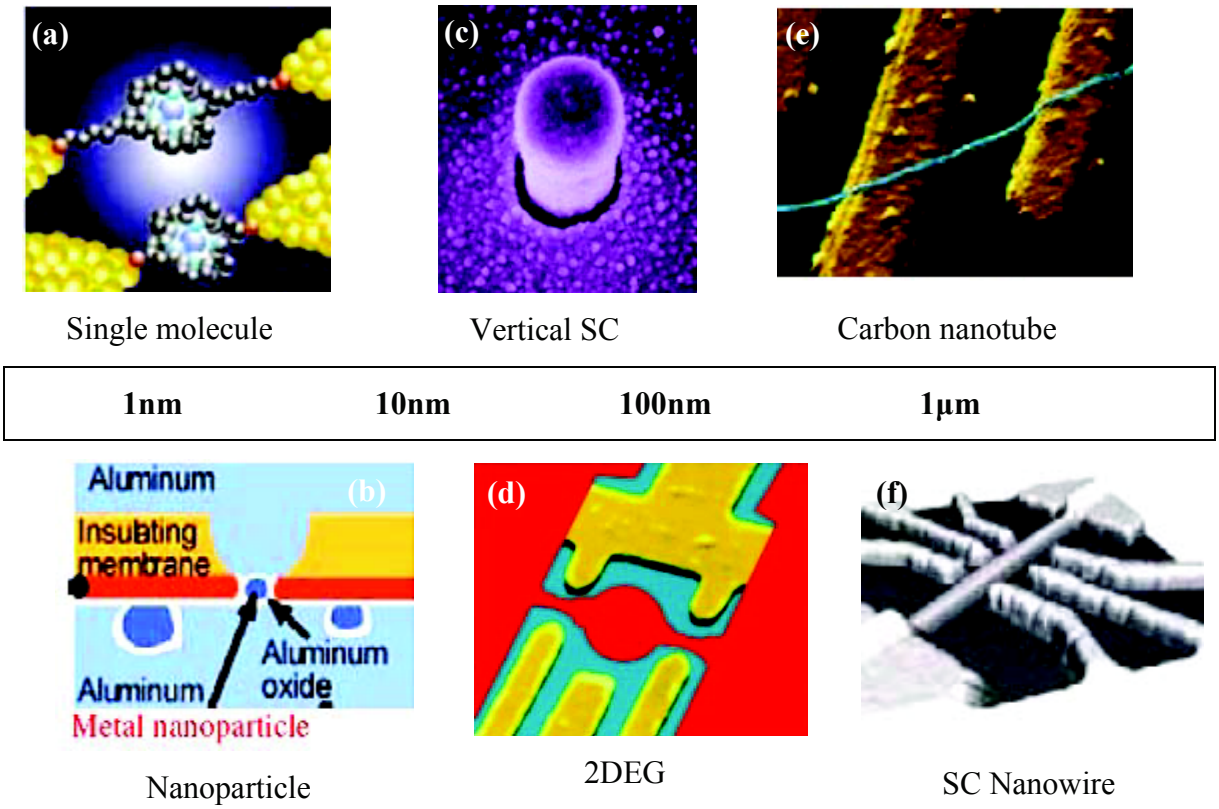

Figure 5.1. Examples of quantum dots of different sizes and materials. (a) single molecule [1], (b) metallic nanoparticle [2], (c) vertical semiconducting dot [3], (d) two dimentional electron gases [4], (e) carbon nanotube [6], (f) semiconducting nanowire [5].

In order to measure electrical transport through a quantum dot, the dot must be coupled via tunnel barriers to reservoirs with which electrons can be exchanged. The dot is also capacitively coupled to one or more gate electrodes, which can be used to tune the electrostatic potential of the dot with respect to the reservoirs. A representative schematic of a quantum dot measurement configuration is shown in Fig. 5.2.

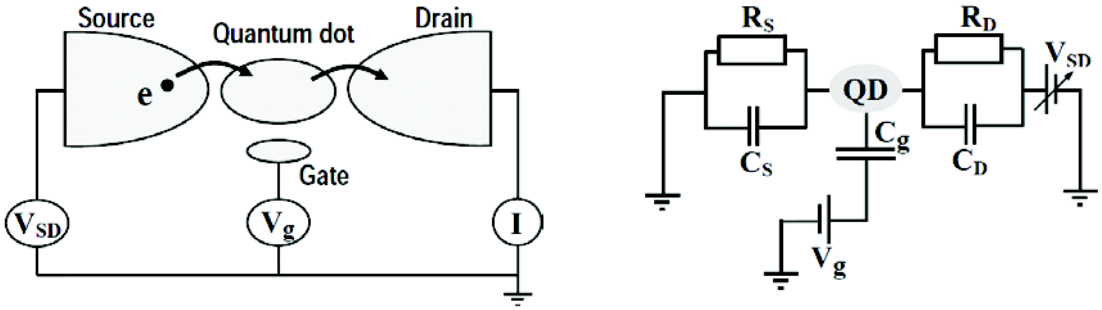

Figure 5.2. Schematic of a quantum dot (left) and its equivalent circuit (right). The quantum dot is connected to source and drain contacts via tunnel barriers, represented by resistances R_S and R_D and capacitances C_S and C_D, respectively, and capacitively coupled to the back gate (Cg). The current through the device (I_{QD}) can be measured in response to a bias voltage (V_{SD}), and a gate voltage (Vg). The system is represented by a RC circuit [7].

5.3. Coulomb blockade

To understand the electrical transport through a quantum dot, the constant interaction (CI) model is used. In this model, the Coulomb interactions among the electrons in the dot, and between the electrons in the dot and those in the environment are parameterized by a constant capacitance $C = C_S+C_D+C_g$. In addition, the discrete energy spectrum is assumed to be independent of the number of electrons on the dot [7]. The total energy *U(N)* of a dot with N electrons in the ground state with the applied source-drain voltage V_{SD} (the drain is grounded) and gate voltage V_g is given by:

$$U(N) = \frac{\left[-|e|(N-N_o)+C_S V_{SD}+C_g V_g\right]^2}{2C} + \sum_{n=1}^{N} E_n(B) \qquad (5.1)$$

where -|e| is the electron charge, N_o is the number of electrons in the dot at zero gate voltage, and B is the magnetic field. The terms $C_S V_{SD}$ and $C_g V_g$ can be changed continuously, and represent an effective induced charge that changes the electrostatic potential on the dot. The last term of Eq. 5.1 is a sum over the occupied single-particle energy levels $E_n(B)$ which depend on the characteristics of the confinement potentials. The electrochemical potential *μ(N)* of the dot is shown in Fig. 5.3 and defined as:

$$\mu(N) = U(N) - U(N-1) = (N - N_o - \frac{1}{2})\frac{e^2}{C} - \frac{|e|}{C}(C_S V_{SD} + C_g V_g) + E_N \qquad (5.2)$$

$$= (N - N_o - \frac{1}{2})E_C - \frac{E_C}{|e|}(C_S V_{SD} + C_g V_g) + E_N$$

where $E_C = e^2/C$ is the charging energy.

The discrete levels are separated by an addition energy defined by:

$$E_{add} = \mu(N+1) - \mu(N) = E_C + \Delta E \qquad (5.3)$$

The addition energy consists of a purely electrostatic part, namely the charging energy E_C, plus the energy spacing between two discrete quantum levels, ΔE. Note that ΔE can be zero, when two consecutive electrons are added to the same spin-degenerate level or if there are additional degeneracies present.

For the electrical transport to occur, energy conservation must be satisfied. This is the case when an electrochemical potential level lies within the "bias window" between the electrochemical potential (Fermi energy) of the source *(μ_S)* and the drain *(μ_D)*, i.e. $\mu_S > \mu > \mu_D$ with $\mu_S - \mu_D = -e|V_{SD}|$ (Fig. 5.3a). An electron can tunnel from the source onto the dot, and then tunnel off to the drain without losing or gaining energy. If no level lies within the bias window (Fig. 5.3b), the electrons are fixed inside the dot and there is no current flow. This is known as Coulomb blockade.

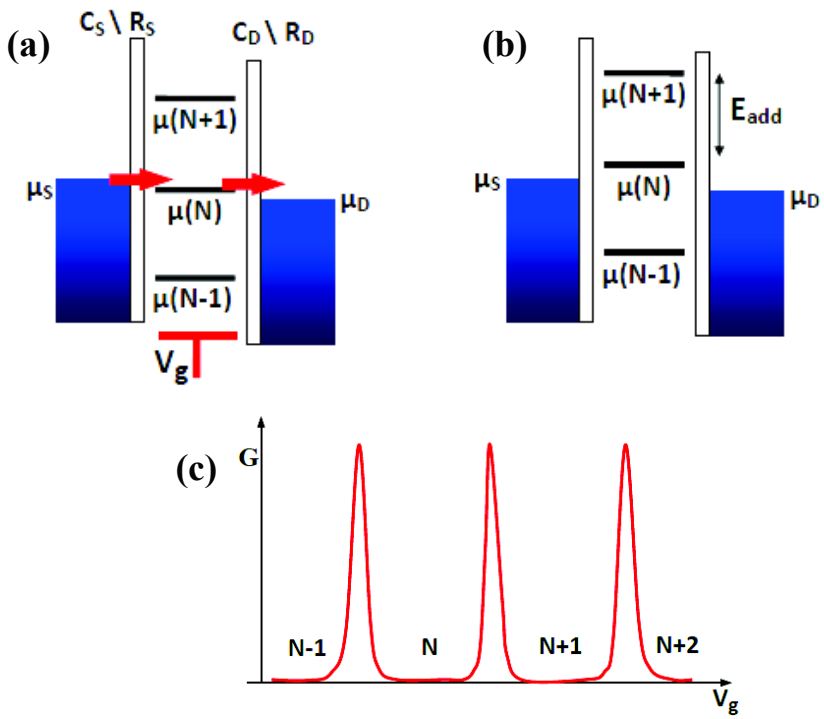

Figure 5.3. Schematic diagrams of the electrochemical potential of the quantum dot for different electron numbers. There are two ways to change the electrochemical potential: opening the bias window relatively to the level, or applying a gate voltage to shift the whole 'ladder' of the energy levels. (a) The μ(N) level is aligned and the electron can tunnel on/out of the QD. (b) No level drops in the bias window of μ_S and μ_D, the electron number is fixed at (N-1) due to Coulomb blockade. (c) Coulomb oscillation of linear conductance *($G=dI_{QD}/dV_{SD}$)* versus gate voltage (V_g). The valleys correspond to Coulomb blockade.

Since the dot is very small, it has a very small capacitance and therefore a large charging energy, e.g. Ec ~ few meV for a typical QD. The charging energy becomes important when it exceeds the thermal energy (e.g. k_BT ~ 0.36 meV at 4.2 K which is the temperature of liquid ^{4}He), and when the tunnel barriers are sufficiently opaque. The electrons thus are located either in the reservoirs or in the dot. A lower bound for the tunnel resistances R_t of the barriers can be found from the Heisenberg uncertainty principle. The typical time Δt to charge or discharge the dot is given by the R_tC-time, due to RC representative circuit of the quantum dot. This yields $\Delta E.\Delta t = (e^2/C)(R_tC) > h$. Hence, R_t should be much larger than the quantum resistance h/e^2 = 25.8 kΩ to sufficiently reduce the uncertainty in the energy and ensure Coulomb blockade.

The Coulomb blockade can be lifted by applying the gate voltage (V_g) to shift the whole "ladder" of electrochemical potential levels up or down, or changing the bias voltage (V_{SD}) to open the bias window. When the μ(N) drops into the bias window, the Nth electron can tunnel from the dot to the drain followed by a tunneling of another electron from the source onto the dot. The number of electrons in the quantum dot then alternates between N-1 and N. Because of the prominent of charging energy, this tunneling is sequential and the QD works as single-electron transistor. By measuring the differential conductance *($G=dI_{QD}/dV_{SD}$)* through the quantum dot while sweeping the bias voltage and changing the gate voltage value, one obtains the stability diagram of the quantum dot as shown in Fig. 5.4.

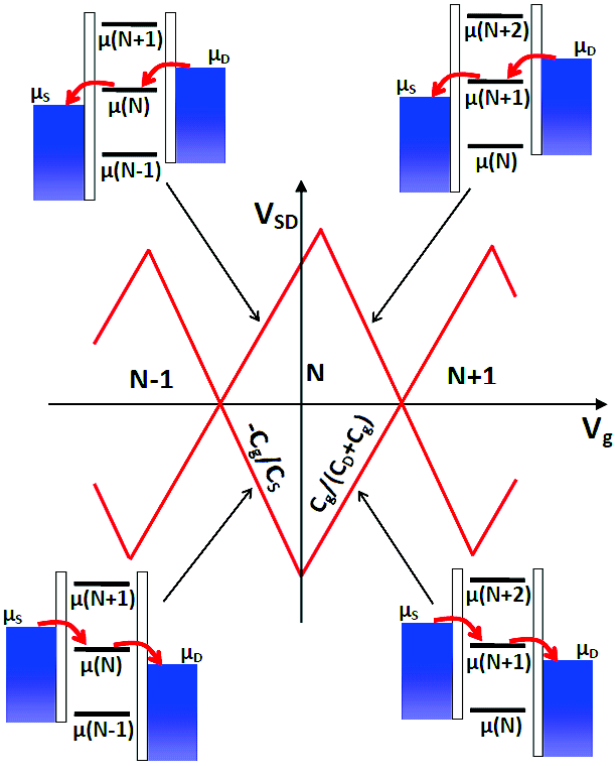

Figure 5.4. Coulomb "diamonds" of differential conductance, dI_{QD}/dV_{SD}, versus V_{SD} and Vg. The edges of the diamond-shaped regions correspond to the onset of current. At several positions, the level alignment is indicated with its schematic diagram. The slopes of different lines are related to different capacitances between electrodes and the QD.

In Fig. 5.4, there are four different situations for which the threshold current flow is reached. The edges of the diamond-shaped regions correspond to the onset of current where the dot turns from OFF to ON state, or reverse. Inside the diamond-shaped region, the number of electrons is fixed due to Coulomb blockade, and no current flows. Outside the diamonds, Coulomb blockade is lifted and the tunneling can take place. At the junction of

two diamonds, the energy level is aligned with both μ_S and μ_D, and a current can flow even if V_{SD} is infinitely small. These special points are called charge degeneracy points. From the size of Coulomb diamonds, different parameters of the quantum dot like Ec, E_{add}, Cg, C_S, C_D can be estimated [7].

In case that the V_{SD} increases so that both the ground state and an excited state fall within the bias window, an electron can choose to tunnel not only through the ground state μ(N), but also through an excited state μ*(N) (Fig. 5.5a). This leads to a change in the total current through the QD. It is worth noting that due to Coulomb blockade, the electron can tunnel into the dot either on the ground state μ(N) or the excited state μ*(N), but not at the same time. Moreover, if the value of the polarization becomes larger than the energy addition, two electrons can tunnel simultaneously across the island (Fig. 5.5b). The Nth electron will have two paths available μ(N) or μ*(N), and the (N+1) has one path μ(N + 1) for the tunneling. The number of electrons in the quantum dot will then alternate between (N-1), N and (N + 1).

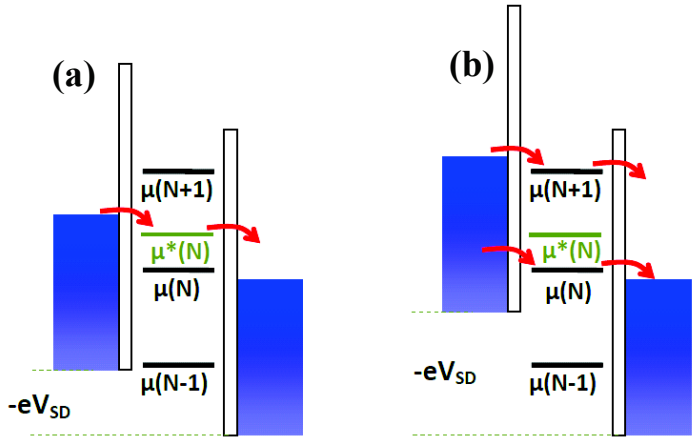

Figure 5.5. Schematic diagrams of the electrochemical potential levels of a quantum dot in the large-bias regime. (a) $eV_{SD} > \Delta E$: the electrons can tunnel on μ(N) or μ*(N) but not at the same time. (b) $eV_{SD} > E_{add}$: two electrons can simultaneously tunnel across the dot.

5.4. CNT four-fold energy level structure

As introduced in chapter 2, CNTs behave as 1D conducting channels owing to the combination of graphene band structure and quantization of $k_{\perp}$ momentum in the transversal direction. When a CNT is attached to two metallic contacts, the influence of quantum confinement (at temperature low enough) becomes relevant and the CNT junction behaves as a quantum dot (0D) with discrete energy levels. Tunnel barriers develop naturally at the CNT-metal interfaces due to the difference in work functions of these materials. The CNT QD length, L, is defined by the CNT segment length lying between the two electrodes (Fig. 5.6a). Due to the confinement of the electrons in the CNT portion, the electronic waves are partly reflected at the interfaces of the metal contacts and interfere with each other. The $k_{//}$ wave vector in the longitudinal direction is thus quantized, with a typical spacing inversely proportional to the CNT length: $\Delta k_{//}=\pi/L$. The formation of discrete energy levels in metallic and semiconducting CNTs is illustrated in Figs. 5.6.b, c. The quantized values of the wave vector in the longitudinal direction k_1, k_2, k_3 intersect the lowest energy bands of the CNT at E_1, E_2, E_3, respectively, both in conduction band and valence band. The CNT QD has thus discrete energy levels separated by the level spacing ΔE. In the CNT band structure, two equivalent dispersion cones (K' and K) in graphene lead to doubly-degenerate electronic orbitals (the orange and blue curves). This orbital degeneracy corresponds to semiclassical clockwise (CW) and counter-clockwise (CCW) electron orbits encircling the tube.

In addition to the unique two-fold degree of freedom leading to the doubly degenerate orbits, the electrons can have different spins, yielding a four-fold degenerate electronic spectrum. Such a group of four levels is called a "shell", each shells are separated by the level spacing ΔE. It is worth noting that, we cannot define exactly the total number of electrons in a metallic CNT QD. The transport measurements in few-electron regime are thus realized in semiconducting and small band gap (quasi-metallic) CNT QDs, where individual electrons (or holes) can be added or removed to the conduction (or valence) band.

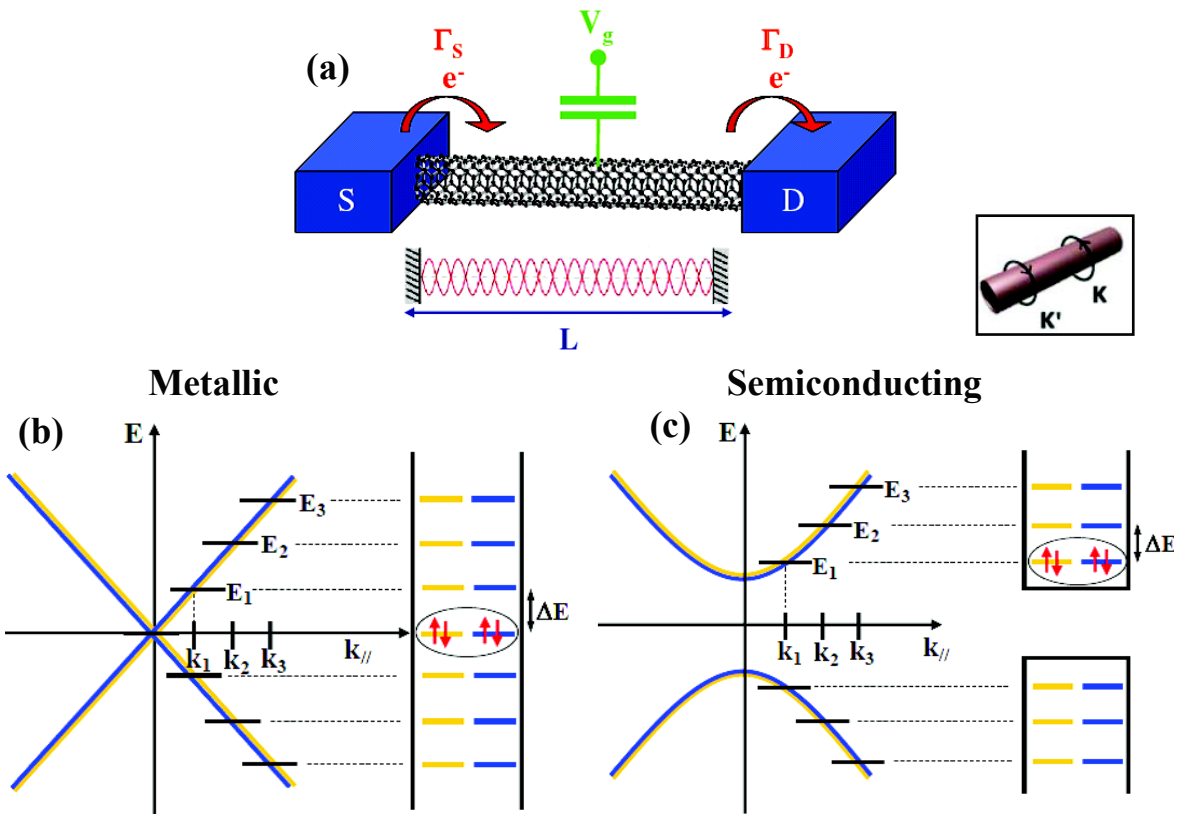

Figure 5.6. Schematic of a CNT QD and its energy level spectrum. (a) The QD is formed in the segment of CNT between the two electrodes, leading to a quantized energy spectrum in the longitudinal direction of the CNT. The CNT is capacitively coupled to a gate electrode controlled by the voltage V_g, shifting the energy levels in the CNT QD with respect to the Fermi level [8]. (b, c) Energy level spectrum of a metallic and semiconducting CNT QD, respectively. The wave vector $k_{//}$ intersects the CNT band structure at E_1, E_2, E_3, … . The two K' and K points of graphene lead to doubly-degenerate electronic orbital levels. This degeneracy can be seen as clockwise (CW) and counter-clockwise (CCW) electron motions through the CNT circumference (inset). The energy levels are four-fold degenerate due to spin and orbital degrees of freedom (and in agreement with the Pauli exclusion principle). Note that the energy level spacing, *ΔE,* for a semiconducting CNT QD is not constant due to the non-linear energy dispersion, especially strong close to the semiconducting gap.

The simple energy level scheme presented before has been confirmed by low temperature measurements of the addition energies in the Coulomb blockade regime (section 5.3). Figure 5.7a shows the result of such a measurement, where the current (or alternatively the differential conductance) through the device is plotted as a function of the gate and bias voltages (Fig. 5.4). Such a charge stability diagram shows a four-fold degenerate shell filling,

following the CI model [9]. Indeed, the addition energy of the Coulomb diamonds presents a four-fold symmetry, where sequences of three "small" diamonds of addition energies E_c followed by a "larger" one, are observed. The addition of an electron to a higher shell requires an extra energy of energy spacing ΔE, which translates into the largest Coulomb diamond (addition energy $E_c + \Delta E$). This pattern is especially well visible when $E_c \sim \Delta E$.

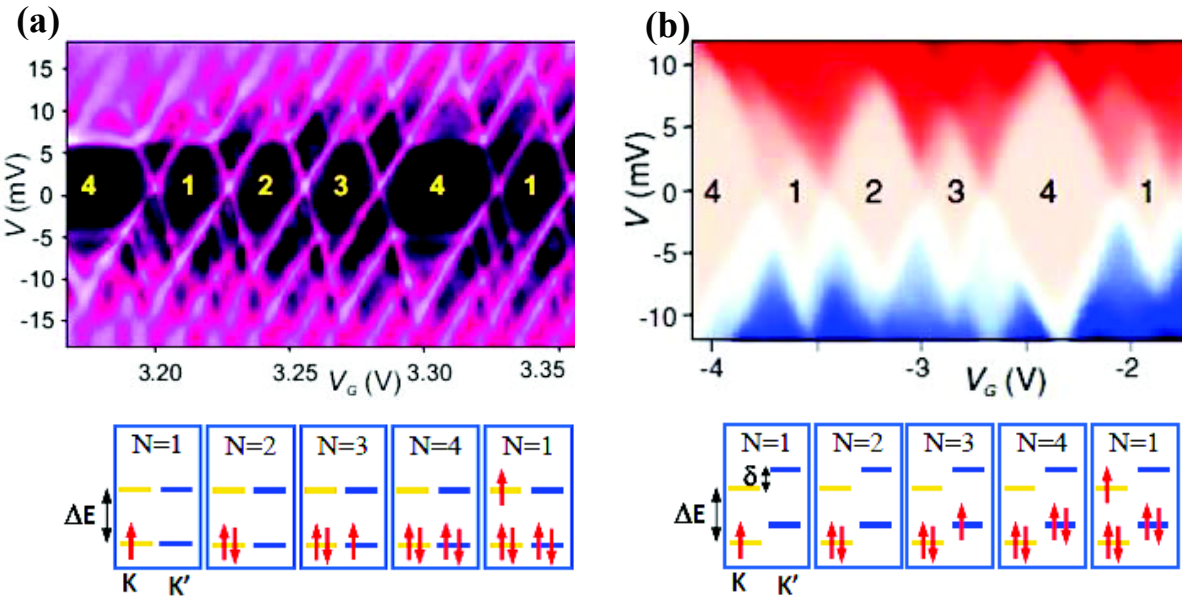

Figure 5.7. Measurements of addition energy of (metallic) CNT QDs. (a) Perfect four-fold level degeneracy, from ref. [10]. The addition energies follow the sequence [E_c, E_c, E_c, E_c+ΔE] (see inset). (b) An orbital energy mismatch leads to an increase of the addition energy for N=2, from ref. [11] and the sequence is now [E_c, E_c + δ, E_c, E_c+ΔE].

The four-fold degeneracy in the CNT energy spectrum (reflecting both spin (↑/↓) and orbital (K/K') degeneracies) has been very popular and in good agreement with many studies (Fig. 5.7a). First evidence of broken degeneracies had been observed in other devices, appearing as an increase of the N = 2 addition energy, with respect to the N = 1 and N = 3 cases (Fig. 5.7b) [9]. This difference between addition energies was interpreted as short range electron scattering induced by defects or impurities, creating a sub-band mismatch δ (also called $\Delta_{KK'}$) [12–16]. It thus lifts the orbital symmetry (inset of Fig. 5.7b) and creates two energy doublets, namely (K↑, K↓) and (K'↑, K'↓). A more accurate description of the energy spectrum [17] was obtained by including exchange energy J (favoring spin alignment) and additional Coulomb energy dU (to put two electrons of opposite spins into the same orbital level) [9], [17], [18].

In the previous description of CNT energy level spectrum, both spin and orbital degrees of freedom were assumed to be independent. In 2008, high resolution excited states level spectroscopy (Fig. 5.5) revealed a subtle interplay between spin and orbital degrees of freedom, namely the curvature enhanced spin-orbit coupling in CNTs [14], [16], [19]. The spin-orbit interaction splits the CNT energy spectrum degeneracy into two Kramers doublets with entangled orbital and spin degrees of freedom. This discovery has yield to a strong new interest in the field, motivating many studies (both theoretical and experimental) to understand and simulate this intriguing effect. In addition to its fundamental interest, spin-orbit coupling may open the way to an all electrical manipulation of electronic spins in addition to optical control of quantum information and currently motivates several studies for these purposes.

5.5. Spin-orbit coupling in CNTs

Spin-orbit interaction (SOI) is a well-known relativistic phenomenon that manifests itself in lifting some energy level degeneracies of electrons in atoms and solid state materials. In an atom, SOI is a relativistic interaction causing shifts in the electrons atomic energy levels due to electromagnetic interaction between the electron's spin and the effective magnetic field felt by the electrons orbiting around the nucleus [20]. Atom with higher atomic number exhibits stronger fields around the nucleus and hence stronger spin-orbit effect. Based on low atomic number Z = 6 of carbon atom, the spin-orbit effects are commonly assumed to be negligible in carbon based materials.

However in the case of nanotubes, this coupling have been argued to be significant due to their high curvature and cylindrical topology [19], [21], [22], and was recently observed in experiment [16] for the first time. In that work, the SO coupling splits each orbital quadruplet into two doublets with the value of ~ 0.4 meV at zero magnetic field, as shown in Fig. 5.8.

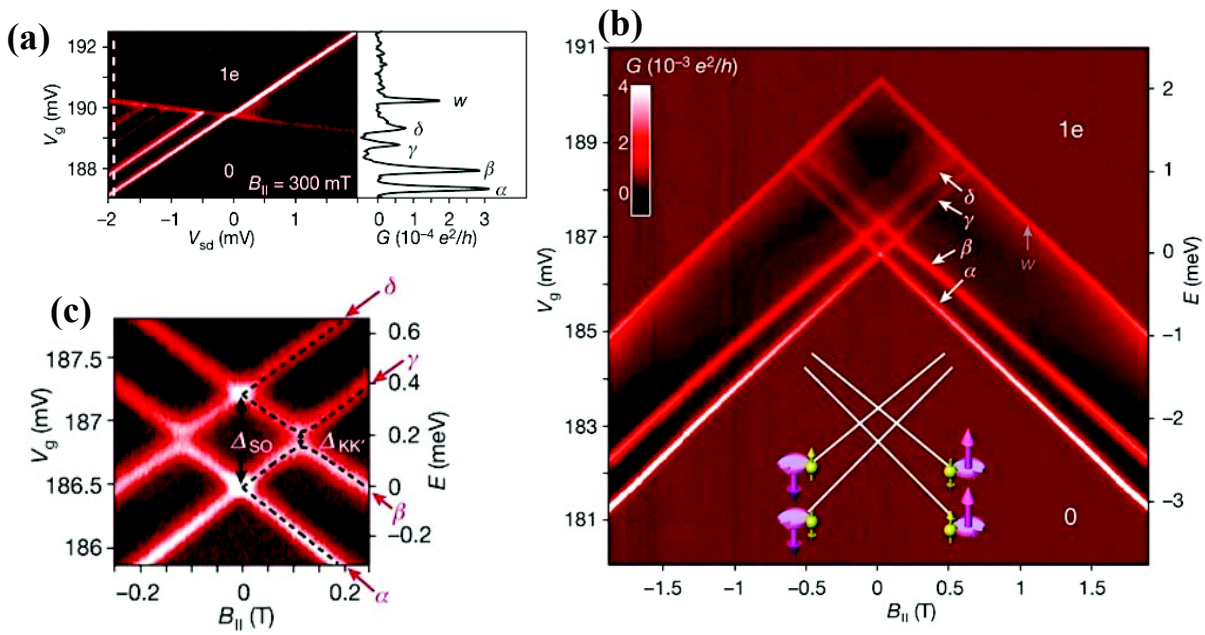

Figure 5.8. Experimental measurement of SO coupling from ref. [16]. (a) Map of conductance as a function of V_G and V_{SD} in the transition region of zero to one electron. α,β,γ,δ correspond to the excited states. (b) Single-electron chemical potentials versus the magnetic field parallel to the CNT axis. Inset is the assignment of orbital and spin magnetic moments. (c) The zoom of b, which shows the SO coupling value $\Delta_{SO} \sim 0.4$ meV at $B_{//}=0$.

The SOI in CNT includes two parts: the intrinsic SOI of graphene lattice (Δ_{int}) and the SOI due to the curvature (Δ_{curv}). The intrinsic splitting near the K points is very small (~ 1 μeV [21]) due to the mirror symmetry of the graphene sheet in respect to the x-y plane, which leads to a cancellation of nearest-neighbor hopping terms for the K and K' points. The contribution to the intrinsic spin-orbit coupling in a flat graphene sheet is the second-order processes as shown in Fig. 5.9a. In these processes, a $p_z\uparrow$ electron on the left A atom (cyan) can hop onto a $p_x\downarrow$ orbital through the intra-atomic spin-orbit coupling. Then it can hop via the σ-band to the next B atom and further to the sp^2 orbitals of the next A atom. Another spin-flip process induced by the intra-atomic coupling brings it back to an $p_z\uparrow$ state. This process is thus second order in Δ [21], [23]. In contrast, the high curvature of carbon nanotubes breaks the isotropy of the lattice and leads to an effective anisotropic coupling between π-band and σ-band as shown in Fig. 5.9b. In the following, we will focus only on the contribution of curvature in the SOI of CNT.

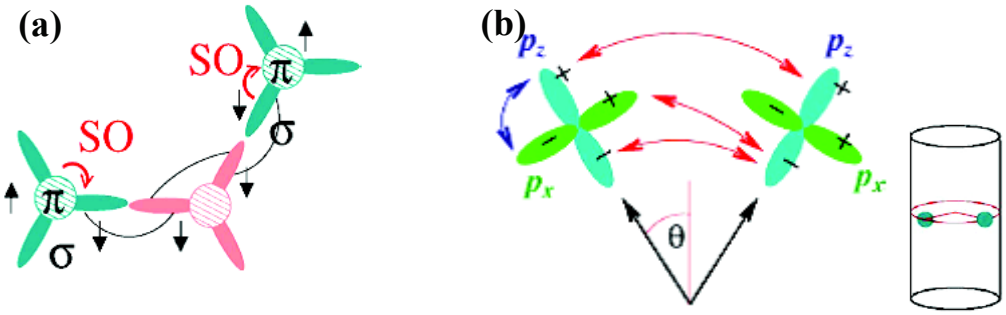

Figure 5.9. (a) Intrinsic SO coupling between two A atoms in graphene: a spin-up electron hops from the p_z orbital onto a spin-down p_x orbital (spin-orbit), then hops to the second nearest neighbor via the σ-band and back onto a spin-up state via spin-orbit coupling. This process is second order in Δ. (b) Additional hoppings allowed by curvature in CNT: a spin up electron on the left p_z orbital hops onto the left p_x orbital (now spin-down) and directly to the right p_z orbital (spin-down). This process is first order in Δ. Adapted from ref. [21].

The SO coupling in CNT has been simply predicted by using the model of Fig. 5.10 [19], [21]. We consider an electron that orbits around the tube circumference and has a spin moment pointing along the CNT axis (Fig. 5.10a). This electron lays on the p_z orbital perpendicular to the nanotube surface. In the rest frame of the electron, the p_z orbital revolves around the spin exactly one time for each rotation (Fig. 5.10b). In the presence of atomic SO coupling ($\Delta_{atom} \approx 8$ meV [16] for an isolated carbon atom), a constant phase accumulates during each rotation. This accumulation is described by a spin-dependent topological flux, $S_{//}\phi_{SO}$ which threads the nanotube cross-section (Fig. 5.10c). The $S_{//}$ value is (+1) or (-1) corresponding to the spin moment in parallel or antiparallel to the nanotube axis.

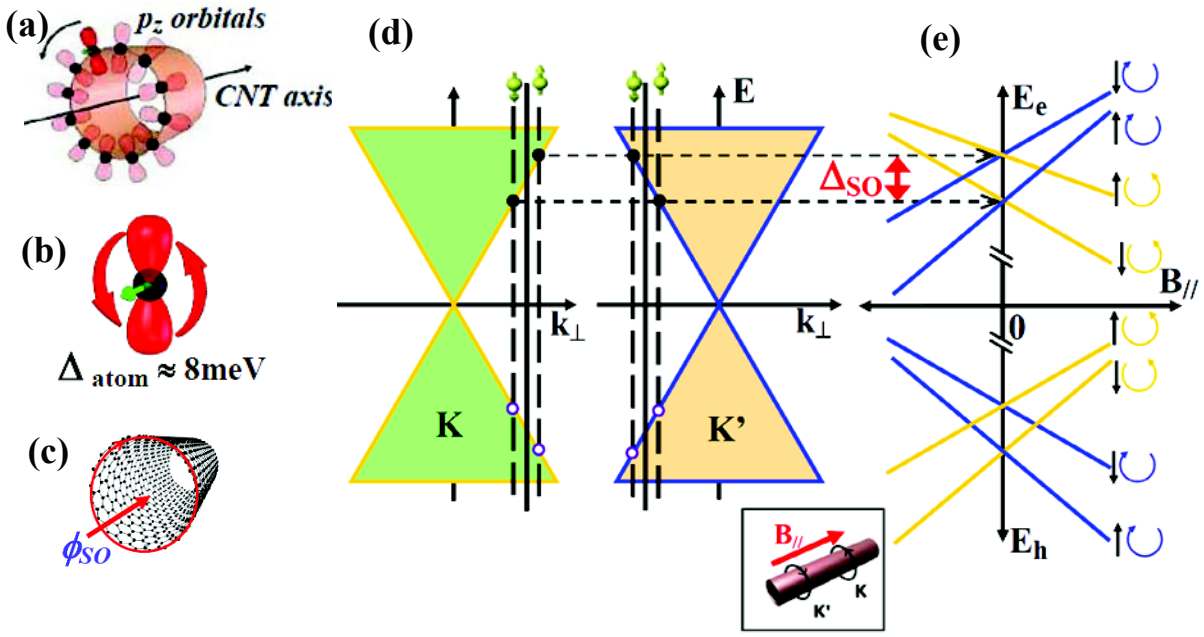

Figure 5.10. Curvature induced SO coupling in carbon nanotube. (a) The circumferential movement of an electron occupying p_z orbital. (b) In the rest frame of electron, the orbital revolves around the spin on time for each complete rotation. (c) The intra-atomic SO coupling Δ_{atom} leads to a phase accumulation during each revolution, and forms a spin-dependent topological flux ϕ_{SO}. (d) Allowed energy states of electrons and holes at $B_{//}$=0 for a small bandgap nanotube with SO coupling. These states are derived from the intersection of Dirac cones (K and K') with spin-dependent quantization lines (dashed lines) different for up and down electron spin moments. (e) Calculated energy levels for electrons and holes as a function of $B_{//}$. The four distinct slopes arise from the orbital and spin Zeeman shifts [14], [16]. Here, K' (CW) and K (CCW) state moves up and down in energy with applied $B_{//}$, respectively (inset). The sign of spin ↑ or ↓ bases on its relative direction with the $B_{//}$.

The spin-dependent topological flux (ϕ_{SO}) has exactly the same effect as the Aharonov-Bohm flux (ϕ_{AB}) created by an external magnetic field. The only differences are that, its sign depends on the spin projection along the tube axis, and it is independent of the nanotube diameter or the shape of the CNT cross-section (thus topological). This flux modifies the quantization condition of the wavefunction around the circumference as:

$$k_\perp \pi d = 2\pi j \quad \rightarrow \quad k_\perp \pi d \pm 2\pi \frac{\phi_{SO}}{\phi_0} = 2\pi j \qquad (5.4)$$

(without SO coupling) (with SO coupling)

where $k_\perp$ is the electron's wave vector in the circumferential direction at K and K' points, d is the tube diameter, j is a integer, and ϕ_o=h/e is the flux quantum. The topological flux mentioned above is given by [16]:

$$\phi_{SO} = \frac{\Delta_{at}}{12\varepsilon_{\pi\sigma}}\left(5 + 3\frac{V_{pp}^{\sigma}}{V_{pp}^{\pi}}\right)\phi_0 \approx 10^{-3}\phi_0 \quad (5.5)$$

in which $\varepsilon_{\pi\sigma}$ is the energy splitting of the π and σ bands in graphene, and V_{pp}^{σ}, V_{pp}^{π} are the hopping elements within these bands.

Due to the presence of the spin dependent topological flux, the allowed values of $k_\perp$ in Eq. 5.4 are modified as shown in Fig. 5.10d. Near each Dirac cones (K and K'), there are two quantization lines for the two spin directions (dashed lines). Comparing to the case without spin-orbit coupling (solid line), the spin-dependent wave-vector shifts $(\pm 2/d)(\phi_{SO}/\phi_0)$ leading to an energy splitting of:

$$|\Delta_{SO,1}| = 2\hbar v_F\left(\frac{2}{d}\right)\left(\frac{\phi_{SO}}{\phi_0}\right) \approx \frac{1.6}{d}\ (meV.nm^{-1}) \quad (5.6)$$

The resulting energy spectrum in Fig. 5.10e shows breaking of the four-fold degeneracy of CNT into two doublets. The value of $\Delta_{SO,1}$ is inversely proportional to nanotube diameter, and thus very small in flat graphene (d→∞).

In addition to the SO coupling produced by the geometric phase ($\Delta_{SO,1}$), an additional term $\Delta_{SO,0}$ was subsequently identified [24–26] that is also created by the curvature of the graphene sheet and can be understood as an effective valley-dependent Zeeman term [14]. The two coupling constants $\Delta_{SO,0}$ and $\Delta_{SO,1}$ depend on the type of the tube, both are inversely proportional to the diameter d. However, while the $\Delta_{SO,0}$ depends on the chiral angle as $\Delta_{SO,0} \propto \cos(3\theta)$, the $\Delta_{SO,1}$ does not depend on θ [27].

The combination of these two terms explains the electron-hole anisotropy of SO coupling strength observed in experiment [16] because the total spin-orbit coupling for electrons and holes is:

$$\Delta_{SO}^{e} = 2(\Delta_{SO,0} - \Delta_{SO,1}) \text{ and } \Delta_{SO}^{h} = -2(\Delta_{SO,0} + \Delta_{SO,1}) \quad (5.7)$$

in which the sign conventions are assumed as in ref. [28].

The SO coupling strength in carbon nanotubes thus depends on the chirality, which decides both the diameter (the curvature) and the wrapping angle leading to the difference in π-σ hybridization as shown in Fig. 5.9b. Despite the four possibilities for the signs of Δ_{SO}^{e} and Δ_{SO}^{h} , only one case of $\Delta_{SO}^{e} > 0$ and $\Delta_{SO}^{h} > 0$ has been observed in experiments [14], [16] until now.

5.6. Kondo effects

In previous sections, we considered the transport through a quantum dot that is weakly coupled to the source and the drain electrodes. The transport in this case is first-order with sequential tunneling, and the number of electrons on the dot is kept constant due to Coulomb blockade. However, when the electrical contacts are sufficiently transparent, so that the resistance of the tunnel barriers becomes comparable to the resistance quantum h/e^2, higher-order tunneling processes have to be taken into account. These processes lead to quantum fluctuations in the number of electrons in the dot, even when it is in the regime of Coulomb blockade. Figure 5.11 shows examples of higher-order tunneling process through a quantum dot, which involves a simultaneous passage of two electrons.

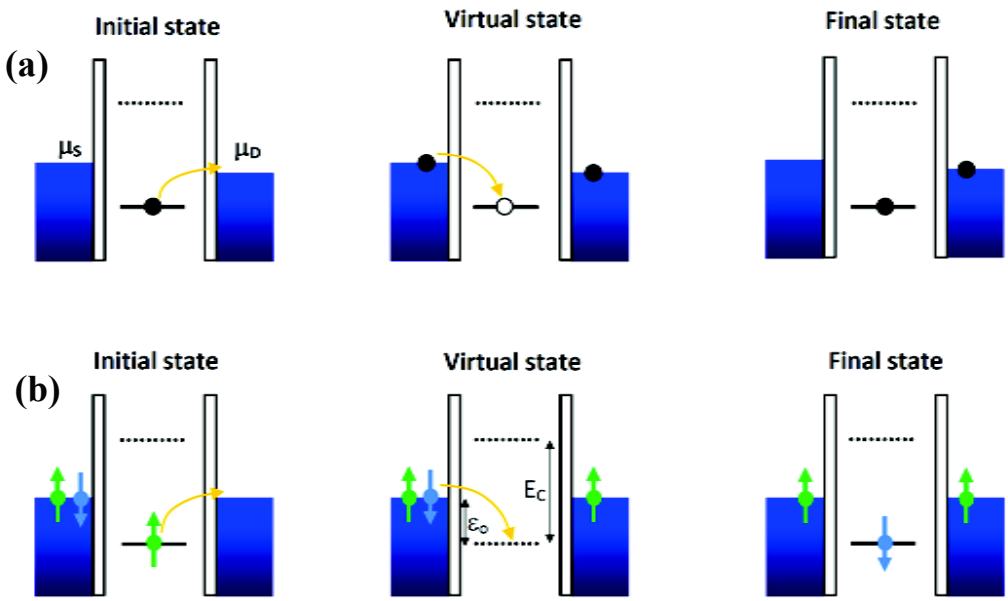

Figure 5.11. Higher-order tunneling events that overcome Coulomb blockade. (a) Elastic cotunneling in general. There are N electrons on the dot. The Nth electron jumping from the dot to the drain will be immediately replaced by an electron from the source. At a small bias voltage, such processes lead to the flow of a current through the dot. (b) Elastic cotunneling with spin flip. The spin-up electron jumping out of the dot is immediately replaced by a spin-down electron. Many such higher-order spin flip events together build up a spin singlet state consisting of electron spins in the reservoirs and the spin on the dot. The spin on the dot is thus screened [8].

Figure 5.11a is the general case of elastic cotunneling process. Initially, there is no discrete level in the dot that is relatively aligned to the Fermi levels of the electrodes. The energy conservation forbids the electron to change its state because this costs an energy of E_c. Nevertheless, if the contacts are sufficiently transparent, the electron initially inside the dot can come out to the drain and temporarily leaves a virtual state in the dot, which is forbidden in classical physics. This process is only allowed by Heisenberg's energy-time uncertainty principle, so that another electron from the source electrode tunnels to the dot and immediately replaces the initial one. The system then finds the same energy as the initial state, but an electron was transported through the dot. This is a coherent process and known as ‘elastic’ cotunneling in which the energy state of the dot does not change. This is distinguished from the "inelastic" cotunneling process where the originally released electron is replaced by another electron occupying a different discrete energy level, and the dot is left in an excited state.

If the spin of the dot is also taken into account, the spin flip elastic cotunneling process can take place (Fig. 5.11b). Initially, the dot has an overall spin 'up' caused by the spin of an individual electron located at the highest energy level. After passing a virtual intermediate state, a spin 'down' electron can tunnel in to replace. The spin of the dot is flipped at each transition and an electron is added coherently. The spins of electrons of contact electrodes and the spin of the dot are highly correlated, which forms a singlet spin state. The localized spin in the dot is completely screened by the spins of electrons in metallic reservoirs. This state is the origin of the Kondo effect in quantum dots and leads to the appearance of a narrow peak in the density of states at the Fermi level of the electrodes [29]. Unlike the Coulomb blockade regime that reveals the behavior of electrons confined only in the dot, the Kondo effect also incorporates consistently the effect of delocalized electrons in the electrodes.

The Kondo effect was initially observed in noble metals containing a low concentration of magnetic impurities (e.g. Co in Au). Unlike the normal behavior of a pure metal at low temperatures, it was observed since the 1930s [30] that below a certain temperature (typically about 10 K), the resistance of the doped metals increases logarithmically (Fig. 5.12a). Since this effect appears only in the presence of magnetic impurities [31], it must necessarily be related to the electron spin. This anomalous behavior was not understood until 1964, that Jun Kondo explained the effect as a screening of the magnetic spins by the spins of free electrons of the host metal [32]. The magnetic moment of the impurity interacts with the spin of the conduction electrons by an anti-ferromagnetic coupling, and results in a polarization of the electrons in the vicinity of the magnetic impurity. The screening forms a macroscopic coherent state called the 'Kondo cloud' (Fig. 5.12b). The Kondo cloud is a much larger scatterer than a single impurity site, and hence leads in an increased resistance. The temperature below which this phenomenon occurs is called the 'Kondo temperature' T_K. This temperature reflects the binding energy of the singlet state leading to the Kondo effect. Above the Kondo temperature, Kondo clouds cannot form since they are not energetically favorable.

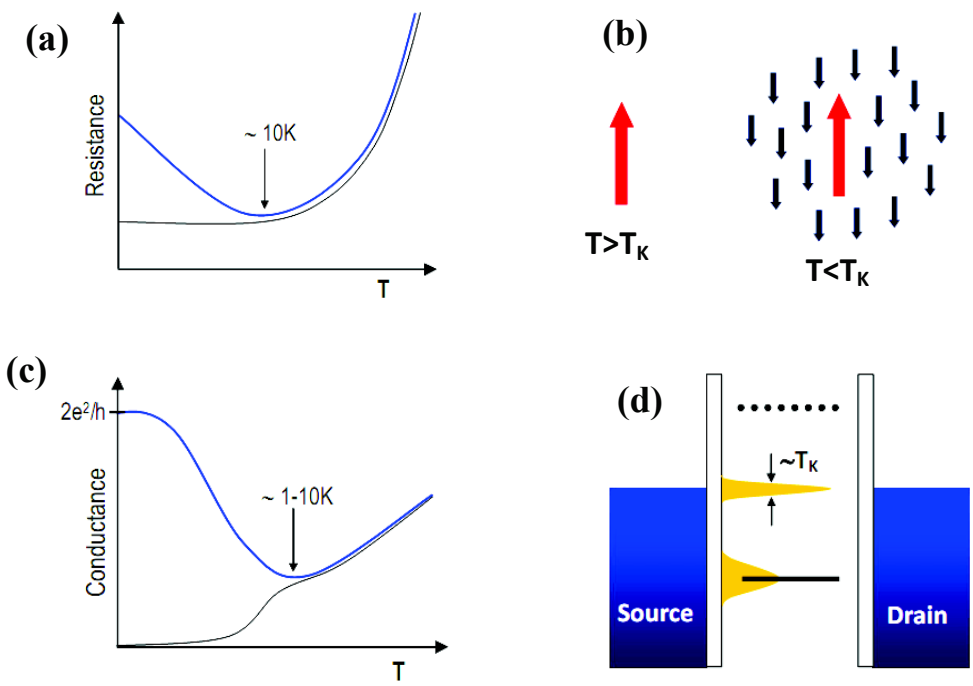

Figure 5.12. Kondo effect in doped metal (top) and in QD (bottom). (a) Evolution of resistance of bulk metals with temperature. For a pure metal (black curve), it saturates at low temperature due to the diffraction on static defects in the material. However, for a metal containing a small fraction of magnetic impurities (e.g. Co in Au, blue curve), the resistance increases at T< 10 K due to the Kondo effect. (b) For T> T_K, the magnetic impurity is decoupled from the conduction electrons. If T <T_K, conduction electrons and the magnetic impurity interact coherently and form a Kondo cloud. (c) For a quantum dot, the conductance decreases at lower temperatures due to Coulomb blockade (black curve). If the dot contains a magnetic impurity (blue curve), the conductance will increase at temperatures below a certain temperature due to Kondo effect. (d) A resonance with a width of k_BT_K develops in the density of states of the quantum dot at the Fermi level of the electrodes due to the Kondo effect. This resonance leads to the appearance of the conductance at zero bias voltage in current-voltage characteristics of the quantum dot [29].

The Kondo effect was predicted to occur in QDs in 1988 [33], [34], and then experimentally observed in semiconductor heterostructures [35], carbon nanotubes [36], individual molecules [37], and semiconductor nanowires [38] QDs. The Kondo effect in quantum dots has a very similar origin to that of doped metals. The main difference is that it causes an increase of conductance up to maximum value of $2e^2/h$ [34], instead of resistance (Fig. 5.12c). The Kondo effect happens when the quantum dot is strongly coupled to the two electrodes, which promotes the passage of electrons from source to drain. Because of the

Kondo resonance, the transmission probability of an electron through the quantum dot is increased at temperatures below T_K. The ground state of the system is a spin singlet state and the entire process of cotunneling leads to the appearance of a conductance peak at the Fermi level, called Kondo resonance (Fig. 5.12d). Unlike Kondo effect appearing in bulk materials containing many atoms, the one of QD comes from the localized spin of the electron that behaves as a single 'magnetic impurity'.

The Kondo temperature, T_K, corresponds to the binding energy of the Kondo singlet state, and is expressed in terms of the dot parameters [29]:

$$T_K = \frac{\sqrt{h\Gamma E_C}}{2k_B} e^{\frac{\pi\varepsilon_O(\varepsilon_O + E_C)}{h\Gamma E_C}} \tag{5.8}$$

where Γ is the tunneling rate to and from the dot, ε_o is the energy level on the dot relative to the Fermi energy of the reservoirs, and E_C is the charging energy. The great advantage of using quantum dots to study the Kondo effect is that their parameters can be tuned *in situ* [29], [33], [34].

If there is an odd number of electrons on the dot, the total spin *S* is non zero (S=1/2 in the simplest case), and the Kondo effect occurs due to the singlet spin state formation. When the electron number on the dot is even, all these electrons couple in pairs giving a zero net spin S=0, and no zero-bias Kondo effect is observed. This 'even-odd asymmetry' in Kondo effect is shown in Fig. 5.13.

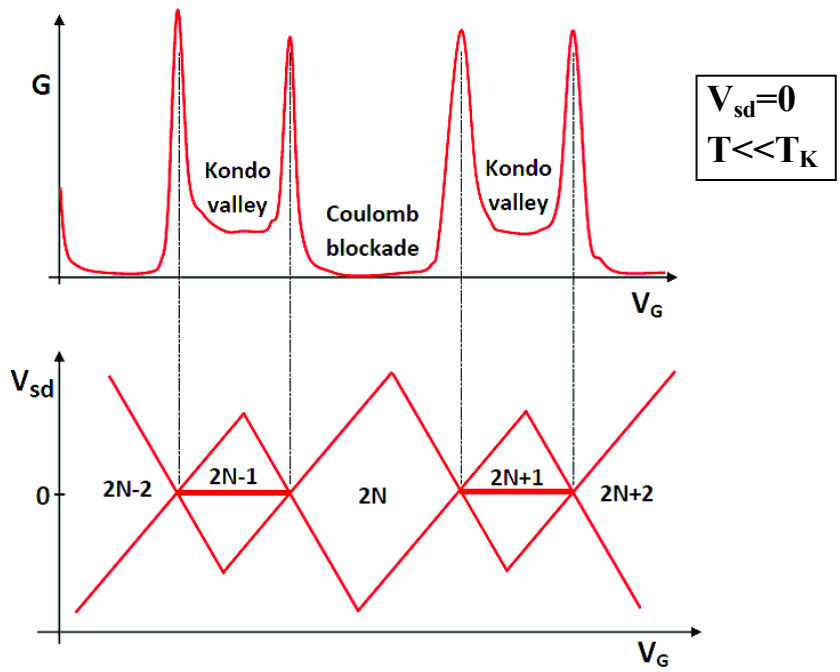

Figure 5.13. Conductance as a function of V_{SD} and V_g of a quantum dot in Kondo regime. The Kondo ridges appear at every second diamond including an odd number of electrons on the dot.

SU(4) Kondo effect

The Kondo effect in CNT QD was first observed in 2000 [36] and since then, it is one of the most fascinating and extensively studied subjects in quantum physics. The Kondo effect in CNT has all familiar features of Kondo effect in other kinds of QDs, plus the unique properties of nanotubes. The four-fold degeneracy of the nanotube plays a very important role in the cotunneling of electrons. In addition to the spin ½ Kondo effect due to spin flip (Fig. 5.14a), orbital Kondo effect was also observed in the CNT QD [39]. In this process, the electron tunneling into the dot can occupy CW or CCW orbital alternately. In other word, the orbital of the QD is flipped and screened as illustrated in Fig. 5.14b. The (+) and (–) signs in this figure correspond to CW and CCW orbital, respectively.

Moreover, since both the spin and orbital of electron can be flipped and lead to Kondo effect during the electron transport, their degrees of freedom are totally entangled. This leads to the highly symmetry SU(4) Kondo effect, with a much higher Kondo temperature, $T_K^{SU(4)}$, than that of spin ½ Kondo, $T_K^{SU(2)}$[39], [40]. The formation of SU(4) Kondo effect in CNT QD is shown in Fig. 5.14c.

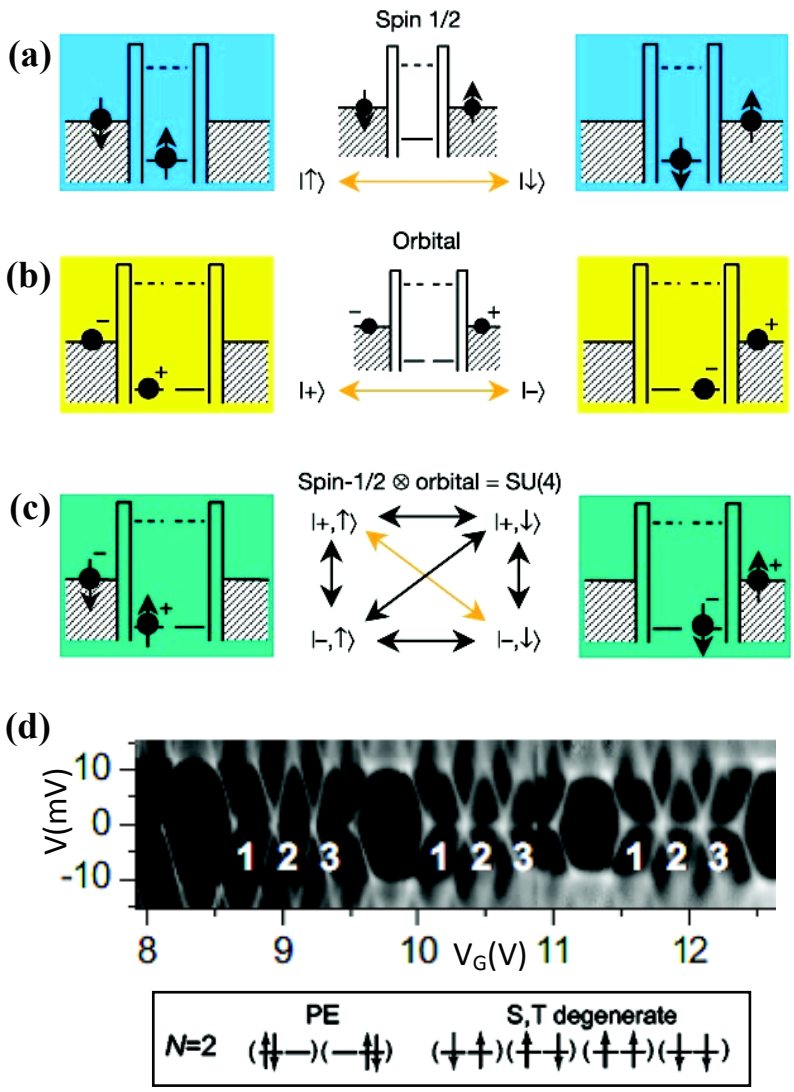

Figure 5.14. Spin (a), orbital (b) and SU(4) (c) Kondo effect in a CNT QD. The left, middle and right panels in a-c represent the initial, intermediate virtual and final ground states, respectively [39]. (d) A conductance map of the CNT QD from ref. [41] showing SU(4) Kondo effect.

In SU(4) Kondo effect, the Kondo ridges appear both at the odd numbers of electron (N=1,3) and also at haft-filled diamonds (N=2) (Fig. 5.14d). At N=2, there are six possibilities of electron filling: two states of paired-electrons (PE) and other four of one singlet plus three triplet (see inset). The Kondo effect at haft-filling is supposed due to the degeneracy of singlet and triplet states, which is effective by the entangled processes illustrated in Fig. 5.14c. In other word, the large number of degenerate states caused by SU(4) Kondo energetically allows the second-order elastic spin-flip processes to occur. However, it is worth noting that the SU(4) Kondo effect described above can only be observed when the

symmetry of four-fold degeneracy of CNT is well preserved. In the presence of spin-orbit coupling, the condition of $k_B T_K^{(SU4)} \geq \Delta_{SO}$ must be satisfied for its appearance [42].

5.7. Conclusion

In this chapter, we presented the main electronic properties of carbon nanotube quantum dots. The CNT QD, owning large charging energy, high energy level spacing and simple energy spectrum, is a very attractive system for studying quantum physics. The unique band structure of CNT leads to the four-fold degeneracy of its energy level, which is revealed by four electron shell filling and especially highly symmetry SU(4) Kondo effect. Moreover, we also described the effect of spin-orbit coupling on the energy structure of the CNT, which is very useful in interpreting and understanding the spectra of transport measurements.

References

[1] A. N. Pasupathy, J. I. Goldsmith, C. Chang, Y. Yaish, J. R. Petta, M. Rinkoski, J. P. Sethna, P. L. McEuen, and D. C. Ralph, "Coulomb blockade and the Kondo effect in single-atom transistors," *Nature*, vol. 417, no. 6890, pp. 722–725, Jun. 2002.

[2] D. C. Ralph, C. T. Black, and M. Tinkham, "Gate-Voltage Studies of Discrete Electronic States in Aluminum Nanoparticles," *Phys. Rev. Lett.*, vol. 78, no. 21, pp. 4087–4090, May 1997.

[3] S. Tarucha, D. G. Austing, Y. Tokura, W. G. van der Wiel, and L. P. Kouwenhoven, "Direct Coulomb and Exchange Interaction in Artificial Atoms," *Phys. Rev. Lett.*, vol. 84, no. 11, pp. 2485–2488, Mar. 2000.

[4] C. Pasquier, U. Meirav, F. I. B. Williams, D. C. Glattli, Y. Jin, and B. Etienne, "Quantum limitation on Coulomb blockade observed in a 2D electron system," *Phys. Rev. Lett.*, vol. 70, no. 1, pp. 69–72, Jan. 1993.

[5] S. De Franceschi, J. A. Van Dam, E. P. a. M. Bakkers, L. F. Feiner, L. Gurevich, and L. P. Kouwenhoven, "Single-electron tunneling in InP nanowires," *Applied physics letters*, vol. 83, no. 2, pp. 344–346.

[6] S. J. Tans, M. H. Devoret, H. Dai, A. Thess, R. E. Smalley, L. J. Geerligs, and C. Dekker, "Individual single-wall carbon nanotubes as quantum wires," *, Published online: 03 April 1997; | doi:10.1038/386474a0*, vol. 386, no. 6624, pp. 474–477, Apr. 1997.

[7] L. P. Kouwenhoven, C. M. Marcus, P. L. McEuen, S. Tarucha, R. M. Westervelt, and N. S. Wingreen, "Electron transport in quantum dots," in *Mesoscopic Electron Transport*, Kluwer, 1997, pp. 105–214.

[8] J.-P. CLEUZIOU, "Propriétés de transport électronique de nanotubes de carbone: des nanotubes hybrides au nano-SQUID," Toulouse, 2007.

[9] S. Sapmaz, P. Jarillo-Herrero, J. Kong, C. Dekker, L. P. Kouwenhoven, and H. S. J. van der Zant, "Electronic excitation spectrum of metallic carbon nanotubes," *Phys. Rev. B*, vol. 71, no. 15, p. 153402, Apr. 2005.

[10] D. H. Cobden and J. Nygård, "Shell Filling in Closed Single-Wall Carbon Nanotube Quantum Dots," *Phys. Rev. Lett.*, vol. 89, no. 4, p. 046803, Jul. 2002.

[11] S. Sapmaz, P. Jarillo-Herrero, L. P. Kouwenhoven, and H. S. J. van der Zant, "Quantum dots in carbon nanotubes," *Semiconductor Science and Technology*, vol. 21, no. 11, pp. S52–S63, Nov. 2006.

[12] A. Pályi and G. Burkard, "Spin-valley blockade in carbon nanotube double quantum dots," *Phys. Rev. B*, vol. 82, no. 15, p. 155424, Oct. 2010.

[13] G. Kiršanskas, J. Paaske, and K. Flensberg, "Cotunneling renormalization in carbon nanotube quantum dots," *Phys. Rev. B*, vol. 86, no. 7, p. 075452, Aug. 2012.

[14] T. S. Jespersen, K. Grove-Rasmussen, J. Paaske, K. Muraki, T. Fujisawa, J. Nygård, and K. Flensberg, "Gate-dependent spin-orbit coupling in multielectron carbon nanotubes," *Nature Physics*, vol. 7, no. 4, pp. 348–353, Jan. 2011.

[15] P. Jarillo-Herrero, J. Kong, H. S. J. van der Zant, C. Dekker, L. P. Kouwenhoven, and S. De Franceschi, "Electronic Transport Spectroscopy of Carbon Nanotubes in a Magnetic Field," *Phys. Rev. Lett.*, vol. 94, no. 15, p. 156802, Apr. 2005.

[16] F. Kuemmeth, S. Ilani, D. C. Ralph, and P. L. McEuen, "Coupling of spin and orbital motion of electrons in carbon nanotubes," *Nature*, vol. 452, no. 7186, pp. 448–452, Mar. 2008.

[17] Y. Oreg, K. Byczuk, and B. I. Halperin, "Spin Configurations of a Carbon Nanotube in a Nonuniform External Potential," *Phys. Rev. Lett.*, vol. 85, no. 2, pp. 365–368, Jul. 2000.

[18] W. Liang, M. Bockrath, and H. Park, "Shell Filling and Exchange Coupling in Metallic Single-Walled Carbon Nanotubes," *Phys. Rev. Lett.*, vol. 88, no. 12, p. 126801, Mar. 2002.

[19] T. Ando, "Spin-Orbit Interaction in Carbon Nanotubes," *J. Phys. Soc. Jpn.*, vol. 69, pp. 1757–1763, 2000.

[20] "Spin–orbit interaction." [Online]. Available: http://en.wikipedia.org/wiki/Spin%E2%80%93orbit_interaction.

[21] D. Huertas-Hernando, F. Guinea, and A. Brataas, "Spin-orbit coupling in curved graphene, fullerenes, nanotubes, and nanotube caps," *Phys. Rev. B*, vol. 74, no. 15, p. 155426, Oct. 2006.

[22] A. D. Martino, R. Egger, F. Murphy-Armando, and K. Hallberg, "Spin–orbit coupling and electron spin resonance for interacting electrons in carbon nanotubes," *Journal of Physics: Condensed Matter*, vol. 16, no. 17, pp. S1437–S1452, May 2004.

[23] F. Kuemmeth, "SPIN STATES AND SPIN-ORBIT COUPLING IN NANOSTRUCTURES," Cornell, 2008.

[24] W. Izumida, K. Sato, and R. Saito, "Spin–Orbit Interaction in Single Wall Carbon Nanotubes: Symmetry Adapted Tight-Binding Calculation and Effective Model Analysis," *Journal of the Physical Society of Japan*, vol. 78, no. 7, p. 074707, Jun. 2009.

[25] J.-S. Jeong and H.-W. Lee, "Curvature-enhanced spin-orbit coupling in a carbon nanotube," *Phys. Rev. B*, vol. 80, no. 7, p. 075409, Aug. 2009.

[26] L. Chico, M. P. López-Sancho, and M. C. Muñoz, "Curvature-induced anisotropic spin-orbit splitting in carbon nanotubes," *Phys. Rev. B*, vol. 79, no. 23, p. 235423, Jun. 2009.

[27] H. O. H. Churchill, "Quantum Dots in Gated Nanowires and Nanotubes," Harvard, 2012.

[28] S. Weiss, E. I. Rashba, F. Kuemmeth, H. O. H. Churchill, and K. Flensberg, "Spin-orbit effects in carbon-nanotube double quantum dots," *Phys. Rev. B*, vol. 82, no. 16, p. 165427, Oct. 2010.

[29] L. Kouwenhoven and L. Glazman, "Revival of the Kondo effect," *Physics World*, vol. 14, no. 1, pp. 33–38, 2001.

[30] W. J. de Haas, J. de Boer, and G. J. van dën Berg, "The electrical resistance of gold, copper and lead at low temperatures," *Physica*, vol. 1, no. 7–12, pp. 1115–1124, May 1934.

[31] M. P. Sarachik, E. Corenzwit, and L. D. Longinotti, "Resistivity of Mo-Nb and Mo-Re Alloys Containing 1% Fe," *Phys. Rev.*, vol. 135, no. 4A, pp. A1041–A1045, 1964.

[32] J. Kondo, "Resistance Minimum in Dilute Magnetic Alloys," *Progress of Theoretical Physics*, vol. 32, no. 1, pp. 37–49, 1964.

[33] L. I. Glazman and M. É. Raikh, "Resonant Kondo transparency of a barrier with quasilocal impurity states," *Soviet Journal of Experimental and Theoretical Physics Letters*, vol. 47, p. 452, Apr. 1988.

[34] T. K. Ng and P. A. Lee, "On-Site Coulomb Repulsion and Resonant Tunneling," *Phys. Rev. Lett.*, vol. 61, no. 15, pp. 1768–1771, Oct. 1988.

[35] D. Goldhaber-Gordon, H. Shtrikman, D. Mahalu, D. Abusch-Magder, U. Meirav, and M. A. Kastner, "Kondo effect in a single-electron transistor," *Nature*, vol. 391, no. 6663, pp. 156–159, Jan. 1998.

[36] J. Nygard, D. H. Cobden, and P. E. Lindelof, "Kondo physics in carbon nanotubes," *Nature*, vol. 408, no. 6810, pp. 342–346, Nov. 2000.

[37] J. Park, A. N. Pasupathy, J. I. Goldsmith, C. Chang, Y. Yaish, J. R. Petta, M. Rinkoski, J. P. Sethna, H. D. Abruna, P. L. McEuen, and D. C. Ralph, "Coulomb blockade and the Kondo effect in single-atom transistors," *Nature*, vol. 417, no. 6890, pp. 722–725, Jun. 2002.

[38] T. S. Jespersen, M. Aagesen, C. Sørensen, P. E. Lindelof, and J. Nygård, "Kondo physics in tunable semiconductor nanowire quantum dots," *Phys. Rev. B*, vol. 74, no. 23, p. 233304, Dec. 2006.

[39] P. Jarillo-Herrero, J. Kong, H. S. J. van der Zant, C. Dekker, L. P. Kouwenhoven, and S. D. Franceschi, "Orbital Kondo effect in carbon nanotubes," *Nature*, vol. 434, no. 7032, pp. 484–488, Mar. 2005.

[40] M.-S. Choi, R. López, and R. Aguado, "SU(4) Kondo Effect in Carbon Nanotubes," *Phys. Rev. Lett.*, vol. 95, no. 6, p. 067204, 2005.

[41] A. Makarovski, A. Zhukov, J. Liu, and G. Finkelstein, "SU(2) and SU(4) Kondo effects in carbon nanotube quantum dots," *Phys. Rev. B*, vol. 75, no. 24, p. 241407, Jun. 2007.

[42] M. R. Galpin, F. W. Jayatilaka, D. E. Logan, and F. B. Anders, "Interplay between Kondo physics and spin-orbit coupling in carbon nanotube quantum dots," *Phys. Rev. B*, vol. 81, no. 7, Feb. 2010.

Chapter 6. Ultraclean carbon nanotube quantum dot with a strong negative spin-orbit coupling in the Kondo regime

In this chapter, we study an ultraclean carbon nanotube quantum dot in the few-electron regime which exhibits spin-orbit coupling and the SU(4) Kondo effect. When both phenomena are comparable in strength, the spin-orbit interaction lifts the four-fold Kondo symmetry and quenches the zero bias Kondo resonance at half filling. The electronic level spectra of the first electrons are investigated using inelastic cotunneling spectroscopy in an axial magnetic field. A strong negative spin-orbit coupling is found for the conduction band as well as a pure orbital level degeneracy in the two electron regime.

6.1. Introduction

The interplay between electron orbital and spin degrees of freedom in nanostructures is currently a subject of intense studies. In this context, carbon nanotubes (CNTs) have attracted considerable interest in the past years due to their unique electronic properties. The progress in designing and processing of ultraclean CNT quantum dots have enabled to resolve the CNT energy spectrum with a high resolution in the first and few-electron regimes. Single-electron tunneling spectroscopy on these devices has shown the important role of curvature induced spin-orbit interaction (SOI), which splits the four-fold degenerate levels into two Kramers doublets ($K\uparrow$, $K'\downarrow$) and ($K\downarrow$, $K'\uparrow$) with entangled spin and orbital degrees of freedom [1] separated by an energy gap Δ_{SO}. This result was later confirmed in the many electron regime, including a significant disorder induced valley mixing $\Delta_{KK'}$ [2]. The role of the SOI and disorder on the nanotube energy spectrum can be illustrated in Fig. 6.1, which shows the calculated single-particle energy spectrum as a function of magnetic field $B_{\perp}$ and $B_{//}$ to the tube axis [2]. Depending on the CNT type, electron filling and degree of disorder, all the four situations can occur. For the case of ultraclean CNT with $\Delta_{SO} > 0$, the 1e energy spectrum should be as Fig. 6.1c.

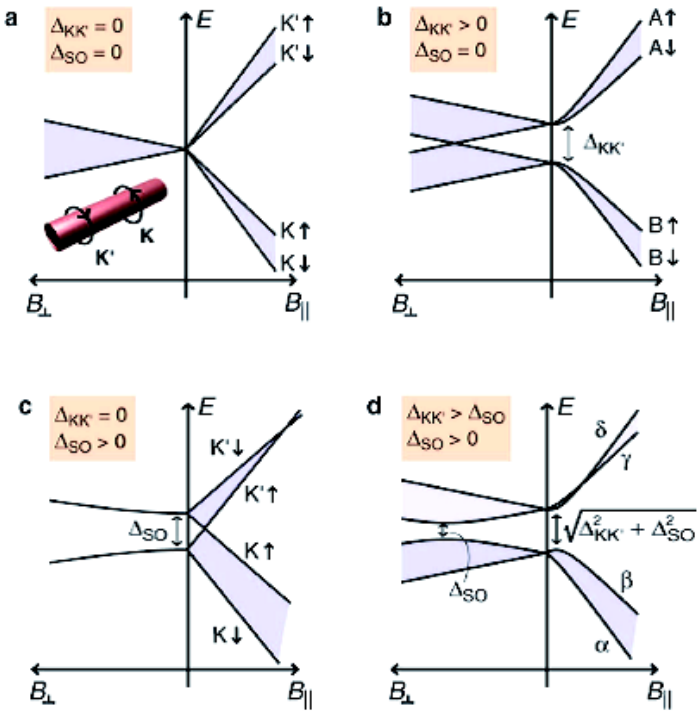

Figure 6.1. Calculated single-particle energy spectrum as a function of magnetic field applied perpendicular ($B_\perp$) and parallel ($B_{//}$) to the CNT axis. (a) Perfect four-fold degeneracy. (b) With the presence of $\Delta_{KK'} > 0$, (c) $\Delta_{SO} > 0$, and (d) both $\Delta_{KK'}$ and $\Delta_{SO} > 0$. Adapted from ref. [2].

On the other hand, it is well established that quantum dots with sufficiently strong tunnel couplings to the metallic leads exhibit rich Kondo physics. Particularly in a CNT having the four-fold degeneracy, the electronic correlations tend to mix the spin and isospin degrees of freedom, thereby forming a highly entangled SU(4) Kondo ground state [3] (assuming conservation of orbital quantum numbers during the tunneling processes) with enhanced Kondo temperature T_K. When SOI is taken into account in CNT energy spectrum, a crossover from SU(4) ($k_B T_K >> \Delta_{SO}$) to SU(2) Kondo effects ($k_B T_K \approx \Delta_{SO}$) at zero magnetic field is expected [4] due to the mutual interplay between SOI and Kondo correlations. While plausible deviations of SU(4) Kondo physics related to the SOI have been discussed in connection to previous experiments [4], the study of the Kondo effect in CNT quantum dots with SOI split energy spectrum is still missing.

In this work, we have studied a (ultraclean) small band gap semiconducting CNT quantum dot, which shows a mutual competition between Kondo physics and the SOI. The

CNT spectrum is investigated by inelastic cotunneling spectroscopy measurements in the weak Kondo regime for the first electron quartet of the conduction band ($k_B T_K \approx \Delta_{SO}$).

6.2. Kondo effect of ultraclean CNT quantum dot with SOI splitting

6.2.1. Conductance at zero magnetic field

Our quantum dot is based on a CNT *in situ* grown on top of predefined source (S) and drain (D) Pt metal contacts (Fig. 6.2a). The CNT is suspended over two independent gates, a Pt metal local gate (LG) and a substrate back gate (BG) as described in chapter 4. The chemical potential of the CNT single quantum dot can be shifted by applying a voltage on each gate, which is depicted in the stability diagram of Fig. 6.2b. All the measurements presented in the rest of this chapter are recorded at a fixed $V_{BG} = 0$ (the white dashed line).

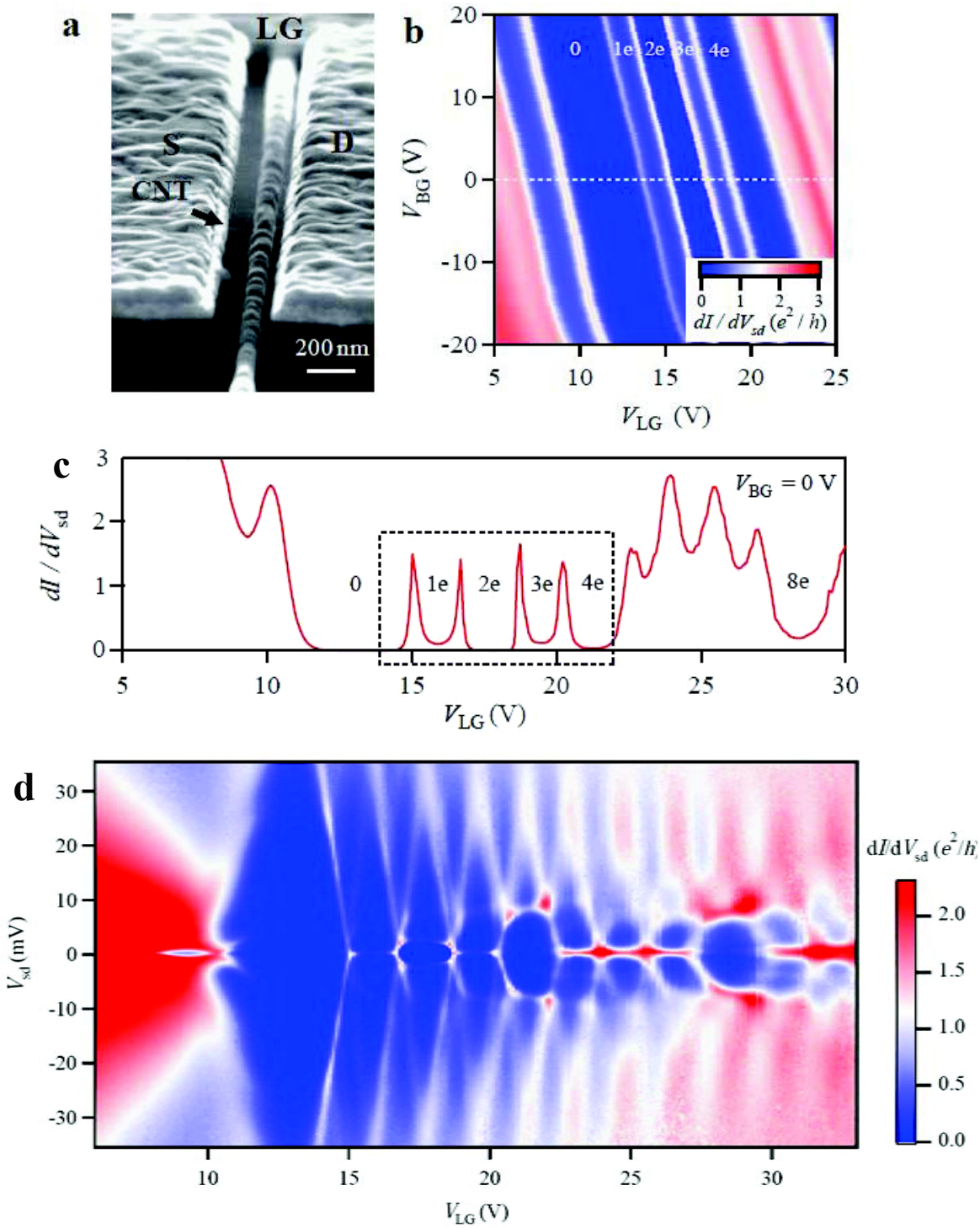

Figure 6.2. (a) Scanning electron microscopy of a nanotube device similar to the one used in the measurements. (b) Color scale representation of the differential conductance dI/dV_{SD} measured at zero bias, as a function of the local gate voltage V_{LG} and back gate voltage V_{BG}. Numbers indicate the charge occupation of the nanotube quantum dot. (c) dI/dV_{SD} trace as a function of V_{LG} at zero bias and $V_{BG} = 0$. (d) Map of dI/dV_{SD} as a function of V_{LG} and V_{SD}. The SU(4) Kondo symmetry is broken in the first electron shell, but it still exists

in the second shell.

When a local gate voltage is applied, electrons are sequentially added to the CNT quantum dot as shown in Fig. 6.2c. In the CNT conduction band, G (dI/dV_{SD}) displays a series of Coulomb peaks which are connected by Coulomb blockade valleys and Kondo ridges at zero bias. The shells of four electrons are clearly observed in this device, and increase of V_{LG} value leads to enhancement of Kondo temperature. While the second shell (N = 5e-8e) displays the SU(4) Kondo symmetry (with a pronounced conductance enhancement at half filling), this symmetry is broken in the first quartet which shows the usual SU(2) Kondo symmetry (enhancement of G only for an odd number of electrons). The map of linear conductance as a function of V_{LG} and V_{SD} is shown in Fig. 6.2d, which gives estimated values of the charging energy $E_C \approx 30$ meV and band gap of the nanotube $E_g \approx 30$ meV.

In our study, we focus on the first four electron states which are further depicted in the high resolution charge stability diagram in Fig. 6.3. At zero bias, Kondo ridges are visible for N = 1e and N = 3e together with the nearby excitations at $|eV_{SD}| \approx$ 0.34 meV. These anomalous behaviors of the electrical transport are the signature of SO coupling. It has been predicted in ref. [4] that, the Kondo ridge at N=2e is destroyed when $\Delta_{SO} \approx k_B T_K$. This will be studied in details as follow.

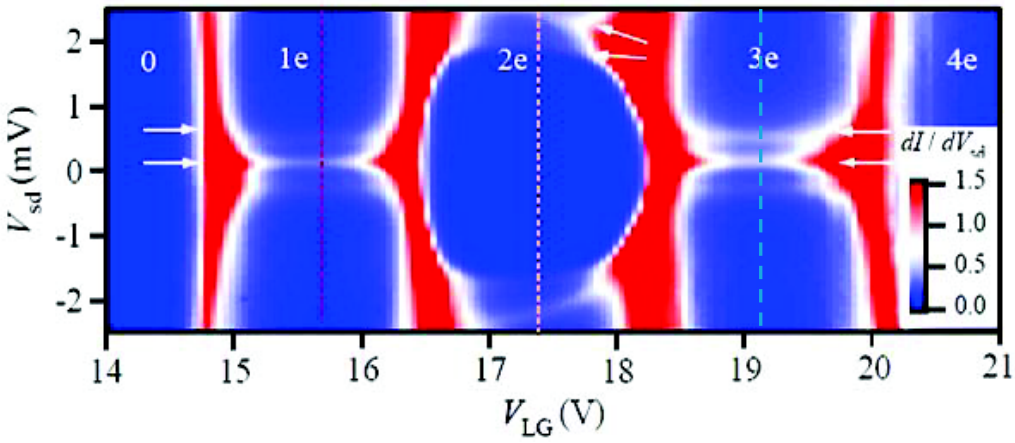

Figure 6.3. Map of dI/dV_{SD} as a function of V_{SD} and V_{LG} at $V_{BG} = 0$ corresponding to the consecutive addition of the first four electrons to the dot in the Kondo regime.

6.2.2. Evolution of Kondo ridges as a function of applied magnetic field

A powerful way to probe the SO coupling in CNT is to confine the carriers in a quantum dot and apply a magnetic field $B_{//}$ parallel to the tube axis. The confinement creates bound states and the field interrogates their nature by coupling independently to their spin and orbital moments [4–6]. The evolution of the Kondo ridges and cotunneling features with the magnetic field can be best traced in Figs. 6.4, 6.5 and 6.7. The conductance is measured as a function of V_{SD} and $B_{//}$ in the center of the three valleys of N = 1e to 3e (the dashed lines in Fig. 6.3).

N=1e

Figure 6.4 is the spectra of one electron on the quantum dot. The applied magnetic field along the CNT axis lifts the spectrum degeneracies with g_s and g_{orb}, the spin and orbital Zeeman g factors, respectively ($g_{orb} >> g_s$) [7]. In this spectrum, two main transitions with significantly different $dV_{SD}/dB_{//}$ slopes (denoted as α and β in Fig. 6.4a) are well visible. It is interesting that the β energy decreases slowly as $B_{//}$ increases in such a way that the involved ground and excited states cross at $B_{spin} \approx 2.5$ T. These splittings are also presented differently in the V_{LG}-V_{SD} maps of conductance (Fig. 6.4c-e), which show an enhanced conductance due to elastic cotunneling process (V_{SD}=0) at finite $B_{//}$. The zero field splitting and the observed level degeneracy at finite $B_{//}$ are compatible with the energy level diagram in Fig. 6.4b, which includes a negative spin-orbit constant ($\Delta_{SO} < 0$). This spin-orbit coupling energy splits the level spectrum in two doublets ($K\downarrow$, $K'\uparrow$) and ($K\uparrow$, $K'\downarrow$). In the diagram, α and β corresponds respectively to the inter- and intra-orbital spin flip cotunneling processes. The average slopes $|dV_{SD}/dB_{//}|$ of α and β give respectively the g-factors: $g_s \approx 2.5$, $g_{orb} \approx 20$ [7], and the spin-orbit splitting $|\Delta_{SO}| \approx 0.34 \pm 0.04$ meV (extracted from Fig. 6.3). The third transition δ is not resolved here probably due to the level broadening. The negative spin-orbit coupling is further confirmed by a level spectroscopy of the third electron charge state, which does not exhibit level crossing at finite magnetic field.

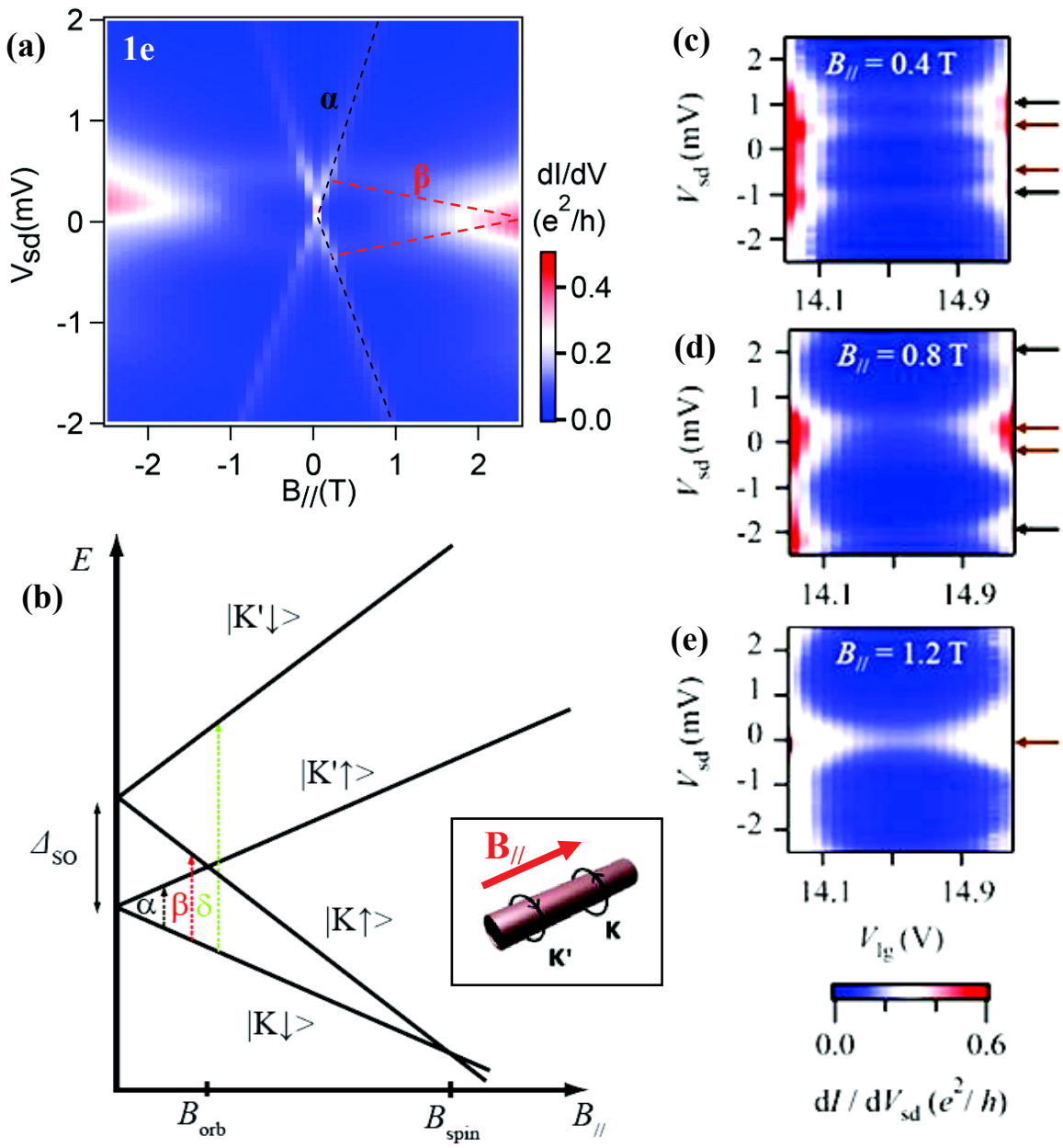

Figure 6.4. (a) dI/dV_{SD} along the center of the N = 1e diamond (red dotted line in Fig. 6.3) as a function of V_{SD} and $B_{//}$. (b) Diagram of the expected 1e energy levels as a function of $B_{//}$ for a nanotube with a negative spin-orbit coupling, $\Delta_{SO} < 0$. The possible transitions between ground and excited states are labeled as α, β and δ. Here, K' (CW) and K (CCW) state moves up and down in energy with applied $B_{//}$, respectively (inset). The sign of spin ↑ or ↓ bases on its relative direction (parallel or antiparallel) with $B_{//}$. (c-e) Differential conductance maps as a function of V_{LG} and V_{SD} for three magnetic field values of $B_{//}$ = 0.4 T, 0.8 T and 1.2 T.

N=3e

The evolution of the Kondo ridge at N=3e is shown in Fig. 6.5. The high slope line F and small slope line G (Fig. 6.5a) are due to the inter- and intra-orbital excitations, respectively. In contrast to the case of N=1e, the two negative small slope lines G do not cross at $B_{//} \approx 2.5$ T, which further confirms the negative of SO coupling as in our assignment of the energy levels (Fig. 6.5b). The other excitation (H) is not well observed here that is also probably due to the broadening of the energy levels.

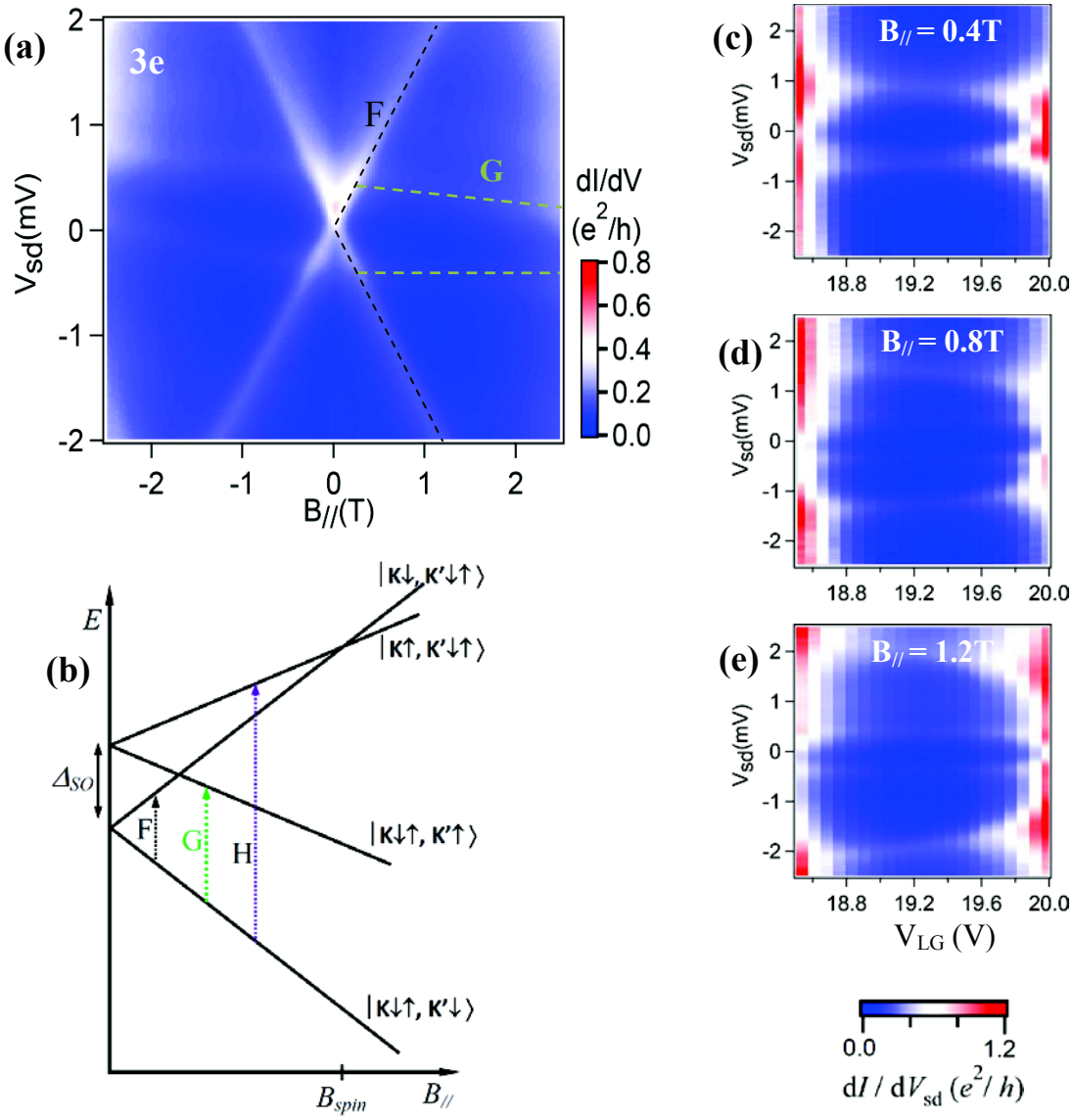

Figure 6.5. (a) dI/dV_{SD} along the center of the N = 3e diamond (blue dashed line in Fig. 6.3) as a function of V_{SD} and $B_{//}$. (b) Expected energy level scheme of the N = 3e ground state. F and G are the inter- and intra-orbital excitations respectively. (c–e) Maps of differential conductance as a function of V_{LG} and V_{SD} for three magnetic field values of $B_{//}$ = 0.4 T, 0.8 T and 1.2 T respectively, which does not show the Kondo effect at a finite magnetic field.

N=2e

First, we introduce the level spectrum of N=2e in the case without SOI and exchange energy J (Fig. 6.6). There are six possibilities of electron filling: two states of paired-electrons and other four of one singlet plus three triplet as mentioned in section 5.6. The six-fold degeneracy leads to the Kondo effect at haft-shell filling at zero magnetic field.

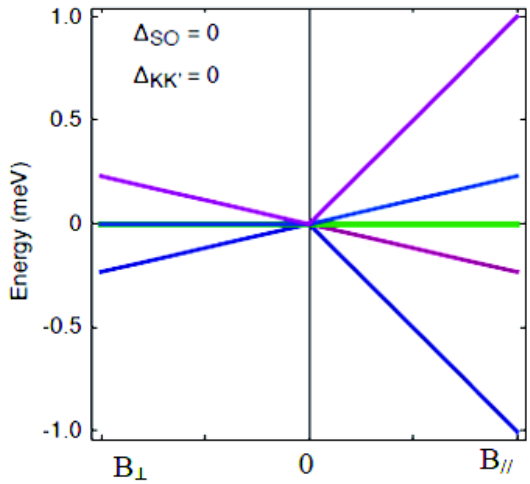

Figure 6.6. Level spectrum as a function of magnetic field for N=2e in a nanotube quantum dot with six-fold degeneracy ($\Delta_{SO} = 0 = \Delta_{KK'}$ and exchange energy J=0). Adapted from ref. [8].

In our case, the spectroscopy of the two-electron sector shows a clear evidence of the negative spin-orbit coupling (Fig. 6.7), which is strongly consistent with the schemes of N=1e and N=3e presented above. Since the map of conductance is quite complicated for N=2e, we use second derivative d^2I/d^2V_{SD} (Fig. 6.7a) instead of dI/dV_{SD} to make the transitions more visible. The peaks/dips appear at the inflection points of the conductance and they correspond to different transitions between ground and excited states.

Due to spin-orbit coupling, each of the two electrons is favored to possess parallel orbital and spin moments [1], which forces them into two different orbital states [9], [10]. The ground state is constituted by an inter-orbital singlet ($K\downarrow$ and $K'\uparrow$) as shown in Fig. 6.7b [11]. The two first inter-orbital excitations lead to the high slope lines of A, Δ without spin flip (keeping the singlet states). At $B = B_{orb}$ (≈ 0.9 T in our case), the A excited state (|K↓, K↑>) has the same energy with the ground state (|K↓, K'↑>), and the electron (the second one with spin up) can change its orbital freely. A Kondo ridge appearing at $B = B_{orb}$ is due to the pure

Kondo effect (orbital flip) [3]. When B > B_{orb}, these two singlet states diverge and the sign of the high slope line A changes from negative to positive (A') as shown in Fig. 6.7a.

In addition, the line B with small slope is assigned to the intra-orbital (spin flip) excitation from the ground state singlet to the triplet. Moreover, there is also a high slope line B', which is due to the inter-orbital excitation with spin flip (or secondary excitation) changing the state from singlet to triplet. This "combined" transition is allowed only at $B_{//}$ higher than a certain value (B ≥ 0.35 T in our case).

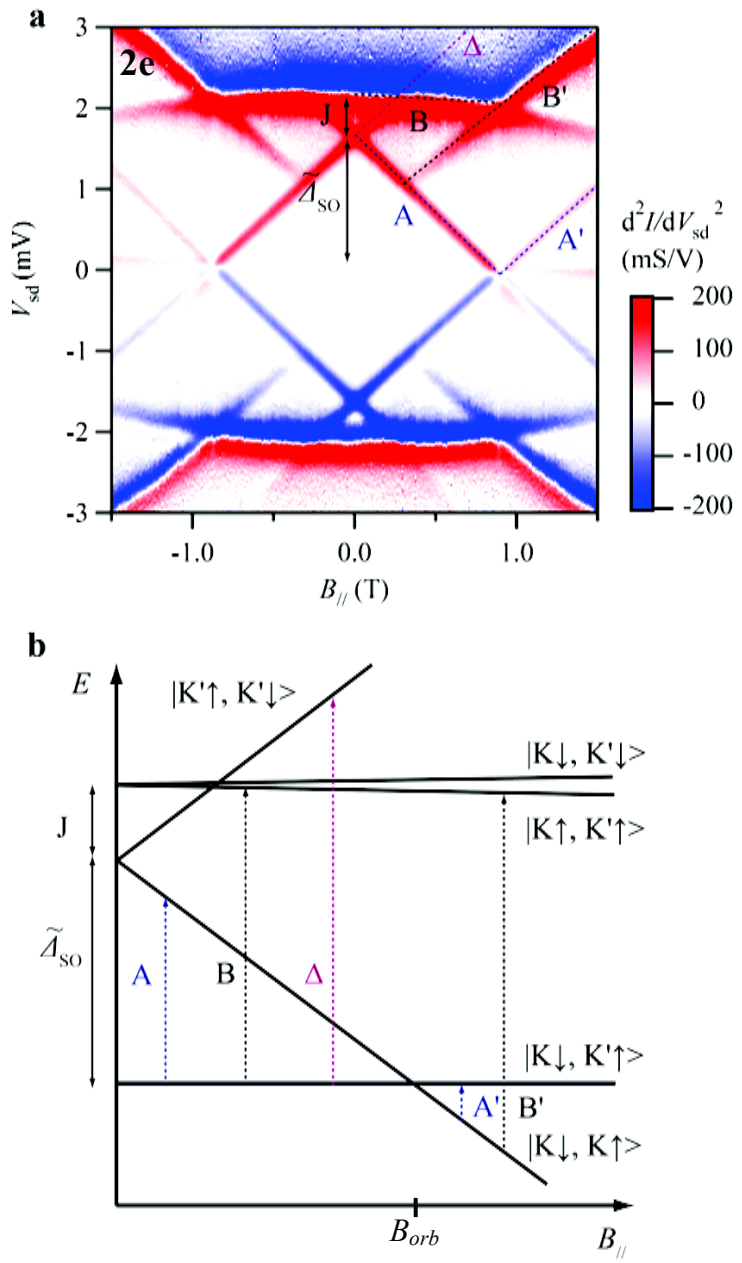

Figure 6.7. (a) Second derivative d^2I/d^2V_{SD} along the center of the N = 2e diamond (orange dotted line in Fig. 6.3) as a function of Vsd and $B_{//}$. (b) Expected energy level scheme of the N = 2e ground state. The excited states at energy 2Δ are not shown here.

The filling of electrons into the first shell is further confirmed by plotting a map of conductance as a function of V_{LG} and $B_{//}$ (at V_{SD}=0) as shown in Fig. 6.8. Near the zero magnetic field, the sign of $dV_{LG}/dB_{//}$ changes every time an electron is added, indicating that anticlockwise and clockwise orbitals are filled alternately. This behavior is a clear evidence of spin-orbit coupling [1]. Moreover, we also compared our measurement with the case of Δ_{SO} = 0 (Fig. 6.8c) and $\Delta_{SO} > 0$ (Fig. 6.8d) predicted in ref. [4]. The Kondo ridges appearing at B_{spin} and B_{orb} in the N=1e and N=2e case (Fig. 6.8a) are in a perfect agreement with the level spectrum of negative spin-orbit coupling (Fig. 6.8b).

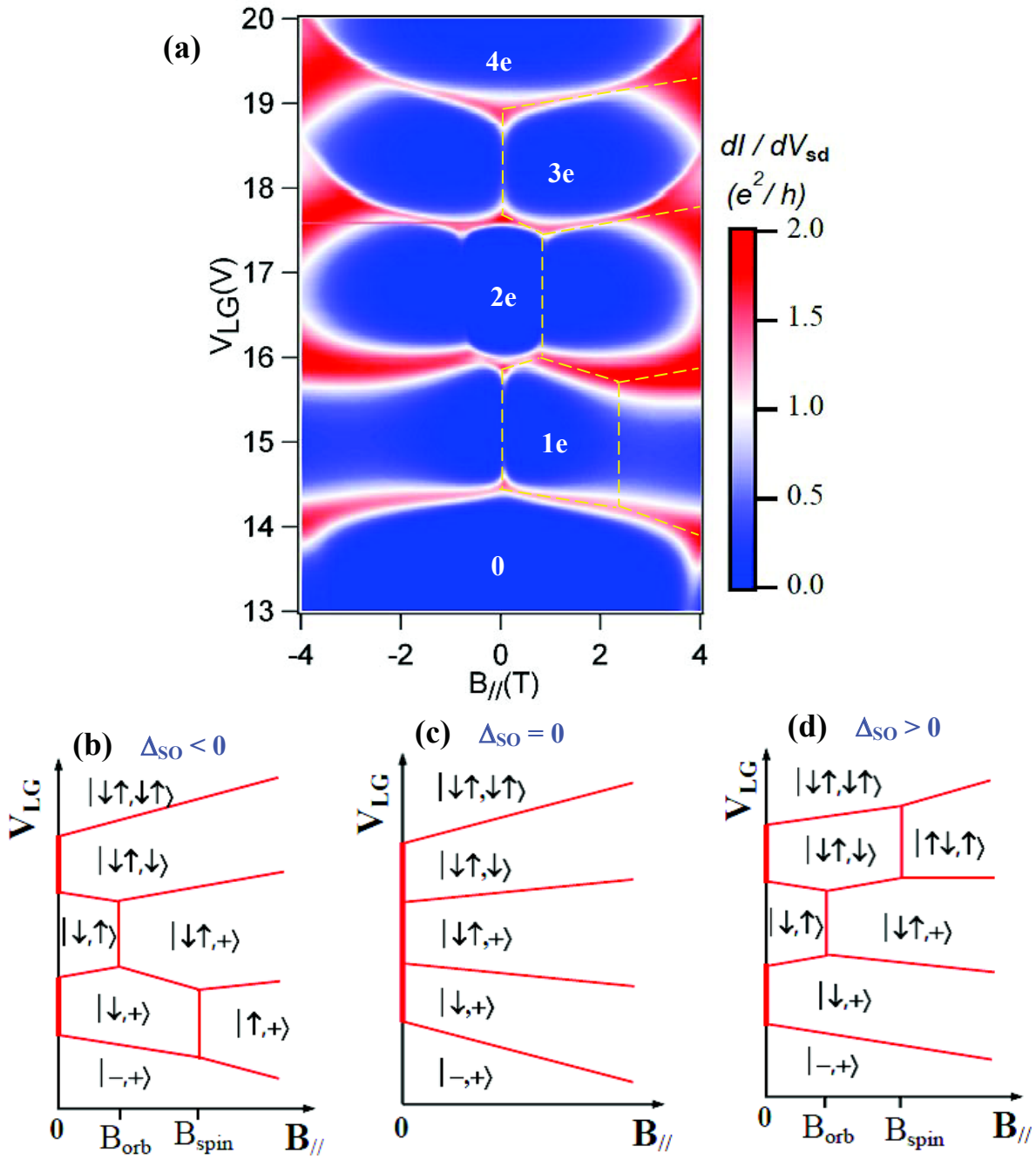

Figure 6.8. Filling of electrons into the first shell. (a) Map of conductance as a function of $B_{//}$ and V_{LG} (V_{sd}=0). Near zero field, the sign of slopes changes every time an electron is added in to the dot, which means CCW (K) and CW (K') orbitals are filled alternately. (b) Schematic phase diagram with $\Delta_{SO} < 0$ showing the boundaries between ground states of different charges of map. Predicted diagram [4] of Δ_{SO} =0 (c), and $\Delta_{SO} > 0$ (d). The orbitals K and K' are represented by the sign (–) and (+), respectively due to their down-shift and up-shift in energies with apply magnetic field.

Moreover, we also studied the interplay between SO coupling and SU(4) Kondo effect in the second shell of electrons. Since the SU(4) Kondo temperature significantly increases at higher gate voltages (higher tunneling rate, Γ), the spin-orbit coupling is less obvious ($k_BT_K >> \Delta_{SO}$). Details of the studies on the second shell electrons can be found in Annex 2.

6.3. Conclusion

In this work, we studied the spin-orbit coupling of electron in Kondo regime in an ultraclean carbon nanotube quantum dot. By studying the charge states of the electrons in the first shell, an unusually strong negative SOI ($\Delta_{SO} < 0$) is inferred in connection to the existing theories. Due to this SO coupling, the sequence of electron filling is completely different from that of pure SU(4) Kondo. The Kondo ridge in N = 2e cannot be formed at zero magnetic field, but at $B=B_{orb}$ instead due to the pure orbital Kondo effect. Moreover, another Kondo ridge appears at high magnetic field $B=B_{spin}$ in N=1e due to the negative value of SOI. Our measurements and assignments are very well consistent for all the four electrons in the first shell.

However, there are still several issues that we cannot explain completely at the moment. The exchange coupling *J* of singlet and triplet states is quite prominent in our measurements (Fig. 6.7). There is a small asymmetry in the spectra at positive and negative magnetic fields (Fig. 6.4 and 6.5). There is also a gate dependence of the cotunneling processes in N = 2e regime (Fig. 6.3 and 6.8). We are trying to understand more in connection to the electrons inter-shell interaction, the difference between the coupling of CW and CCW electrons with the metal leads, etc.

References

[1] F. Kuemmeth, S. Ilani, D. C. Ralph, and P. L. McEuen, "Coupling of spin and orbital motion of electrons in carbon nanotubes," *Nature*, vol. 452, no. 7186, pp. 448–452, Mar. 2008.

[2] T. S. Jespersen, K. Grove-Rasmussen, J. Paaske, K. Muraki, T. Fujisawa, J. Nygård, and K. Flensberg, "Gate-dependent spin-orbit coupling in multielectron carbon nanotubes," *Nature Physics*, vol. 7, no. 4, pp. 348–353, Jan. 2011.

[3] P. Jarillo-Herrero, J. Kong, H. S. J. van der Zant, C. Dekker, L. P. Kouwenhoven, and S. D. Franceschi, "Orbital Kondo effect in carbon nanotubes," *Nature*, vol. 434, no. 7032, pp. 484–488, Mar. 2005.

[4] M. R. Galpin, F. W. Jayatilaka, D. E. Logan, and F. B. Anders, "Interplay between Kondo physics and spin-orbit coupling in carbon nanotube quantum dots," *Phys. Rev. B*, vol. 81, no. 7, Feb. 2010.

[5] A. Makarovski, J. Liu, and G. Finkelstein, "Evolution of Transport Regimes in Carbon Nanotube Quantum Dots," *Phys. Rev. Lett.*, vol. 99, no. 6, p. 066801, 2007.

[6] A. Makarovski, A. Zhukov, J. Liu, and G. Finkelstein, "SU(2) and SU(4) Kondo effects in carbon nanotube quantum dots," *Phys. Rev. B*, vol. 75, no. 24, p. 241407, Jun. 2007.

[7] E. D. Minot, Y. Yaish, V. Sazonova, and P. L. McEuen, "Determination of electron orbital magnetic moments in carbon nanotubes," *Nature*, vol. 428, no. 6982, pp. 536–539, Apr. 2004.

[8] H. O. H. Churchill, "Quantum Dots in Gated Nanowires and Nanotubes," Harvard, 2012.

[9] J. Paaske, A. Rosch, P. Wolfle, N. Mason, C. M. Marcus, and J. Nygard, "Non-equilibrium singlet-triplet Kondo effect in carbon nanotubes," *Nature Physics*, vol. 2, no. 7, pp. 460–464, Jul. 2006.

[10] S. Florens, A. Freyn, N. Roch, W. Wernsdorfer, F. Balestro, P. Roura-Bas, and A. A. Aligia, "Universal transport signatures in two-electron molecular quantum dots: gate-tunable Hund's rule, underscreened Kondo effect and quantum phase transitions," *J Phys Condens Matter*, vol. 23, no. 24, p. 243202, Jun. 2011.

[11] D. E. Logan and M. R. Galpin, "Tunneling transport and spectroscopy in carbon nanotube quantum dots," *The Journal of Chemical Physics*, vol. 130, no. 22, pp. 224503–224503–15, Jun. 2009.

Chapter 7. Evaporation of $TbPc_2$ Single Molecule Magnets

7.1. Motivation

The ability to combine different components into hybrid devices is widely recognized as one of the key strategic technologies for the future. In the field of molecular spintronics, single molecule magnets – carbon nanotube (SMM-CNT) devices are revealing to be very interesting. For example, one of our recent studies of the spin valve effect on such devices has shown very high, up to several hundred percent, ratios of the magneto-resistance [1]. The $TbPc_2$ SMMs in these devices play the role of a localized spin polarizer and analyzer on electronic conducting channels of the CNT. The most important fabrication requirement of SMM-CNT devices is the grafting of a small but controlled number of single molecule magnets on the CNTs.

In this work, we developed a technique to fabricate hybrid devices of SMMs attached on suspended CNTs. In contrast to the technique used in ref. [1] where the SMMs are drop casted onto CNTs by solution method, here we used thermal evaporation to keep our CNT as clean as possible. In section 7.2, we shortly introduce the $TbPc_2$ SMMs and the grafting techniques. The details of the experimental setup and process parameters are described in section 7.3. In section 7.4, we show and discuss the main results. Due to the small size and small amount of the evaporated SMMs (expect one or few molecules in each cluster), we make the evaporation first on flat surfaces like sapphire and graphene for characterizations, and then on suspended CNTs. Here we show some primary results, and the work is still in progress.

7.2. Introduction to $TbPc_2$ single molecule magnets and grafting methods

7.2.1. $TbPc_2$ Single molecule magnets

Terbium bis-phthalocyaninato ($TbPc_2$ hereafter) is a mononuclear metal complex that behaves as a single molecule magnet which has the characteristics such as quantum tunneling of magnetization, large magnetic anisotropy, and slow relaxation of the magnetic moment [2–7]. Each $TbPc_2$ molecule includes a Tb^{3+} ion and two Pc (Pc = phthalocyanine) ligands on two sides as shown in Fig. 7.1. The two Pc ligands are rotated 45° to each other so that the Tb^{3+} ion is 8-fold coordinated with the N atoms.

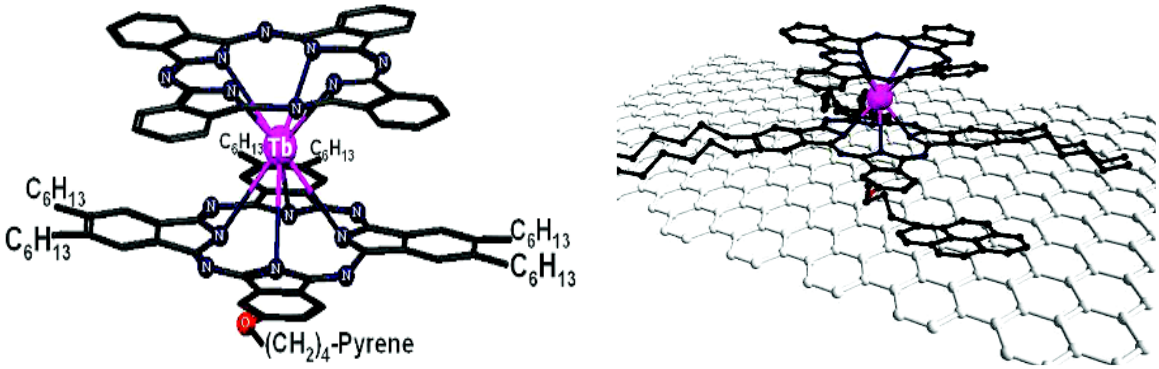

Figure 7.1. Structure of the pyrene-substituted $TbPc_2$ single molecule magnet. One Pc ligand is tailored with the addition of six Hexyl chains and one Pyrene group [8], [9].

Thanks to the rich and well-studied chemistry of phthalocyanines, it is possible to add tailored functionalities to these molecules while maintaining the SMM behaviors [10–12]. Pyrene groups and alkyl chains are known to exhibit an attractive interaction with sp^2 carbon materials, thus the pyrene-$TbPc_2$ molecules are bound with the graphene or CNTs via Van der Waals interactions [1], [8], [9], [13–15]. These non-covalent interactions avoid the possible insertion of local defects due to covalent bonding, which may alter the conducting properties of the graphene and CNT. Among the existing SMMs, single ion $TbPc_2$ is one of the most simple and robust molecule which is expected to retain its magnetic properties in different environmental conditions unlike many of the structurally more complex d-metal SMMs [8], [16]. The molecules used in this work are synthesized in microcrystalline powder form by the group of Ruben as described in [8].

7.2.2. SMMs deposition methods

The unique magnetic properties of SMMs have attracted significantly the interest of researchers over the last ten years. Despite the progress that have been made on the synthesis and characterization of SMMs [7], [17], the application of SMMs in molecular spintronics devices is still quite limited. One of the main reasons is the difficulty to deposit individual or well assembled SMMs on a desired surface. Moreover, the most important issue arising from these works is that, the properties of the SMMs and the host material must be still intact after the deposition [17].

There are two main methods to deposit SMMs on a surface: solution-based and vacuum-based techniques. In the former, the solution of SMMs is drop-casted on the surface or the substrate is immersed into the solution. After evaporation of the solvent, the molecules

are attached to the surface via interactions such as Van der Waals forces, hydrogen bonds, ionic or hydrophobic interactions [17]. This technique has been used successfully for the fabrication of several hybrid devices [1], [9].

In addition, the vacuum-based techniques have been more interesting since the SMMs and sample surface are very clean after the deposition. Thanks to this advantage, the ultra-high vacuum *in situ* characterization techniques such as STM and STS have revealed valuable information about the structures and electrical properties of the SMMs once they are grafted [18], [19]. The understanding of these properties is very important for the application of SMMs in spintronics devices. Between the two most common vacuum deposition techniques, electrospray and thermal evaporation, we chose the latter one for this work.

Thermal evaporation

Thermal evaporation is the cleanest deposition method compared with other techniques mentioned above, since it does not use any solvent. The SMMs are evaporated on the desired surface in a vacuum environment and at temperatures higher than the sublimation point. The recent studies have shown a successful evaporation of lanthanide-based bis-phthalocyaninato ($LnPc_2$) complexes owing to the robust and thermally stable properties of these SMMs [16], [19–21]. The evaporated $TbPc_2$ molecules were found to adsorb flat lying on Cu (100) [18], Cu (111) [19], Au (111) [20] and graphite [22] surfaces with the phthalocyanine planes parallel to the surface plane and their single molecule magnet properties were retained. Moreover, this technique also extends to the grafting and study of SMM on reactive surfaces, e.g. ferromagnetic metals, thanks to the high vacuum environment. The advantages of the thermal evaporation motivated us to use it for the grafting of SMMs on ultraclean CNTs.

7.3. Experimental details

7.3.1. Evaporation setup

We have built a system for evaporating the SMMs which is shown in Fig. 7.2. The setup consists of a Knudsen cell and sample holder with a shutter all inside a vacuum chamber created by a turbo pump. The heater (Thermocoax) is connected to a DC power supply with a regulator. A built-in K-type thermocouple is used to measure the temperature of the heater that is supposed to be the temperature of the copper box and the quartz crucible. Before and after the evaporation, the sample is hidden behind the shutter to avoid any

contamination may have. The temperate of the Knudsen cell can go up to 600 °C, and the vacuum can reach 10^{-7} mbar depending on the duration of pumping.

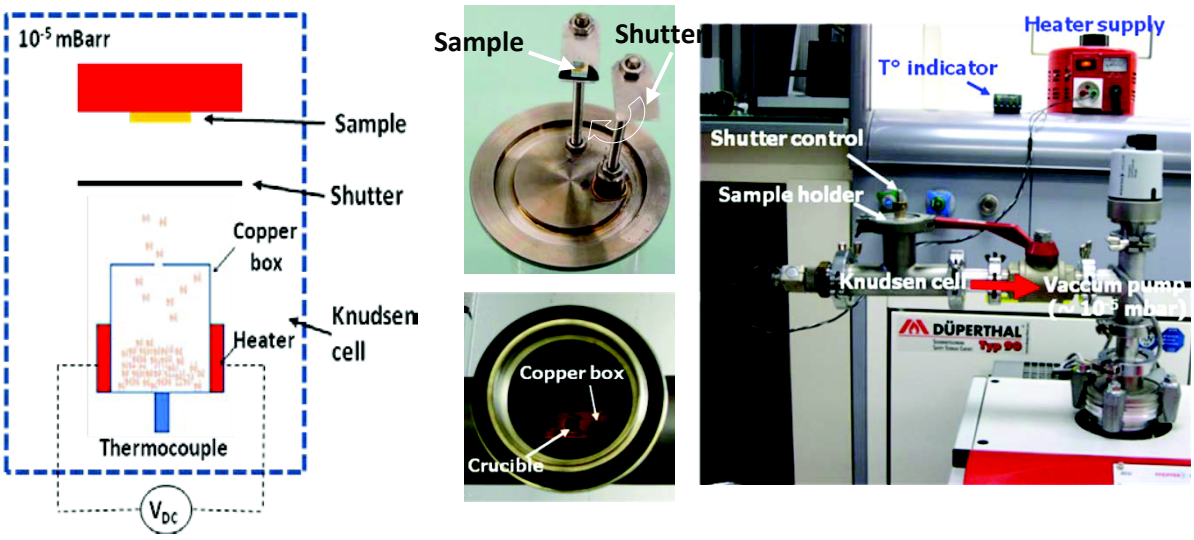

Figure 7.2. The thermal evaporator of single molecule magnets. (a) Schematic, and (b) experimental setup.

7.3.2. Evaporation parameters

The SMMs supplied by our collaborator are in a form of microcrystallized powder which contains many molecules. Here with the thermal evaporation, we would like to obtain molecular clusters with the size of one to few nanometers on our samples. Referring to the other works of fabricating SMM films [16], [21], we tried different parameters such as the quantity of SMMs powder used, temperature, heating rate and time of evaporation. To be able to characterize the small size evaporated SMMs, the substrate must be very flat (for morphology testing) or enhance the SMMs signal (for structure characterization). For this reason, a sapphire with high flatness and a graphene on SiO_2 were used in each evaporation. The grafting of SMMs on suspended CNTs was applied once we have found the optimal process conditions. The samples were characterized by AFM for morphology and cluster size, resonance raman spectroscopy for the integrity of the evaporated SMMs, and SEM for the case of SMMs on suspended CNTs.

This work was realized by “try and check” approach and it took us a lot of time. Here we present the procedure for evaporating the SMMs which was found after many trials. For each trial, we fixed the amount of SMMs powder to 0.5 mg. During the heating and cooling steps, the shutter was closed to protect the substrate. The crucible filled with the $TbPc_2$ compound was ramped up in temperature at an average rate of 10 °C/min to ensure

homogeneous heating of the powder. At desired temperature, we waited 5 minutes for the temperature to stabilize, which assures of having a constant flux of the sublimated molecules when the shutter is opened for evaporation. The samples are unloaded after the system has cooled down to room temperature.

7.4. Results and discussions

7.4.1. Evaporating temperature

The first parameter to be determined is the temperature at which the $TbPc_2$ SMMs start to sublimate. The AFM images of sapphire substrates after the evaporations at different temperatures for 10 minutes are shown in Fig. 7.3. It can be seen that the SMMs start to evaporate at 450 °C (Fig. 7.3b), that is in good agreement with the work in refs. [16], [21]. At higher temperature the SMMs evaporate at higher rate and form bigger clusters on the substrate (Fig. 7.3c, d).

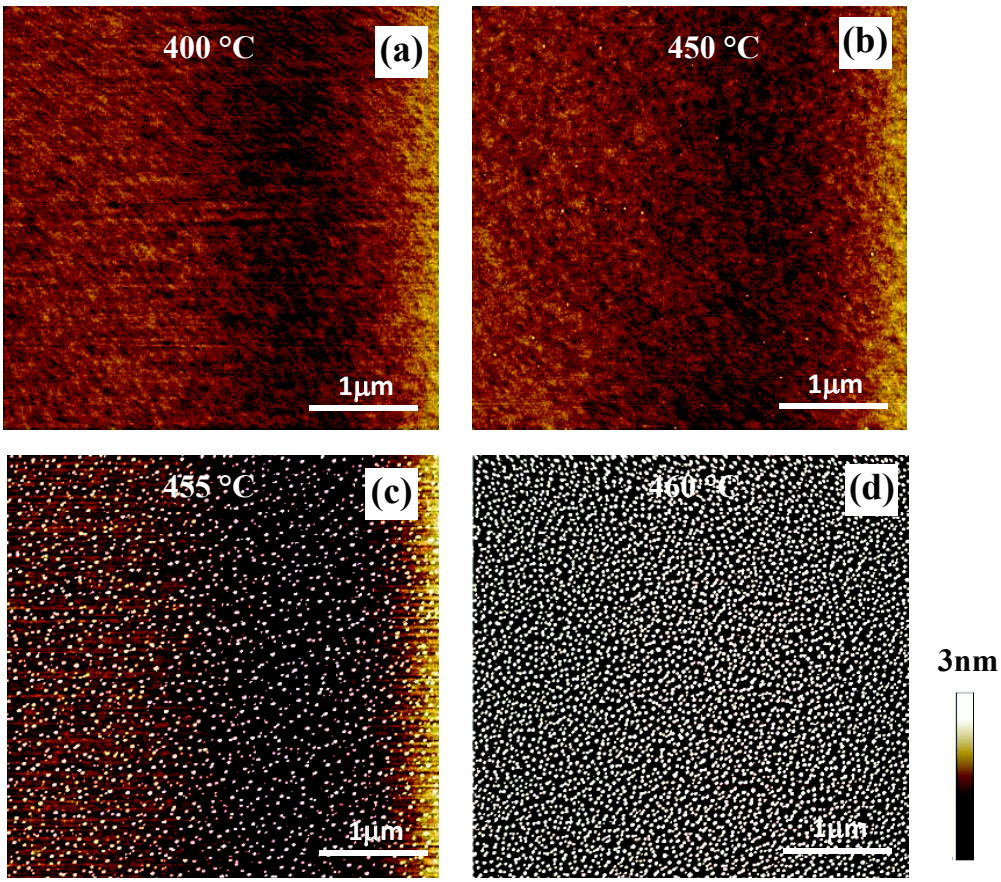

Figure 7.3. AFM images of samples after evaporation at (a) 400, (b) 450, (c) 455, and (d) 460 °C for 10 minutes on sapphire surfaces.

The AFM characterization, however, just shows the surface topography of the sample but not the intrinsic signature of the SMMs. For this reason, a resonance raman spectroscopy is essential. It has been shown to be a non-destructive and sensitive tool to probe the intramolecular vibration modes of the $TbPc_2$ molecules [13].

7.4.2. The integrity of the SMMs after thermal evaporation

One of the most important questions after the thermal evaporation is that whether the SMMs are still intact after such a high temperature treatment. Among the existing SMMs, $TbPc_2$ is one of the most robust molecule which is expected to retain its structure and magnetic properties in a wide range of different conditions [8], [16], [18–21]. The simplest characterization is to compare the pristine powder and the powder remaining in the quartz crucible after the evaporations. We used Raman spectroscopy with a laser wavelength of 633 nm, which has been shown to give the best resonance with $TbPc_2$. A low power of 0.5 mW for a 500nm laser spot is used in this characterization to avoid destruction of the molecules. Figure 7.4 shows the Raman spectra of the SMM powders. The most prominent peak of the molecule is the doublet at 1512 and 1520 cm^{-1} (so-called M-mode), which are attributed to the pyrrole C=C and aza C=N stretching modes, respectively (see insets on the right). These peaks were important for adjusting the right focus of the Raman laser in our experiments. Other vibration modes are noticed directly on the spectra [23], [24].

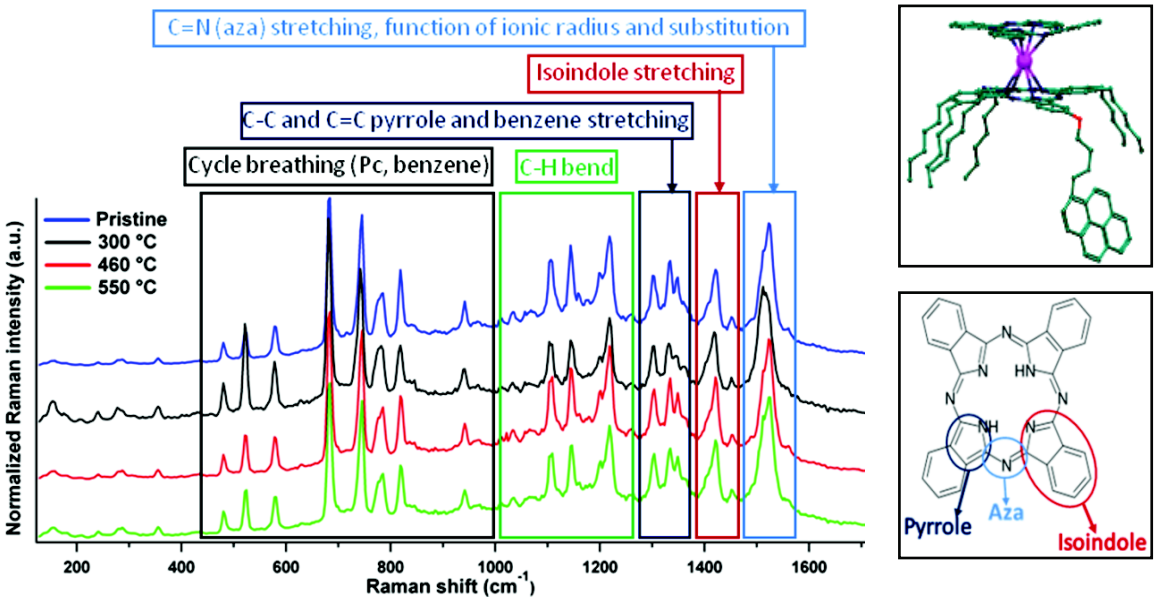

Figure 7.4. Raman spectra of $TbPc_2$ powders after heat treatment at different temperatures for 10 minutes.

Comparing the spectrum of pristine powders (blue curve) to the spectrum of thermally treated powders, it is clear that all the peaks corresponding to the vibration modes of the $TbPc_2$ molecule are unchanged after the thermal treatments. Our results are in good agreement with the works of Margheriti [16], [21] and Katoh [20], where they used more sophisticated techniques like Time-of-flight secondary ion mass spectrometry (ToF-SIMS), X-ray absorption spectroscopy (XAS), X-ray natural linear dichroism (XNLD), X-ray Magnetic Circular Dichroism (XMCD), Scanning tunneling microscopy (STM), and Scanning tunneling spectroscopy (STS) to confirm the integrity of the chemical composition, the structure, the electronic and magnetic properties of thermally evaporated $TbPc_2$ SMMs.

Moreover, we also characterized small clusters of $TbPc_2$ evaporated on a sample surface. Due to the small quantity of the evaporated SMMs, the Raman signals on sapphire or SiO_2 samples are very weak. Fortunately, it has been proved that such signals are greatly enhanced when using graphene as a background [13]. This kind of enhancement is thus very useful in our experiments. In addition, the interaction of $TbPc_2$ with graphene is supposed to be similar with CNT. The AFM imaging was combined with Raman spectroscopy in this characterization.

Figure 7.5 shows the AFM images of an exfoliated graphene flake on a SiO_2 surface before and after SMMs evaporations and its Raman map. The thickness of the flake is about 1.5 nm which corresponds to few graphene layers. It is obvious that the evaporated $TbPc_2$ molecules favor to graft on the graphene rather than the SiO_2 (Fig. 7.5b, c) due to the substituted groups of the molecules. Pyrene group is well-known to exhibit an attractive π-π interaction with the sp^2 carbon materials, and the supramolecular assembly is obtained via π-stacking interactions between the pyrenyl groups and the graphene surface or the CNT wall [1], [8], [9], [13]. Calculations also showed that the binding energy of the pyrene molecule to graphene is 2-times larger than the one to SiO_2 (1.06 eV vs 0.52 eV) [13]. This characteristic is very important for the fabrication of CNT-SMM hybrid devices.

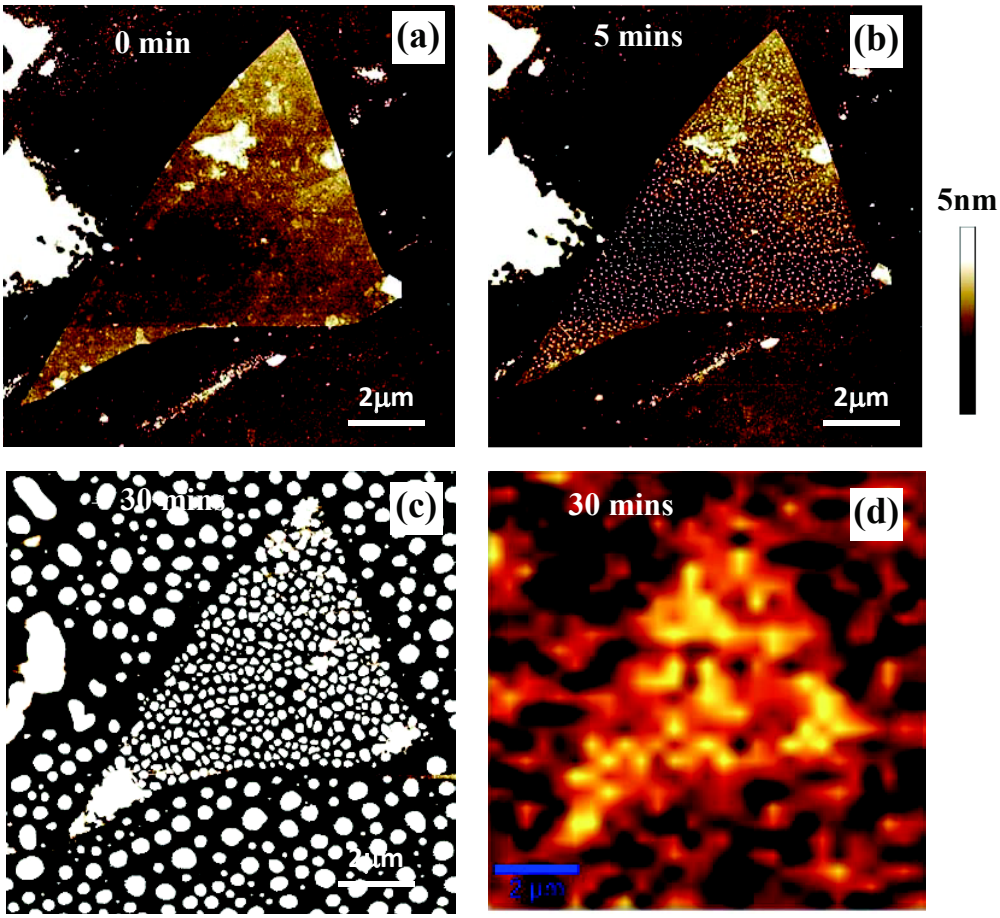

Figure 7.5. AFM images of a graphene sample. (a) Before, and (b, c) after evaporation in 5 and 30 minutes, respectively. (d) Raman intensity map of M doublet of $TbPc_2$ of the sample in (c).

The Raman spectra of these samples are shown in Fig. 7.6. The signals of the SMMs evaporated on graphene (Fig. 7.6c, d) are much stronger than on SiO_2 (Fig. 7.6e). In this characterization, the use of high quality graphene with low D-band ($\omega \sim 1330$ cm^{-1}) is necessary to reduce the overlap of graphene and SMMs peaks. By comparing these spectra with the powder one (Fig. 7.6a), we can see most of the peaks that are still in same positions. The evaporated SMMs on graphene are thus believed to keep their integrity.

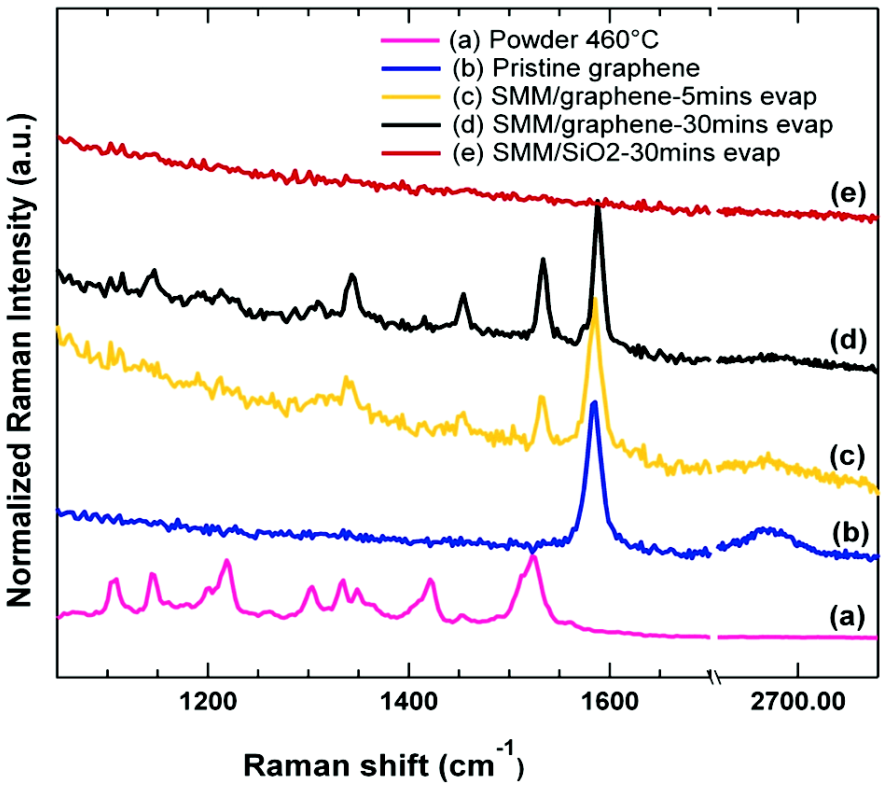

Figure 7.6. Raman spectra of the samples after evaporation at 460 °C. (a) Bulk powder remaining in crucible, (b) pristine graphene, (c) SMMs/graphene after 5 minutes evaporation, (d) SMMs/graphene after 30 minutes, and (e) SMMs/SiO_2 after 30 minutes evaporation.

7.4.3. Effect of evaporation time on thickness and size of molecule clusters

As shown in section 7.4.1, the $TbPc_2$ molecules started to evaporate at 455 – 460 °C. However in this narrow range of temperature, it is quite difficult to fine tune the cluster size and density. In contrast, here we fixed the temperature to 460 °C and changed the duration of the evaporation. The AFM images of the samples on sapphire surface are shown in Fig. 7.7, which also contains some scratches for testing the profile of the evaporated material.

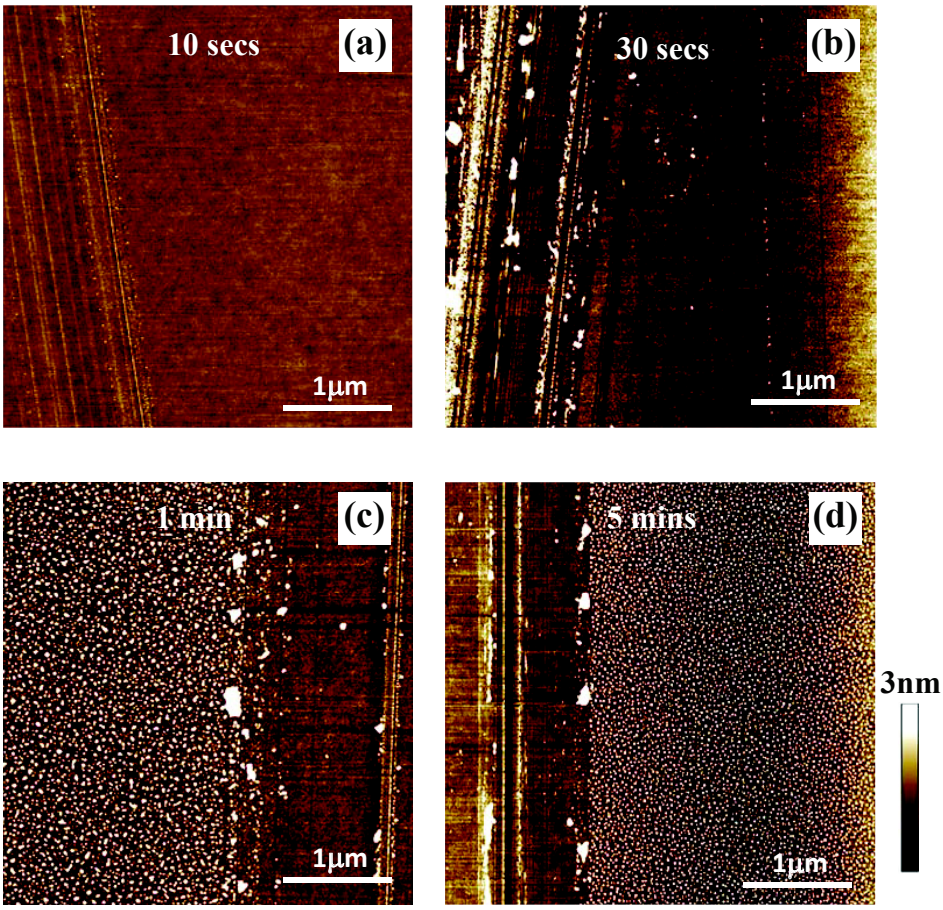

Figure 7.7. AFM images of samples after evaporation at 460 °C for (a) 10 secs, (b) 30 secs, (c) 1min, and (d) 5mins on sapphire surfaces.

In these samples, it is surprising that the evaporated SMMs prefer to form clusters instead of a continuous film. Increase in the time of evaporation leads to higher $TbPc_2$ molecule sublimation rate and bigger clusters (Fig. 7.8). For example, after 1 minute of evaporation (Fig. 7.8c) the clusters have sizes in range of 1-2 nm that is more or less the size of an individual or a cluster of few SMMs. These is about 10 clusters on a 1 μm long scan. When we increased the duration to 5 minutes, the clusters became larger reaching the sizes in a range of 1-5 nm with about the same density as before (Fig. 7.8d). This can be explained that in our experiment conditions (temperature, vacuum, source-sample distance, etc.), the evaporated SMMs have a finite energy when reaching the sample. Therefore, they can move a distance on the surface, transfer energy to the surface or to previously deposited molecules before immobilizing. The molecules prefer to build up at previously deposited SMMs positions and form bigger clusters.

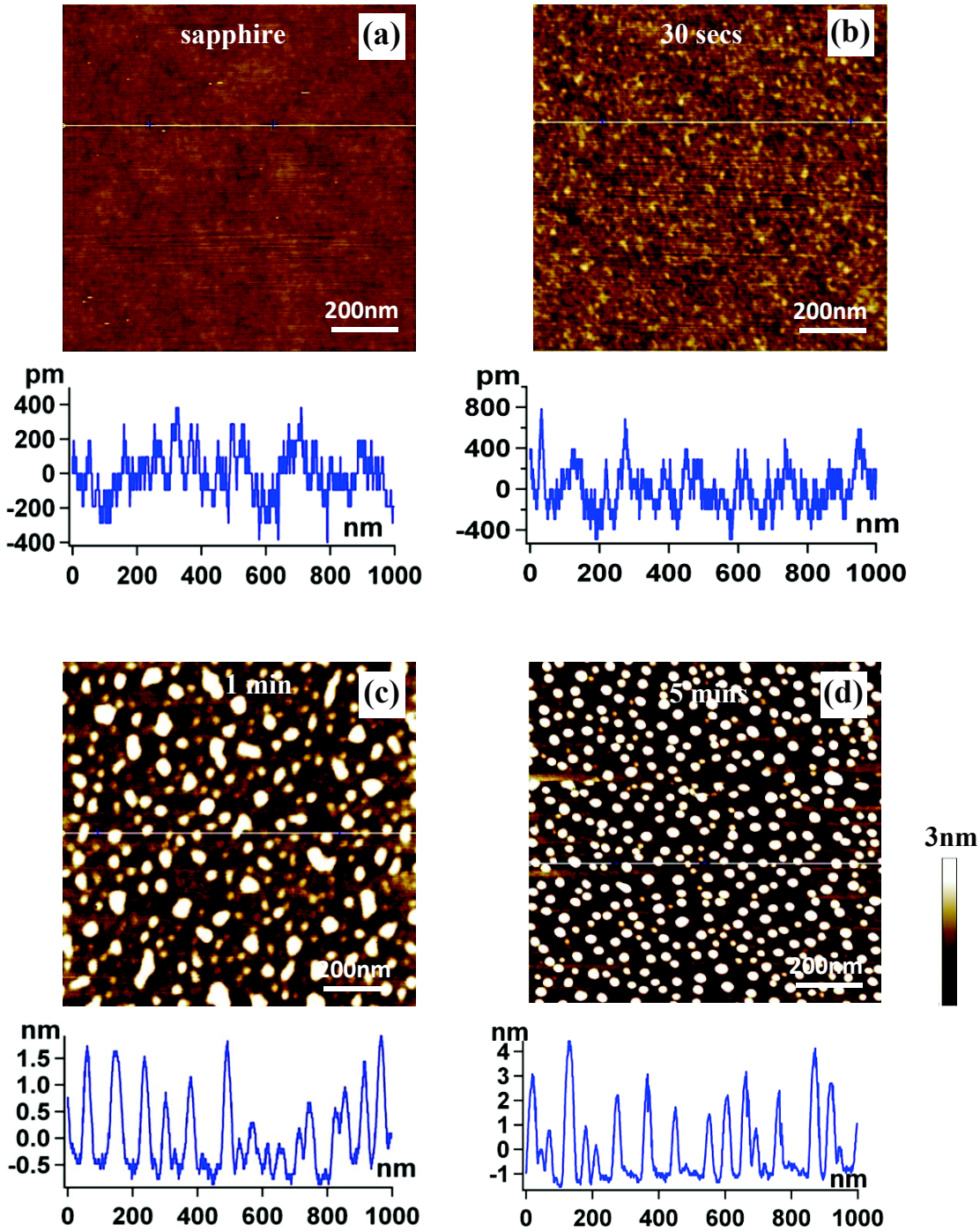

Figure 7.8. AFM images and profiles of sapphire samples after evaporation at 460 °C with different durations. (a) bare sapphire, (b) 30 secs, (c) 1 min, and (d) 5mins.

7.4.4. Evaporation of $TbPc_2$ onto suspended CNTs

After we had the information of clusters size and density of evaporated $TbPc_2$ on sapphire surface, we started the evaporation on sp^2 carbon materials including graphene and CNTs. The AFM image of $TbPc_2$ on graphene (Fig. 7.9a) shows the density of the clusters

and their sizes similar to that of on sapphire. In the case of suspended nanotubes, SEM imaging is used instead of AFM (Fig. 7.9b, c). The density seems to be a little bit lower than on surface. However, since the sizes of both CNTs and SMMs are too small, it is quite difficult to have an accurate estimation. Other techniques like TEM characterization and measuring the electronic and magnetic behavior of CNT-SMM hybrid devices is necessary. This work is still in progress and needs more elaborate studies.

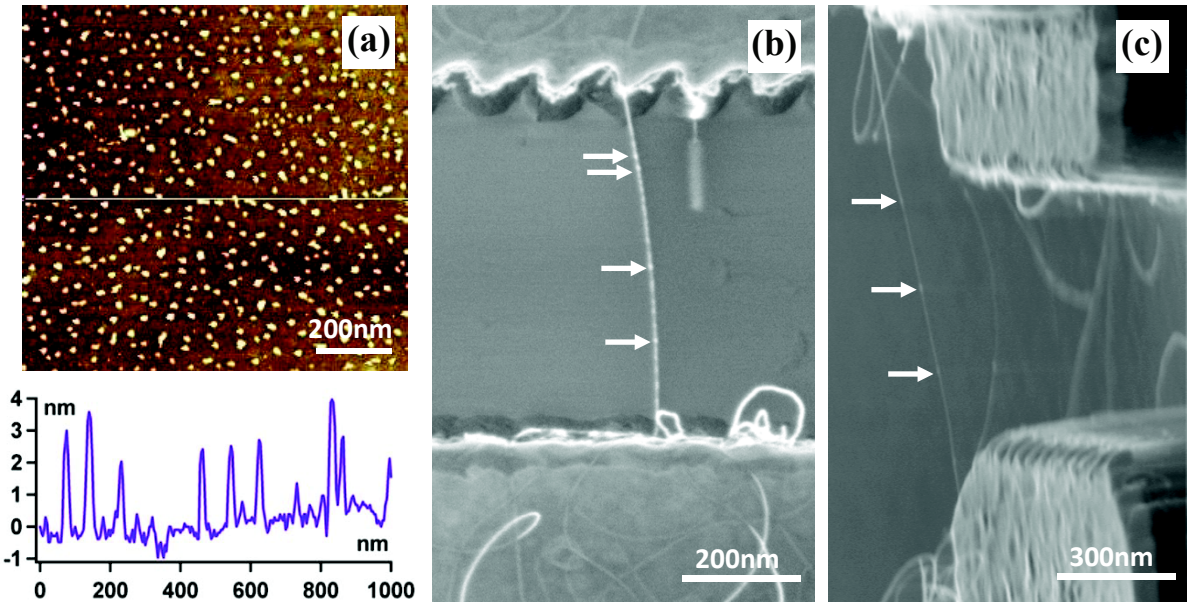

Fig. 7.9. Evaporation of SMMs on sp^2 carbon materials at 460 °C for 5 minutes. (a) AFM image and height profile of $TbPc_2$ on graphene. (b, c) SEM images of SMMs on suspended CNTs.

7.5. Conclusion

In this chapter, we described the evaporation of pyrene-substituted $TbPc_2$ SMMs. The molecules kept their integrity during the thermal evaporation. In the experimental conditions, small clusters are formed on the surface instead of a continuous film with an estimated concentration of 10 clusters per 1 μm length. By tuning the evaporation time and temperature, we could get clusters of the sizes of 1-2 nm. Moreover, the clusters are more likely to graft on sp^2 carbon materials than other surfaces. This work is promising for the fabrication of SMM-CNT hybrid devices.

References

[1] M. Urdampilleta, N.-V. Nguyen, J.-P. Cleuziou, S. Klyatskaya, M. Ruben, and W. Wernsdorfer, "Molecular quantum spintronics: supramolecular spin valves based on single-molecule magnets and carbon nanotubes," *Int J Mol Sci*, vol. 12, no. 10, pp. 6656–6667, 2011.

[2] N. Ishikawa, M. Sugita, T. Ishikawa, S. Koshihara, and Y. Kaizu, "Lanthanide Double-Decker Complexes Functioning as Magnets at the Single-Molecular Level," *J. Am. Chem. Soc.*, vol. 125, no. 29, pp. 8694–8695, Jul. 2003.

[3] N. Ishikawa, M. Sugita, and W. Wernsdorfer, "Quantum tunneling of magnetization in lanthanide single-molecule magnets: bis(phthalocyaninato)terbium and bis(phthalocyaninato)dysprosium anions," *Angew. Chem. Int. Ed. Engl.*, vol. 44, no. 19, pp. 2931–2935, May 2005.

[4] Wernsdorfer and Sessoli, "Quantum phase interference and parity effects in magnetic molecular clusters," *Science*, vol. 284, no. 5411, pp. 133–135, Apr. 1999.

[5] N. Ishikawa, M. Sugita, and W. Wernsdorfer, "Nuclear spin driven quantum tunneling of magnetization in a new lanthanide single-molecule magnet: bis(phthalocyaninato)holmium anion," *J. Am. Chem. Soc.*, vol. 127, no. 11, pp. 3650–3651, Mar. 2005.

[6] N. Ishikawa, M. Sugita, T. Ishikawa, S. Koshihara, and Y. Kaizu, "Mononuclear Lanthanide Complexes with a Long Magnetization Relaxation Time at High Temperatures: A New Category of Magnets at the Single-Molecular Level," *J. Phys. Chem. B*, vol. 108, no. 31, pp. 11265–11271, Aug. 2004.

[7] D. Gatteschi, R. Sessoli, and J. Villain, *Molecular Nanomagnets*. OUP Oxford, 2006.

[8] S. Kyatskaya, J. R. Galan Mascaros, L. Bogani, F. Hennrich, M. Kappes, W. Wernsdorfer, and M. Ruben, "Anchoring of Rare-Earth-Based Single-Molecule Magnets on Single-Walled Carbon Nanotubes," *Journal of the American Chemical Society*, vol. 131, no. 42, pp. 15143–15151, 2009.

[9] A. Candini, S. Klyatskaya, M. Ruben, W. Wernsdorfer, and M. Affronte, "Graphene Spintronic Devices with Molecular Nanomagnets," *Nano Lett.*, vol. 11, no. 7, pp. 2634–2639, Jul. 2011.

[10] J. Gomez-Segura, I. Diez-Perez, N. Ishikawa, M. Nakano, J. Veciana, and D. Ruiz-Molina, "2-D Self-assembly of the bis(phthalocyaninato)terbium(iii) single-molecule magnet studied by scanning tunnelling microscopy," *Chemical Communications*, no. 27, p. 2866, 2006.

[11] T. Ye, T. Takami, R. Wang, J. Jiang, and P. S. Weiss, "Tuning interactions between ligands in self-assembled double-decker phthalocyanine arrays," *J. Am. Chem. Soc.*, vol. 128, no. 34, pp. 10984–10985, Aug. 2006.

[12] W. Su, J. Jiang, K. Xiao, Y. Chen, Q. Zhao, G. Yu, and Y. Liu, "Thin-film transistors based on Langmuir-Blodgett films of heteroleptic bis(phthalocyaninato) rare earth complexes," *Langmuir*, vol. 21, no. 14, pp. 6527–6531, Jul. 2005.

[13] M. Lopes, A. Candini, M. Urdampilleta, A. Reserbat-Plantey, V. Bellini, S. Klyatskaya, L. Marty, M. Ruben, M. Affronte, W. Wernsdorfer, and N. Bendiab, "Surface-Enhanced Raman Signal for Terbium Single-Molecule Magnets Grafted on Graphene," *ACS Nano*, vol. 4, no. 12, pp. 7531–7537, Dec. 2010.

[14] D. A. Britz and A. N. Khlobystov, "Noncovalent interactions of molecules with single walled carbon nanotubes," *Chemical Society Reviews*, vol. 35, no. 7, p. 637, 2006.

[15] Y.-L. Zhao and J. F. Stoddart, "Noncovalent Functionalization of Single-Walled Carbon Nanotubes," *Acc. Chem. Res.*, vol. 42, no. 8, pp. 1161–1171, Aug. 2009.

[16] L. Margheriti, M. Mannini, L. Sorace, L. Gorini, D. Gatteschi, A. Caneschi, D. Chiappe, R. Moroni, F. B. de Mongeot, A. Cornia, F. M. Piras, A. Magnani, and R. Sessoli, "Thermal deposition of intact tetrairon(III) single-molecule magnets in high-vacuum conditions," *Small*, vol. 5, no. 12, pp. 1460–1466, Jun. 2009.

[17] N. Domingo, E. Bellido, and D. Ruiz-Molina, "Advances on structuring, integration and magnetic characterization of molecular nanomagnets on surfaces and devices," *Chem Soc Rev*, vol. 41, no. 1, pp. 258–302, Jan. 2012.

[18] L. Vitali, S. Fabris, A. M. Conte, S. Brink, M. Ruben, S. Baroni, and K. Kern, "Electronic Structure of Surface-supported Bis(phthalocyaninato) terbium(III) Single Molecular Magnets," *Nano Lett.*, vol. 8, no. 10, pp. 3364–3368, Oct. 2008.

[19] S. Stepanow, J. Honolka, P. Gambardella, L. Vitali, N. Abdurakhmanova, T.-C. Tseng, S. Rauschenbach, S. L. Tait, V. Sessi, S. Klyatskaya, M. Ruben, and K. Kern, "Spin and Orbital Magnetic Moment Anisotropies of Monodispersed Bis(Phthalocyaninato)Terbium on a Copper Surface," *J. Am. Chem. Soc.*, vol. 132, no. 34, pp. 11900–11901, Sep. 2010.

[20] K. Katoh, Y. Yoshida, M. Yamashita, H. Miyasaka, B. K. Breedlove, T. Kajiwara, S. Takaishi, N. Ishikawa, H. Isshiki, Y. F. Zhang, T. Komeda, M. Yamagishi, and J. Takeya, "Direct observation of lanthanide(III)-phthalocyanine molecules on Au(111) by using scanning tunneling microscopy and scanning tunneling spectroscopy and thin-film field-effect transistor properties of Tb(III)- and Dy(III)-phthalocyanine molecules," *J. Am. Chem. Soc.*, vol. 131, no. 29, pp. 9967–9976, Jul. 2009.

[21] L. Margheriti, D. Chiappe, M. Mannini, P.-E. Car, P. Sainctavit, M.-A. Arrio, F. B. de Mongeot, J. C. Cezar, F. M. Piras, A. Magnani, E. Otero, A. Caneschi, and R. Sessoli, "X-ray detected magnetic hysteresis of thermally evaporated terbium double-decker oriented films," *Adv. Mater. Weinheim*, vol. 22, no. 48, pp. 5488–5493, Dec. 2010.

[22] T. G. Gopakumar, F. Müller, and M. Hietschold, "Scanning tunneling microscopy and scanning tunneling spectroscopy studies of planar and nonplanar naphthalocyanine on graphite (0001).," *J Phys Chem B*, vol. 110, no. 12, pp. 6060–6065, Mar. 2006.

[23] F. Lu, Q. Yang, J. Cui, and X. Yan, "Infra-red and Raman spectroscopic study of tetra-substituted bis(phthalocyaninato) rare earth complexes peripherally substituted with tert-butyl derivatives," *Spectrochim Acta A Mol Biomol Spectrosc*, vol. 65, no. 1, pp. 221–228, Sep. 2006.

[24] J. Jiang, M. Bao, L. Rintoul, and D. P. Arnold, "Vibrational spectroscopy of phthalocyanine and naphthalocyanine in sandwich-type (na)phthalocyaninato and porphyrinato rare earth complexes," *Coordination Chemistry Reviews*, vol. 250, no. 3–4, pp. 424–448, Feb. 2006.

Chapter 8. Conclusions and perspectives

8.1. Summary of the results

In this thesis, we have succeeded in synthesizing high quality SWNTs, fabricating ultraclean CNT devices, and studying the electronic properties of CNTs with transport measurements. All these parts are important and in close relation with each other in an experimental sequence needed for revealing the interesting properties of CNTs.

First, we found the optimal parameters for obtaining high quality SWNTs by varying different parameters of the synthesis and characterizing carefully the dependence between the parameters and grown CNTs. The methane CVD process at 800 °C with the gas flows of 1200 sccm CH_4 + 700 sccm H_2 led to the best growth of SWNTs that are long (3-15 μm), straight, well crystallized, and have moderate number density. The samples grown in these optimized conditions were very clean from amorphous carbon. Moreover, the composition of the catalyst showed a very important role on the CNTs growth. Two different catalyst systems were studied, Fe-Mo and Fe-Ru, which both led to a high selective growth of SWNTs (> 94%) with narrow diameter distribution. The explanation of the role of bimetallic catalyst on the selective growth of SWNTs based on the phase diagrams and the experiment results was proposed. The optimal catalyst composition maintains the proper proportion of hydrocarbon decomposition and CNT nucleation during the synthesis and leads to a sustainable growth of long and well crystallized SWNTs.

For the fabrication of ultraclean CNT nanojunctions, we developed a procedure using a state of the art all electron beam lithography process. This enabled high accuracy fabrication of small and elaborate structures, e.g. the local gate devices. The CNTs were grown *in situ* at the last step, which lay freely suspended over the gap of the source-drain electrodes without any contact with the substrate surface, and thus were ultraclean from defects and disorders. The CNT junctions for the studies were selected according to their transport characteristics at room temperature instead of a SEM observation to keep the tubes as clean as possible.

The electrical transport measurements on these ultraclean CNTs showed a strong spin-orbit coupling of electron in the Kondo regime. When the SOI energy was comparable to that of the Kondo, it lifted the four-fold Kondo symmetry and quenched the zero bias Kondo resonance at half filling. The level spectra of the electrons in the first shell were investigated using inelastic cotunneling spectroscopy in an axial magnetic field, which showed a negative value of the SOI ≈ 0.34 meV. Due to this coupling, the sequence of electron filling was different from that of pure the SU(4) Kondo ($\Delta_{SO} = 0$) and a pure orbital Kondo effect was observed in the N=2e regime at finite magnetic field.

Moreover, we also developed a technique to thermally evaporate single molecule magnets (SMMs) for the future fabrication of ultraclean CNT-SMM hybrid devices. We optimized the process parameters first by evaporating SMMs on sapphire and graphene surfaces and characterizing them. Encouraging results were achieved in terms of the cluster sizes, number density, and integrity of the evaporated SMMs. The evaporation of SMMs onto ultraclean CNTs will need more elaborate studies in future.

8.2. Outlook

The success of fabricating ultraclean CNT devices is important for studying the electrical properties of CNTs. In the future, the measurements could be performed on more samples to gain a better understanding of the SOI in both the electron (observed in this work) and hole regimes. Since the SO splitting depends on the chirality of the CNT, it is necessary to combine the transport measurements with the structure characterization of the CNT, as well as to compare the experimental results with the current theory and calculations. This study will enrich the understanding about SOI effect as well as other properties of CNTs in combination with previous works.

Annex 1. Binary phase diagrams of C-Mo and C-Ru

(Supporting information for chapter 3)

A1.1. Phase diagram of C-Mo

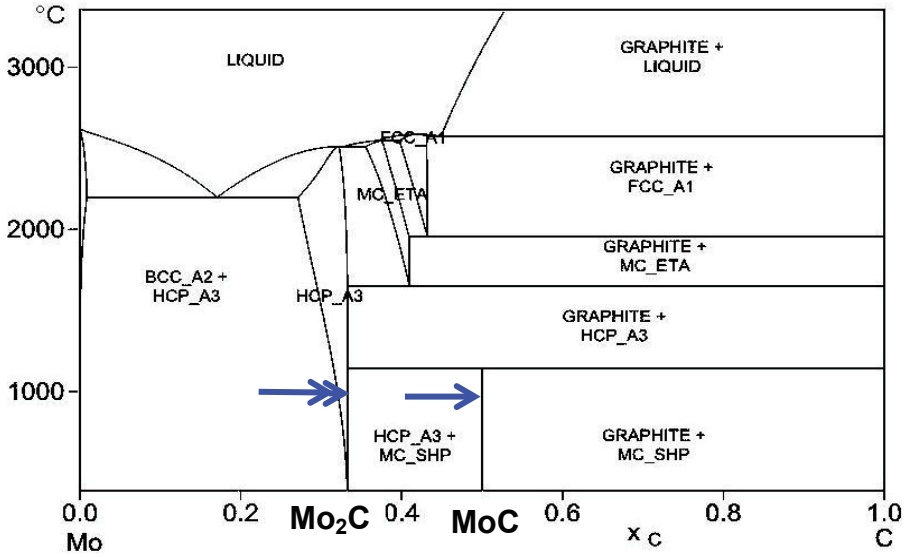

Figure A1.1. Mo-C phase diagram [1]. There are three carbide formations at ~ 32 at.%, 33.3 at.% (Mo_2C) and 50 at.% (MoC) at temperature 1000 °C, respectively. The multiple intermediate Mo carbides prevent saturation state of C for CNT growth [2].

A1.2. Phase diagram of C-Ru

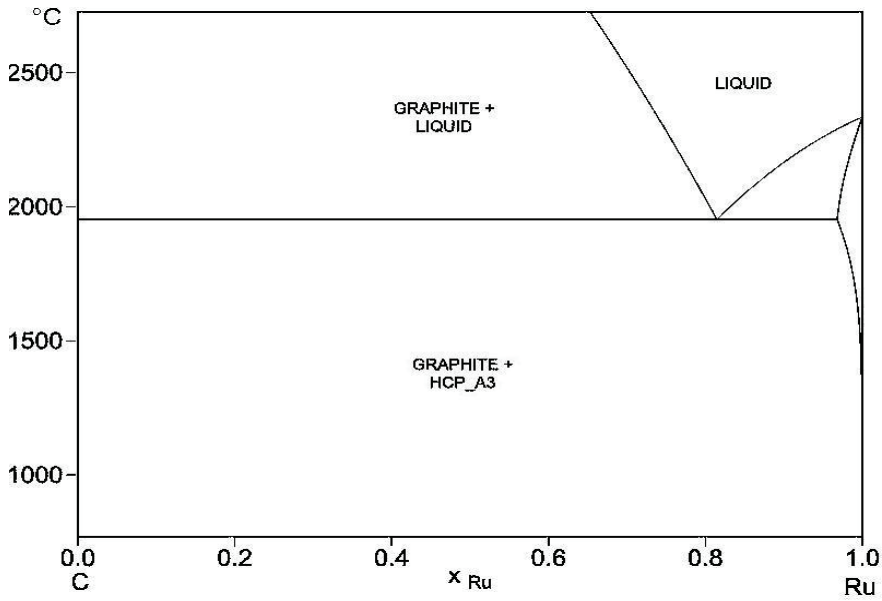

Figure A1.2. Ru-C phase diagram [3]. The carbon solubility of Ru is nearly zero at temperature ~ 1000 °C. No Ru carbide formation has been observed.

References

[1] MTDATA, "Phase Diagram Software from the National Physical Laboratory (C-Mo)," 2010. [Online]. Available: http://resource.npl.co.uk/mtdata/phdiagrams/cmo.htm.

[2] C. P. Deck and K. Vecchio, "Prediction of carbon nanotube growth success by the analysis of carbon–catalyst binary phase diagrams," *Carbon*, vol. 44, no. 2, pp. 267–275, Feb. 2006.

[3] MTDATA, "Phase Diagram Software from the National Physical Laboratory (C-Ru)," 2005. [Online]. Available: http://resource.npl.co.uk/mtdata/phdiagrams/cru.htm.

Annex 2. Spin-orbit coupling in Kondo regime of ultraclean CNT

(Supporting information of chapter 6)

A2.1. Kondo ridges in different shells

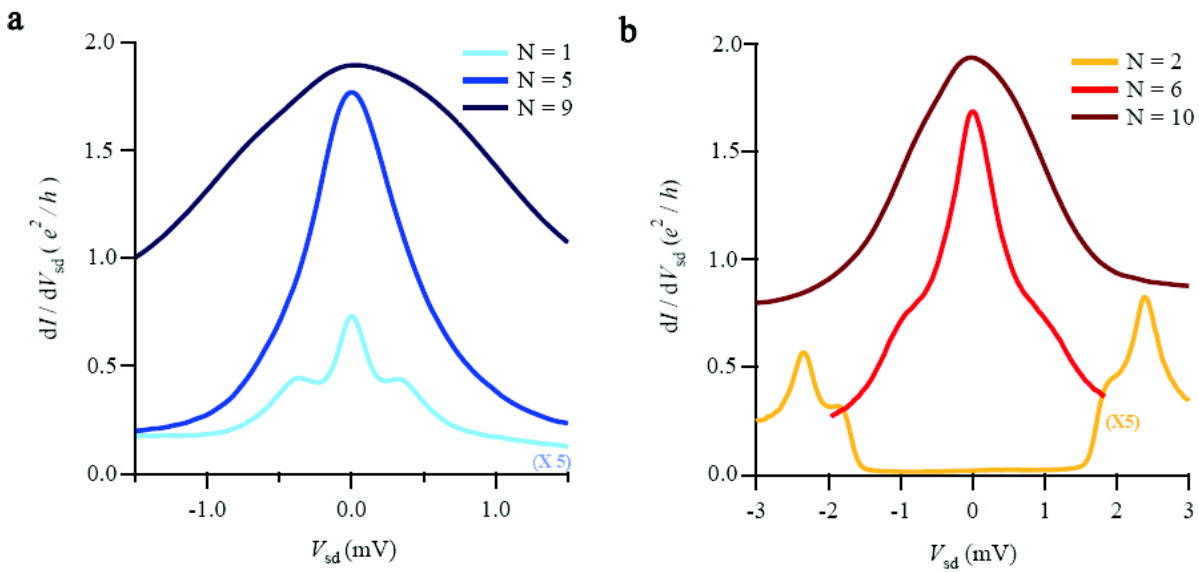

Figure A2.1. Slices of cotunneling patterns in the center of different Coulomb diamonds. (a) N=1,5,9. (b) N=2,6,10. For N=1e, the SO coupling splits the Kondo ridge with the excited states at ≈ 0.34 meV.

A2.2. Determination the angle of $B_{//}$ with the tube axis

In the study of spin-orbit coupling in carbon nanotubes, apply of magnetic field is essential. While the parallel magnetic field $B_{//}$ with the CNT axis leads to a strongest splitting of Kondo ridges and co-tunneling patterns, the perpendicular one gives very small field effect. Figure A2.2 shows the angle dependence of 1e and 2e splitting at B = 0.4 T. We determine $\theta_{//} \approx 20°$ and $\theta_{\perp} \approx 110°$.

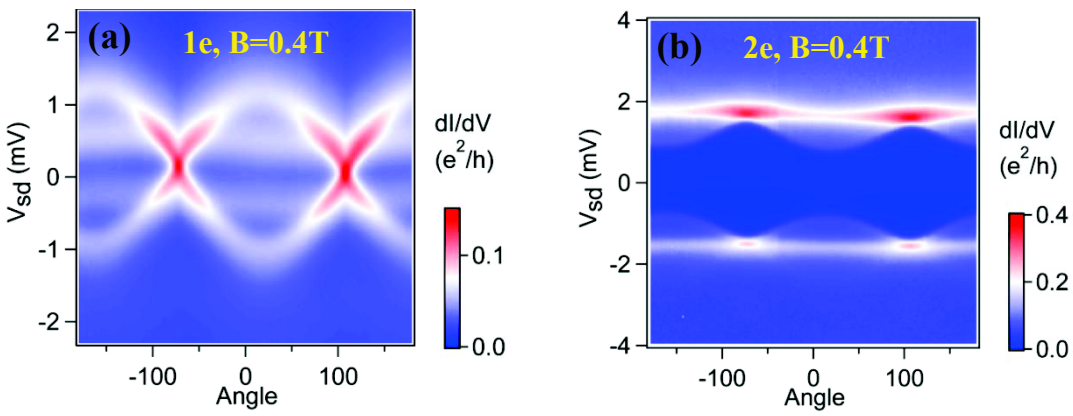

Figure A2.2. Evolution of the differential conductance as a function of B applied angle and V_{SD}. The B applied is fixed at 0.4T and V_{LG} is fixed in middle of (a) 1st and (b) 2nd diamond, respectively.

A2.3. Splitting of Kondo ridges in the second shell

The SO coupling is observed in the first shell of electron when the spin-orbit coupling energy $\Delta_{SO} \approx k_B T_K$. In the second shell, the CNT-electrode contacts are more transparent at higher V_{LG} leading to an increase of electron tunneling rate Γ and hence the $T_K^{SU(4)}$. The spin-orbit effect is less obvious in the second shell.

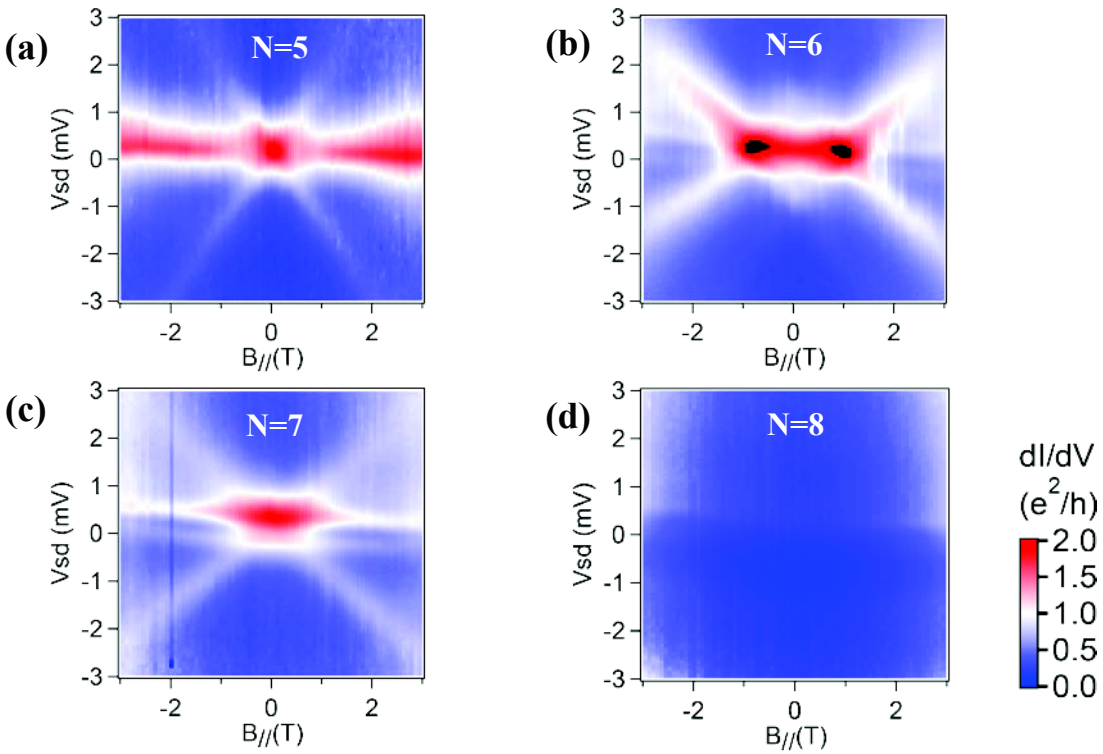

Figure A2.3. Splitting of Kondo ridges with $B_{//}$ of the second shell.